DEPARTAMENT DE FÍSICA ATÒMICA
MOLECULAR I NUCLEAR

INSTITUTO DE FÍSICA CORPUSCULAR

DOCTORAT EN FÍSICA

Time calibration and search for cosmic sources of high energy neutrinos with the ANTARES neutrino telescope

Ph. D. thesis dissertation by

Juan Pablo Gómez González

València, Setembre 2013

D. JUAN ZÚÑIGA ROMÁN, Professor Titular de la Universitat de València i D. JUAN de DIOS ZORNOZA GÓMEZ, Contractat Post-doctoral Associat a Projecte pel C.S.I.C.,

CERTIFIQUEN:

Que la present memòria, **Time calibration and search for cosmic sources of high energy neutrinos with the ANTARES neutrino telescope**, ha sigut realitzada baix la seua direcció en el Institut de Física Corpuscular (Centre Mixt Universitat de València - CSIC) per D. Juan Pablo Gómez González i constitueix la seua Tesi Doctoral en el Departament de Física Atòmica Molecular i Nuclear de la Universitat de València per a optar al grau de Doctor en Física.

I per a que conste, en compliment de la legislació vigent, signem el present Certificat a Paterna, a 16 de setembre de 2013.

Signat: Juan Zúñiga Román

Signat: Juan de Dios Zornoza Gómez

Agradecimientos

Me gustaría dar las gracias en primer lugar a Juan José Hernández Rey que, como responsable del grupo ANTARES en el IFIC, me dio la oportunidad de embarcarme en este proyecto, y también por su empuje para llevar el barco a buen puerto.
Quiero expresar mi agradecimiento más sincero a los directores de esta tesis, Juan Zúñiga y Juande Zornoza, por su confianza, dedicación e inestimable ayuda. Sin su experiencia y guía esta tesis nunca habría visto la luz.

Gracias también a Salvi, Umberto, Paco, Ciro, Harold, Agustín, Joaquín, Diego, Javier, Simona, Juanan, Guillaume y Damien, compañeros y amigos con los que he tenido la suerte de compartir algo más que un gran entorno de trabajo durante todos estos años.

Thanks to Paschal Coyle, Vincent Bertin and Heide Costantini at CPPM and to Maarten de Jong and Aart Heijboer at NIKHEF for giving me the chance to join their groups during my stays in Marseille and Amsterdam. I'm also thankful to many people in the ANTARES Collaboration for the useful discussions and suggestions, which have been fundamental for the realization of this thesis.

Por supuesto, quiero dar las gracias a Raquel, mi principal apoyo y compañía en este viaje. También a los amigos que he encontrado a lo largo del mismo, por todos los buenos ratos que hemos pasado y por los que nos quedan. Y a los que reencuentro cuando vuelvo a mi tierra, que siempre consiguen que me crea que nunca la he dejado. Por último, doy las gracias a mi hermana Dolores, por su importancia en esta historia y por traer a este mundo, hace tan solo unos meses, al pequeño Manuel.

Quero adicar esta tese á miña benquerida nai: a túa lembranza, os agarimos e apoios dados, as túas ensinanzas e consellos, o teu sorriso e ledicia sempre ficarán comigo.

Á memoria da miña nai

Contents

1

High energy neutrino astronomy

In the last decades neutrino astronomy has become a mature experimental technique which tries to open a new window to the universe by using neutrinos as cosmic messengers. The main motivation that guides the efforts to detect high energy neutrinos from astrophysical sources is the present lack of knowledge concerning the origin and powering mechanisms of cosmic rays (CRs). These are particles detected in a wide range of energies at Earth and considered to be produced at some known astrophysical objects. Such association, however, has not been confirmed yet because the interstellar and intergalactic magnetic fields randomize their arrival directions. In this chapter, the connection between cosmic rays and neutrinos (and gamma-rays) will be discussed, as well as the characteristics that make neutrinos exceptional probes to explore the deeper and most violent universe and the most suited messengers to identify the sources of the high energy cosmic rays.

1.1 Cosmic rays

Cosmic rays are energetic particles that continuously bombard the upper shells of the Earth's atmosphere from outer space. The discovery of the extraterrestrial origin of CRs was done in 1912 by Victor Hess [1]. Using golden electrometers detectors launched in balloons, Hess measured an increase on the flux of ionizing particles with altitude, refuting the widely accepted hypothesis that the ionization was caused by radioactive elements in the ground. Hess' discovery was confirmed later by R. A. Millikan, who coined the term cosmic rays.

In 1937 Pierre Auger could conclude, from ground-based measurements, that CRs were able to generate extensive air showers of particles in their interaction with the atmosphere nuclei [2]. Ground experiments also pointed out that the energy contained in these showers was orders of magnitude higher than the energy of the cosmic rays that had been measured in the balloon experiments. Figure 1.1 depicts the development of a cascade of secondary particles from the interaction of a cosmic ray with a nucleus of the Earth's atmosphere.

1.1.1 Composition and energy spectrum

Direct and indirect measurements done until present show that primary cosmic rays are constituted by charged particles including protons ($\sim 90\%$), helium ($\sim 9\%$) and heavier nuclei ($\sim 1\%$) and a tiny admixture of electrons (Figure 1.2). Multi-experiment data draw (Figure 1.3) an energy spectrum for CRs that follows a broken power law of the form

$$\frac{dN}{dE} \sim E^{-\gamma}, \tag{1.1}$$

where N is the number of particles observed, E is the energy of the primary particle and γ is the spectral index. The spectrum of CRs extends over 13 orders of magnitude in energy (from about 10^8 eV to roughly 10^{21} eV) and near 31 orders of magnitude in flux. It features two main breaks usually referred to as the "knee" and the "ankle".

For energies between 10^{10} eV and up to $\sim 5 \times 10^{15}$ eV (below the knee) the flux of CRs per unit of area, time, solid angle and energy is well described considering a spectral index $\gamma \sim 2.7$. Most relevant information on this region has been provided by satellites and balloon experiments. The most accepted model for the origin of these CRs is based on the diffusive shock acceleration of interstellar matter around Supernova Remnants (see Section 1.2). At higher energies, the spectrum steepens to a power law index of ∼3.1. Although being usually interpreted as the point where the galactic accelerators reach their maximal boost power, the origin of this knee is still an open question [3]. There are experimental indications supporting an increase of the average mass of the CRs when passing the knee [4] and that the index drop may start at different energies depending on the involved element. Several experiments have collected data that is consistent with a change in the spectrum slope which moves from an index of 3.0 to a value of about 3.3 at energies of $\sim 4 \times 10^{17}$ eV. Then, we find the ankle at energies of $\sim 10^{19}$ eV, where the flux is only one particle per kilometer square per

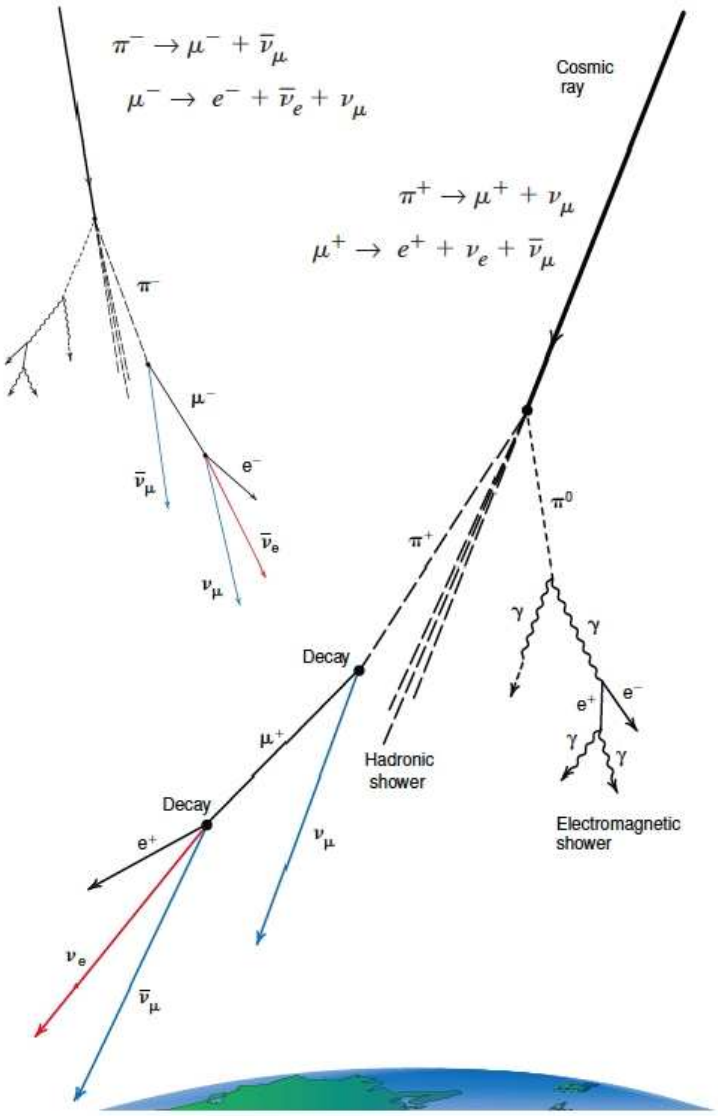

Figure 1.1: Development of an extensive air shower of secondary particles induced by the interaction of a primary cosmic ray with a nucleus in the atmosphere. The muons and the neutrinos are the only particles produced that reach the Sea level and penetrate significant depths underground.

year per stereo-radian and the energy spectrum becomes less steep ($\gamma \sim 2.8$). The origin of the ankle is usually explained considering the transition of CRs from galactic to extragalactic origin [5]. This region of the spectrum is only accessible to very large area ground detectors such as the Pierre Auger Observatory (PAO) in Argentina (see Section 1.2.3), which has reported [6] evidence of the spectrum suppression above a threshold of ∼50 EeV (Figure 1.4). This cutoff[1], predicted by Greisen, Zatsepin and Kuzmin in 1966 [8] [9], is caused by the energy losses derived from the interaction of such ultra high energy protons with the cosmic microwave background (CMB) photons (Equation 1.2), and is usually referred to as the GZK effect:

$$\begin{aligned} p + \gamma_{CMB} &\rightarrow \Delta^{+} \rightarrow \pi^{0} + p \\ p + \gamma_{CMB} &\rightarrow \Delta^{+} \rightarrow \pi^{+} + n. \end{aligned} \tag{1.2}$$

These ultra high energy cosmic rays (UHECRs) are the most energetic particles ever observed, several orders of magnitude above the possibilities of present particle accelerators like the LHC at CERN.

1.2 Origin and acceleration mechanism of cosmic rays

Any plausible scenario for the production of CRs should be able to power them at the high energies observed. In this sense, the so-called *top-down* scenarios consider that cosmic rays are the decay products of supermassive particles originated in the Big Bang, while *bottom-up* scenarios propose acceleration processes in astrophysical sources as the mechanism responsible for the energizing of cosmic rays. Top-down scenarios are unlikely on the light of the results that confirm the GZK suppression [13] and because the lack of photons at the highest energies. Along this work it will be assumed that CRs are correlated with some known cosmic sources like Supernova Remnants (SNR), Microquasars, Active Galactic Nuclei (AGNs) or Gamma Ray Bursts (GRBs) [2].

[1] First observed by HiRes [7]

[2] Description of these sources is given in Section 1.5

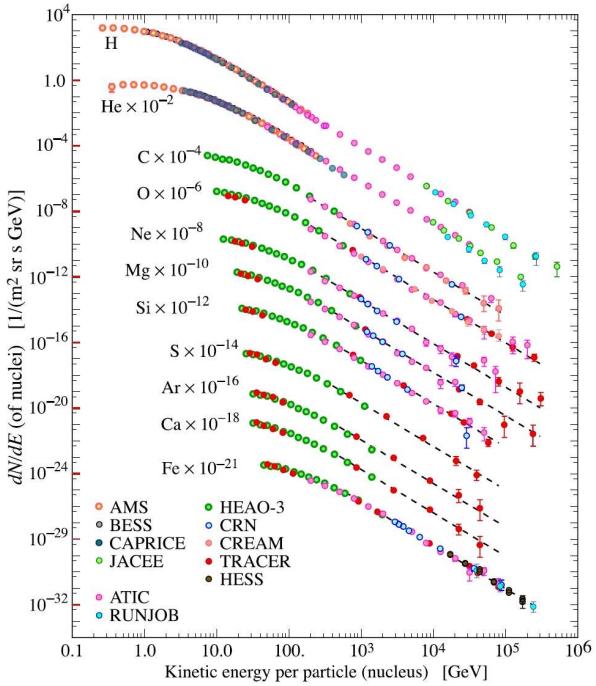

Figure 1.2: Multi-experiment measurements of the primary cosmic rays composition. See [10] for references.

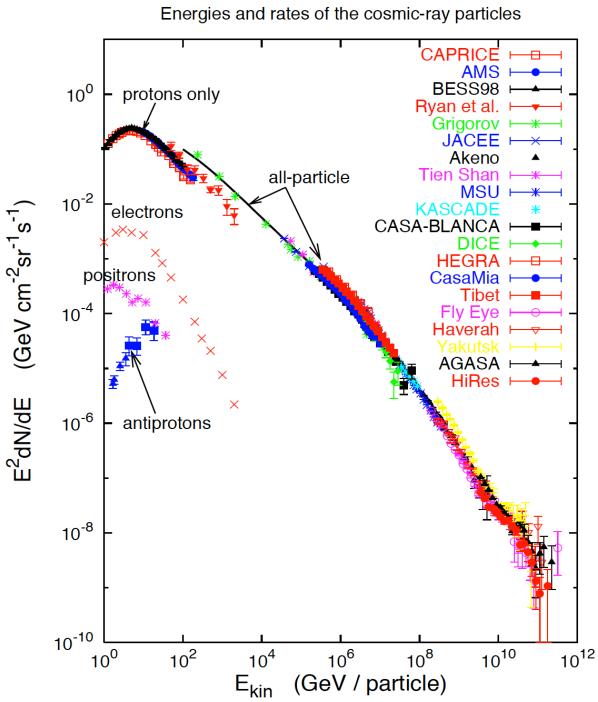

Figure 1.3: Multi-experiment measurements of the cosmic ray flux spectrum (multiplied by E^2) from 10^9 to 10^{21} eV. See [11] for references.

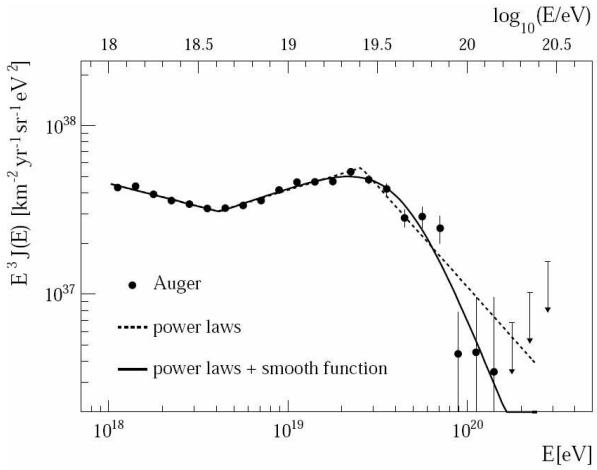

Figure 1.4: Combined energy spectrum of UHECRs measured by PAO [12].

1.2.1 Fermi acceleration mechanism

In 1949 Fermi proposed [14] a mechanism by which charged particles can be accelerated as they elastically scatter on the irregularities of the magnetic fields in a plasma cloud moving with a velocity V_c much smaller than the velocity of light (c) in vacuum (Figure 1.5 (a)). The result of the process is an average gain in energy (ΔE) which is proportional to the square of the cloud velocity expressed in units of c ($\beta = V_c/c$). Assuming a typical velocity of the gas cloud of $\sim$100 km/s, the energy gain is of the order of 10^{-7} and thus quite inefficient. This approximation is usually called the Fermi second order acceleration mechanism because of the quadratic proportionality with β. An extended and more efficient version was developed at the end of the 1970's decade [15]. The so-called first order Fermi acceleration mechanism describes the diffusive acceleration of particles in the presence of strong shock waves (Figure 1.5 (b)), which are known to be produced during the explosive mass ejection of a supernova. In this scenario, the average increase in energy is linear in the cloud velocity (Equation 1.3):

$$\frac{\Delta E}{E} \simeq \frac{4}{3}\beta \tag{1.3}$$

Considering that particles might be caught in the region of acceleration because of the presence of turbulent magnetic fields in the surrounding environment and forced to cross the front *n* times, the process leads to a particle final energy *E* (starting with initial energy E_0) given by

$$E_n = E_0 \left(1 + \frac{\Delta E}{E}\right)^n . \tag{1.4}$$

The first order Fermi mechanism produces a power-law energy spectrum with a spectral index $\alpha \sim 2$ which explains satisfactorily the cosmic ray flux trend observed up to energies of about 10^{15} eV (see [16]). The measured spectral index (Figure 1.3) is steeper than the predicted source spectrum because of the energy dependence of the cosmic ray diffusion out of the Galaxy (the particles with high energy are less confined by the galactic magnetic field). However, regarding the sources for the highest energy cosmic rays, there is not a general consensus but some plausible arguments which generally assume an extragalactic origin.

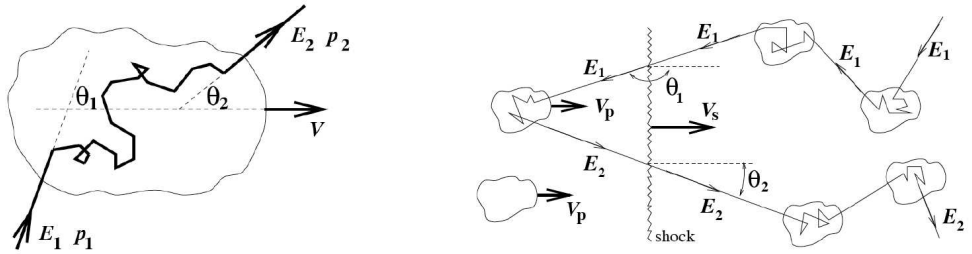

(a) Second Order (b) First Order

Figure 1.5: Sketches of the Fermi acceleration mechanisms.

1.2.2 The Hillas' diagram

Based on the simple argument that the Larmor orbit (or gyro-radius) of an accelerated charged particle has to be smaller than the size of its accelerator, Hillas' [17] derived a diagram (Figure 1.6) that constrains the possible sources for the acceleration of CRs according to the maximum energies that they can produce. The Hillas relation, which is independent of the acceleration mechanism, is given by

$$E_{max} = \Gamma V_c Z B R, \tag{1.5}$$

where Γ is the Lorentz boost factor, V_c the shock wave velocity in the Fermi scheme, Z is the charge of the particle, B is the magnetic field strength in the region where acceleration takes place and R the size of this region.

Following Equation 1.5 it is clear that at energies above the ankle the gyro-radius of a proton in the galactic magnetic field will exceed the size of the Galaxy disc (300 Mpc) and it is generally assumed that an extragalactic component in the spectrum of cosmic rays is the responsible for the flattening ($\gamma \sim 2.8$) observed at such energies.

1.2.3 Cosmic ray astronomy

Because of the influence of the galactic and extra-galactic magnetic fields on CRs propagation there is no possibility of a direct association with an astrophysical source but for the ultra high energy cosmic rays. But even at such high energies the expected difference between the

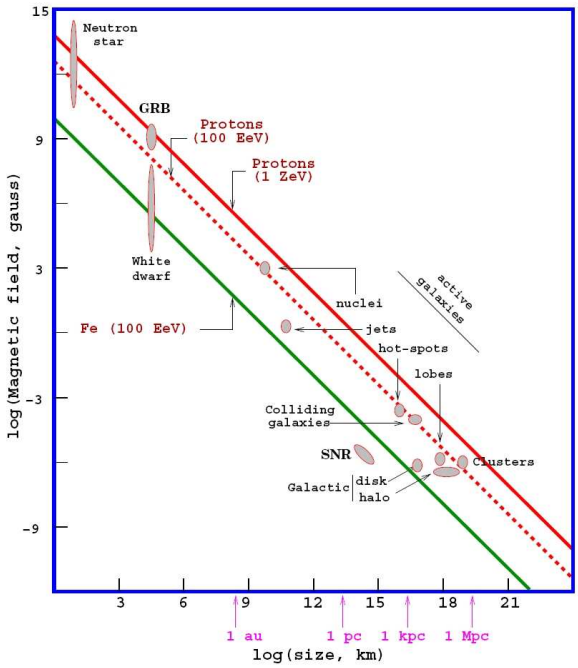

Figure 1.6: A Hillas' diagram displaying potential cosmic ray sources as a function of their size and magnetic field strength. Acceleration up to a given energy requires both conditions to be above the respective line.

direction of the source and direction of the UHECR can be of several degrees[3]. Moreover, the GZK effect limits the distance that UHECRs can travel before they interact with the ubiquitous CMB photons and lose their energy, to a few tens of Mpc, constraining the possibility to observe sources only from the local supercluster of galaxies. In addition, due to the tiny fluxes emitted at such energies (few events on Earth per km^2 per millennium for the most energetic particles) there is an important lack of statistics. Only instruments with extremely large collecting areas are, therefore, capable to perform astronomy with UHECRs [18]. The Pierre Auger Observatory [19] represents nowadays the major effort to detect UHECRs with enough statistics to study their composition and origin. The observatory was completed in 2008 and covers an area of over 3000 km^2 in Western Argentina. It consists of near 1600 water Cherenkov tanks spaced 1.5 km apart and four sites with six fluorescence telescopes for ground and air cosmic ray shower measurement respectively.

Early analysis using the UHECRs ($E > 55$ EeV) detected in 1.2 years of PAO operation provided evidence of anisotropy ($60\%^{+11}_{-13}$ correlation) in their arrival directions (Figure 1.7) and of correlation with nearby AGNs [20]. However, the significance of the observed correlation has been diluting as more data has been taken [21] and unambiguous source identification is still pending.

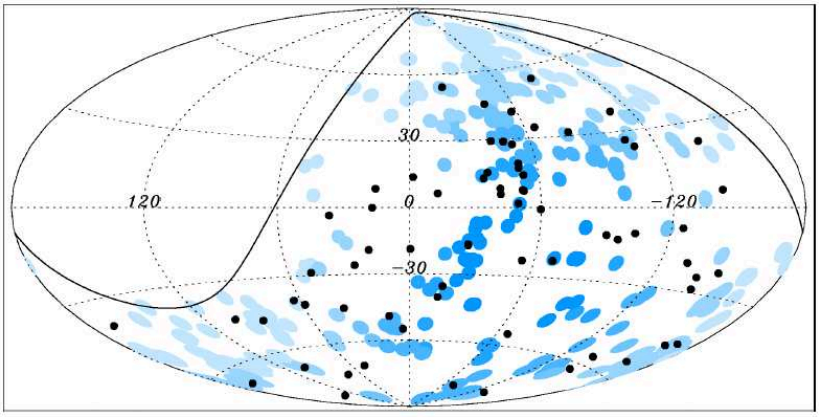

Figure 1.7: Sky map in galactic coordinates showing the 69 arrival directions of CRs with energy E >55 EeV detected by the Pierre Auger Observatory as black dots. Blue circles of radius 3.1° are centred at the positions of the AGNs. Taken from [21].

[3]This difference depends on the electric charge carried by the UHECRs, i.e., their composition, which still remains an open question.

1.3 Production of gamma-rays and neutrinos

Contrary to CRs, neutrinos and gamma-rays are not bent by magnetic fields in the intergalactic or interstellar medium and propagate linearly from the site of origin. Production of gammas and neutrinos would take place on the same astrophysical scenarios as those proposed for the emission of high energy cosmic rays under the likely assumption that, at the acceleration sites, a fraction of the CRs interact with ambient matter or photons (see Figure 1.8).

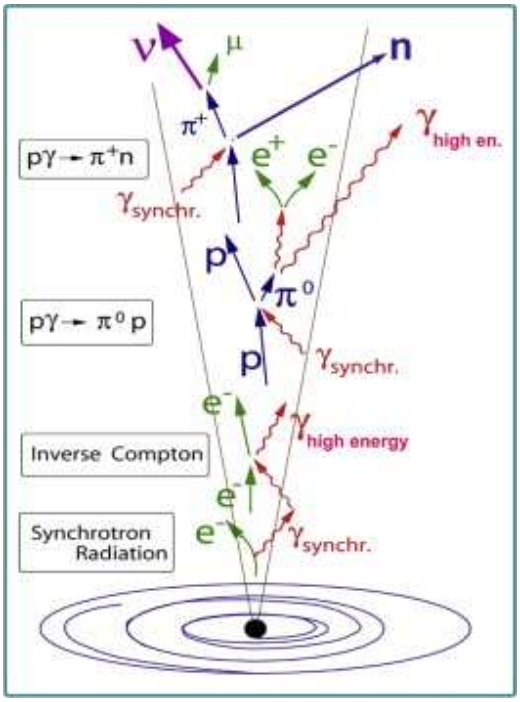

Figure 1.8: Gamma-ray and neutrino production in the jet of an AGN where both hadrons and electrons are accelerated.

Considering that not only hadrons but leptons can be accelerated as well, two emission models can be distinguished which have fundamental differences regarding the connection between cosmic rays, neutrinos and gamma rays. In the hadronic models, neutrinos are produced if the density of matter near the acceleration sites is enough to cause many hadrons to interact instead of escaping the source. The main interaction channels for hadrons in such scenarios are:

$$\begin{aligned} p + N &\rightarrow \pi + X \quad (\pi = \pi^{\pm}, \pi^0) \\ p + \gamma &\rightarrow \Delta^+ \rightarrow \begin{cases} \pi^0 + p \\ \pi^+ + n \end{cases}, \end{aligned} \tag{1.6}$$

with the subsequent decays:

$$\pi^+(\pi^-) \rightarrow \mu^+(\mu^-)\nu_\mu(\bar{\nu}_\mu), \;\; \mu^+ \rightarrow e^+\bar{\nu}_\mu\nu_e, \;\; \mu^- \rightarrow e^-\nu_\mu\bar{\nu}_e, \tag{1.7}$$

As both nucleon-photon and nucleon-nucleon interactions produce also neutral pions, which eventually decay emitting two photons ($\pi^0 \rightarrow \gamma\gamma$), hadronic models naturally predict both gamma-ray and neutrino emissions in the same acceleration sites which are candidates for high energy cosmic rays production.

On the other hand, the leptonic scenarios usually interpret gamma-rays as inverse Compton (IC) emission of energetic electrons. Targets for IC processes are ambient background photons as CMB or diffuse galactic star light radiation photons. If sufficient gas to scatter electrons is present, emission of gamma-rays can be also conducted via bremsstrahlung processes. Moreover, in leptonic models gamma-ray emission will be accompanied by X-ray emission via synchrotron radiation of accelerated electrons.

1.3.1 Gamma-ray astronomy

Gamma-rays are the most energetic photons of the electromagnetic spectrum. The Earth's atmosphere is entirely opaque to this radiation wavelengths, so first astrophysical gamma-ray observations were done using stratospheric balloons and, later, with spacecraft satellites. The SAS-2 and COS-B (launched respectively in 1972 and 1975) were the first gamma-ray dedicated missions opening the window to the *violent* universe. The Compton Gamma Ray Observatory (CGRO) was launched in 1991 and operated during nine years detecting gamma-rays with energies up to 30 GeV. The NASA's CGRO consisted of four specific experiments covering six decades in energy. Among them, the Energetic Gamma Ray Experiment Telescope (EGRET) was designed to observe the most energetic photons, completing a catalog with 271 high significance detections. However, because of its low angular accuracy, 170 of those have not been identified yet. The Fermi Gamma-ray Space Telescope, formerly referred to as the Gamma-ray Large Area Space Telescope (GLAST), is nowadays the successor of the CGRO and the Large Area Telescope (LAT) instrument that carries on-board is the heir of the EGRET

telescope. The LAT catalog of high energy γ-ray sources [22] is the largest one ever made in the range from 100 MeV to 100 GeV and includes more than 1800 sources (Figure 1.9). One of the most spectacular results provided by the Fermi telescope is the discovery of two gigantic gamma-ray bubbles extending 10 kpc in diameter north and south of the Galactic Centre (see Figure 1.10), which are suspected to be erupting from the super-massive black hole [23].

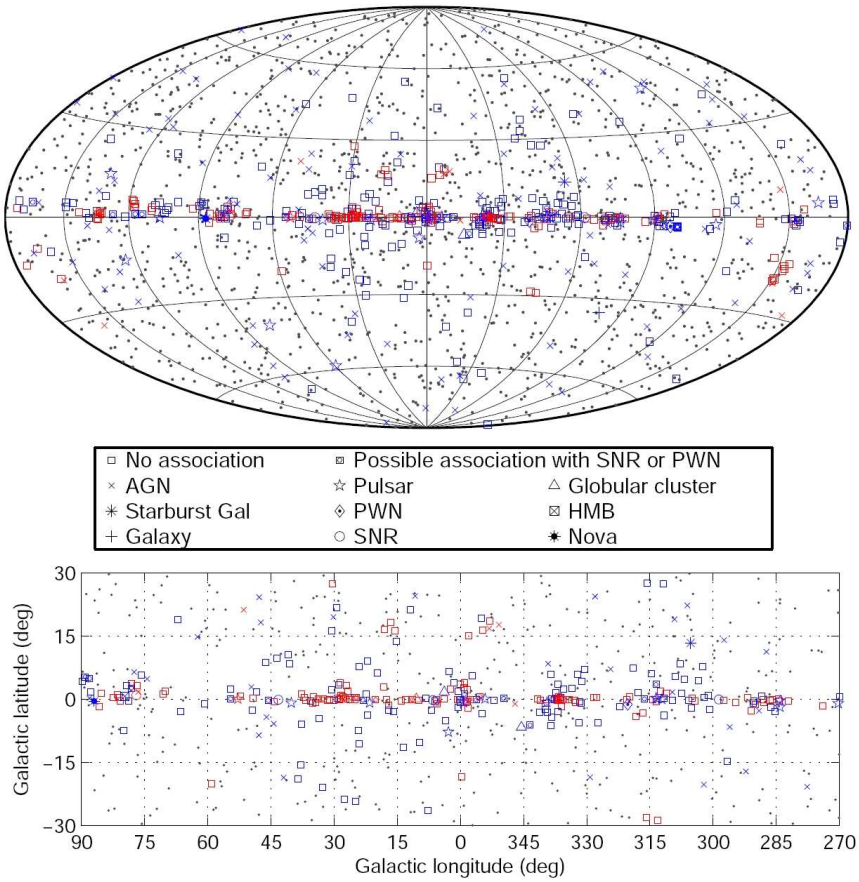

Figure 1.9: Full sky map (top) and blow-up of the inner Galactic region (bottom) showing flagged sources by source class. Identified sources are shown with a red symbol, associated sources in blue. Taken from [22].

Because of the relatively small collecting areas reachable with any on-board satellite instrument (as detection of falling fluxes would require) and because of the difficulty in constructing

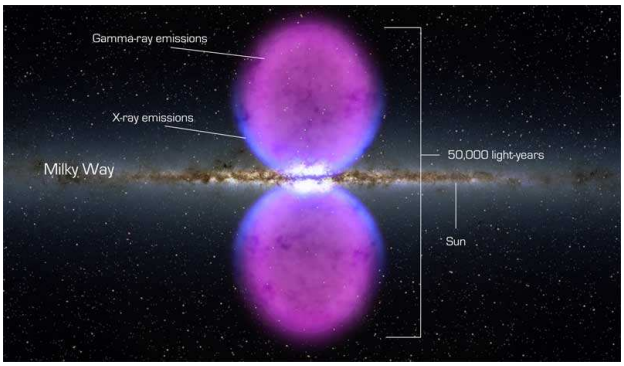

Figure 1.10: Gamma-ray bubbles erupting from the center of the Milky Way.

a suitable detector to stop them, gamma-rays above 100 GeV can not be detected in space. However, although γ-rays are completely absorbed before reaching the ground, the effects of the interaction of high energy photons with the atmosphere nuclei can be used to infer their properties allowing identification in ground-based experiments. In this sense, the development of the Imaging Atmospheric Cherenkov Technique (IACT), which is based on the collection of the Cherenkov photons emitted by the relativistic particles coming from γ-rays induced showers, represent one of the most important technical achievements regarding the high energy gamma ray astronomy. Observations with IACT instruments like VERITAS [24], MAGIC [25] or HESS [26] are of primary interest for neutrino telescopes because neutral pion decay processes produce photons in the energy range they cover, so high energy neutrinos can be expected to be emitted by the same astrophysical sources detected with IACTs.

As late 2002 the TeV gamma-ray sky consisted of only 6 confirmed sources, being the Crab Nebula the unique galactic. Such catalog was highly enriched with the Galactic Plane Survey performed by HESS during years 2004-2007 which lead to the discovery of tens of new TeV galactic sources [27]. The current number of gamma-ray sources, both galactic and extra-galactic, detected in the TeV range exceeds one hundred (Figure 1.11). This catalog could be soon widely extended by the foreseen Cherenkov Telescope Array (CTA) [28], which promises to improve the sensitivity of the current generation of IACTs by an order of magnitude and to detect photons with energies as high as 100 TeV.

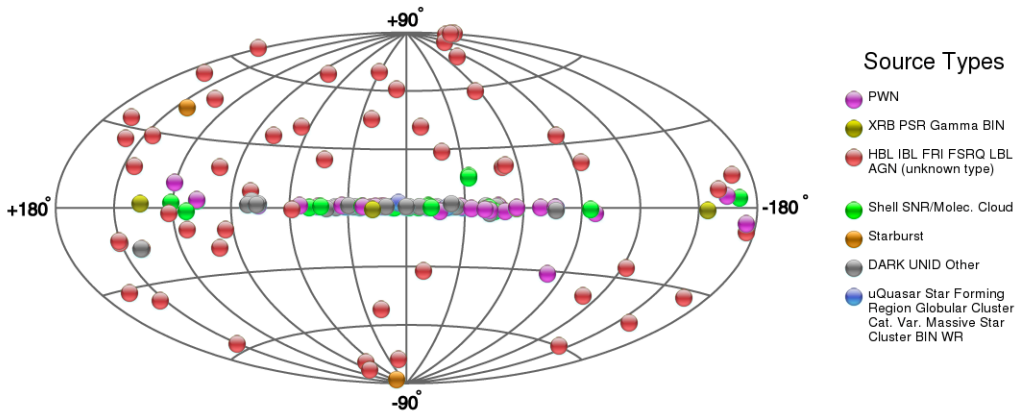

Figure 1.11: Sky map of TeV gamma-ray sources. Taken from [29].

1.4 Neutrinos as cosmic probes

The neutrino is a stable, almost massless and half-integer spin particle which only couples weakly to other particles. Its existence was postulated in 1930 by W. Pauli as a remedy to solve the problem of the continuum spectrum observed for the electron beta decay, but his prediction could not be confirmed until 1956 in an experiment performed by F. Reines and C. Cowan [30] using neutrinos produced in nuclear reactors. Actually, what they detected were neutrinos of the electron family. We know now that three neutrino flavors exist associated to three charged leptons: electron (e), muon (μ), and tau (τ).

Neutrinos are copiously produced in the fusion reactions that power the stars. Travelling from the Sun, billions of solar neutrinos each second reach every cm^2 of the Earth and traverse it without being noticed. The Universe is transparent to neutrinos, they do not suffer from interaction with ambient matter or radiation on their way to Earth (a property they share only with gravitational and radio waves) so they can bring us valuable information from cosmological distances. This is not the case for gamma-rays or protons, whose interactions with the ambient background light (CMB, IR and radio) limit their reach at high energies (see Figure 1.12). Neutrinos turn out to be, thus, the most adequate probes to reveal the sources that produce the high energy cosmic rays.

However, the only cosmic neutrinos that have been detected so far are of relatively low energy ($\sim$ MeV) and coming either from the SN1987A or the Sun. In 1987 a few electron neutrinos were simultaneously captured by three different experiments (11 in Kamiokande

[31], 8 in IMB [32] and 5 in Baksan [33]) from a 13 seconds long burst. These neutrinos were produced in the supernova SN1987A explosion of a supergiant star in the Large Magellanic Cloud. Detection of neutrinos from the Sun has been proven of great importance since they provided the first evidence of neutrino oscillations, later confirmed by dedicated experiments.

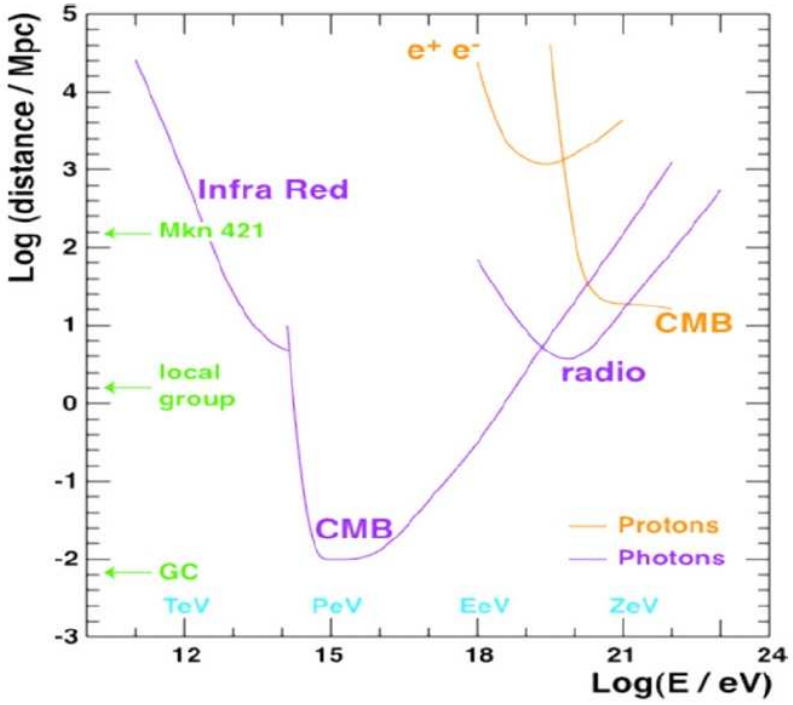

Figure 1.12: Absorption length as a function of the photon and of the proton energy.

1.4.1 Oscillation of neutrinos

Neutrinos oscillate while propagating. This is a natural phenomenon trough which a neutrino of a given flavor *mutates* into a neutrino of a different flavor, i.e. $\nu_l \rightarrow \nu_{l'}$, where $l(l') = e, \nu, \tau$ are the three possible flavors of neutrinos. The first evidence of the oscillation effect was provided by the study of the solar neutrinos collected with the 650-ton radiochemical detector installed in the Homestake mine in the 1960's [34]. This was an underground chlorine-based experiment designed to capture electron neutrinos through the inverse-electron capture reaction

$$^{37}Cl + \nu_e^{\rm solar} \rightarrow ^{37} Ar + e^-. \tag{1.8}$$

The experiment, led by Raymond Davis Jr., revealed a deficit in the solar neutrino flux with respect to the predictions of the Standard Solar Model (SSM) [35], the theory of stellar structure and evolution. The deficit observed by Davis was confirmed later by other neutrino experiments establishing the named *solar neutrino problem*. A theoretical explanation for the neutrino deficits is provided by the neutrino oscillation quantum mechanism.

First proposed by Bruno Pontecorvo in 1957 [36], this mechanism allows the neutrino flavor changing while they propagate through the space. In this scheme, weak flavor eigenstates (ν_l) are a linear combination of mass eigenstates (ν_m) through the elements of the so-called mixing matrix U_{lm}. The connection between flavor and mass eigenstates evolves in time as neutrino propagates following the relation:

$$|\nu_l(t)>= U_{lm} e^{-iE_m t} |\nu_m>, \tag{1.9}$$

where $m = 1, 2, 3$ and E is the neutrino energy. Considering the simple case of oscillation between two neutrinos the probability for a neutrino to oscillate from an initial flavor l to a flavor state l' in a time t is

$$P(\nu_l \rightarrow \nu_{l'}) = |<\nu_{l'}(t)|\nu_l(t)>|^2 = \sin^2(2\theta)\sin^2\left(1.27\Delta m^2 \frac{L}{E}\right), \tag{1.10}$$

where *L* is the distance (in km) travelled by the neutrino from the production site to where detection occurs, *E* is the energy (in GeV) of the neutrino propagation eigenstate of mass m, Δm^2 is the quadratic mass difference between the neutrino flavors considered, and θ is the so-called mixing angle.

The neutrino oscillation effect[4] has important implications for neutrino astronomy. Following the pion decay production of neutrinos discussed in Section 1.3, the expected neutrino fluxes of different flavors produced by a cosmic source are in the ratio $\nu_e : \nu_\mu : \nu_\tau = 1 : 2 : 0$ (combining ν_l and $\bar{\nu_l}$). However, the effect of neutrino oscillations will result in a flux at Earth in the ratio $\nu_e : \nu_\mu : \nu_\tau = 1 : 1 : 1$ as the result of neutrino flavor changing [38]. Furthermore, since tau neutrinos with energy $E_{\nu_\tau} > 100$ GeV are absent in the atmospheric

[4] See [37] for an updated summary of the experimental status.

neutrino background, the identification of such neutrinos would be a strong evidence of their astrophysical origin.

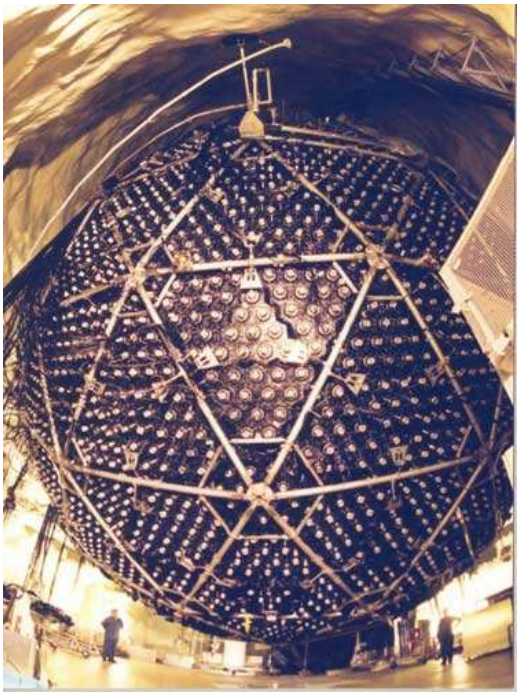

Figure 1.13: Fish-eye photo of the SNO detector and cavity.

1.5 Candidate sources of high energy neutrinos

There is no evidence, so far, of correlation of cosmic rays with astrophysical scenarios, but a large number of gamma-ray sources have been discovered by high energy photon observatories. Detection of high energy cosmic neutrinos in association with a gamma-ray source will be an unambiguous demonstration in favor of hadronic mechanisms, and a strong evidence of the identification of the powering sites of CRs. Some of the most promising sources of high energy neutrinos, both galactic and extra-galactic, are described below. We focus on sources for which gamma-ray emission has been observed in the TeV energy range. In addition, it should be always considered that new detection channels usually bring new discoveries: the potential "unknown unknowns" that would only be discovered using neutrinos as cosmic probes.

1.5.1 Galactic sources

Since the first detection of a TeV gamma-ray source in 1989 [39], hundreds of them have been cataloged up to date. The list of neutrino candidate sources in our galaxy is broad. The description of the most relevant ones is given below.

- **Supernova remnants**

  Supernovae are extremely luminous phenomena resulting from the explosion of a star with sufficient mass. During its explosion, much or all of the star material is expelled at velocities up to 10% of the speed of light, driving a shock wave into the surrounding interstellar medium. This shock wave sweeps up an expanding shell of gas and dust namely a supernova remnant (SNR). Acceleration of particles may occur in the SNR via the Fermi mechanism, which predicts a power law energy spectrum of E^{-2} for their emissions that correctly fits the cosmic rays energy power below the knee. When the result of a supernova is a neutron star, charged particles can gain additional energy due to the strong magnetic fields produced.

  SNRs are considered the best candidates for the acceleration of cosmic rays up to the knee [40], although this theory is not free from some difficulties [41]. One of the brightest objects in the southern gamma-ray TeV sky is the SNR RX J0852.0-4622, also known as Vela Jr., for which emission of photons exceeding 10 TeV energies has been detected [42]. The SNR RX J1713.7-3946, first observed by the CANGAROO experiment [43], is subject of debate about the leptonic or hadronic nature of its γ-ray spectrum. While first analysis claimed a leptonic origin, posterior evaluations with higher statistics let room for the possibility of hadronic acceleration [44] [45]. Indeed, the expected neutrino flux from SNR RX J1713.7-3946 is calculated in [46] using H.E.S.S. measurements and assuming that all the observed gamma rays stem from π^0 decays. Based of these estimates, detection seems possible after several years of data taking with a detector of 1km^3 instrumented volume. However, the more recent observation by the Fermi LAT [47] is well in agreement with emission scenarios in which the dominant process is the Inverse Compton scattering of ambient photon fields of relativistic electrons accelerated in the shock front (see Figure 1.15), a result which diminish the expectations for detecting the emission of neutrinos from this particular source.

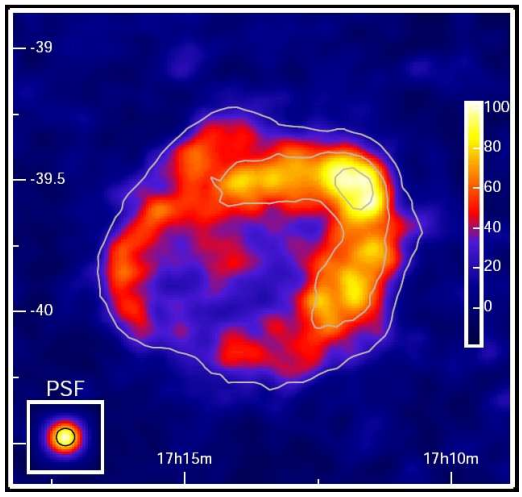

Figure 1.14: Gamma-ray image of SNR RX J1713.7-3946 obtained by H.E.S.S. with data from years 2004 and 2005. The overlaid light-gray contours illustrate the significance of the different features. The levels are at 8, 18, and 24 σ. Taken from [48].

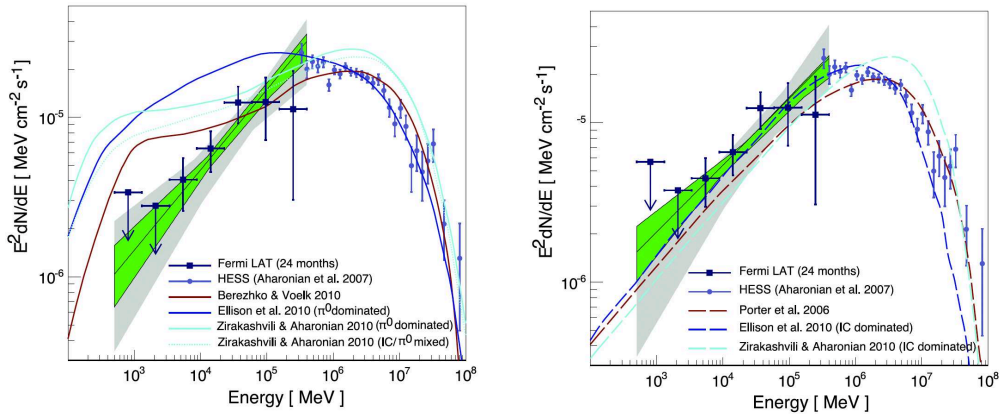

Figure 1.15: Energy spectrum of RX J1713.7-3946 in gamma rays. The Fermi-LAT detected emission is shown in combination with the energy spectrum detected by H.E.S.S. and compared with hadronic (left) and leptonic (right) models. Taken from [47].

- **Pulsar wind nebulae**

  A Pulsar Wind Nebula (PWN) is a special case of a SNR characterized by the presence of a pulsar star in its center blowing out jets of very fast moving material into the nebula. The emission of these sources is produced in the shock region generated by the interaction of the particle wind with the surrounding material. The radio, optical and X-ray observations suggest a synchrotron origin for these emissions. Two morphological types of PWN can be distinguished depending on the nature of the external pressure confining the pulsar wind. The first type shows a toroidal structure around the pulsar with one or two jets along the torus axis. The most representative source is the Crab nebula which was the first TeV gamma-ray source ever detected [39]. Its gamma-ray production is well described by purely electromagnetic models and therefore neutrino fluxes are not expected from such kind of sources. The second type is characterized by a cometary structure with the pulsar close to the comet apex, resulting of the SNR expansion in an inhomogeneous medium. The first source of this second PWN type to be discovered was Vela X (Figure 1.16). Again, the study of the TeV γ-ray emissions from Vela X indicates that inverse Compton up-scattering of cosmic microwave background radiation (or synchrotron) photons by energetic electrons is very likely to be the mechanism responsible. Despite the most successful models for PWN to date are all purely electromagnetic, the existence of a significant fraction of nuclei in pulsar winds has been suggested [49]. In such scenario the TeV emission may be dominated by the decay of pions produced in the interactions of these nuclei and yield a significant production of neutrinos [50].

- **Microquasars**

  Microquasars[5] are X-ray binary systems featuring the emission of relativistic jets observed in the radio band [52]. The engine of a microquasar is thought to be the accretion of matter falling from one component (usually a regular star) to its counterpart (a compact object such as a neutron star or a black hole) forming an accretion disc (Figure 1.17). Microquasars are good candidates for baryonic acceleration up to 10 PeV energies, an hypothesis strengthened by the observation of iron X-ray lines [53]

[5] The name comes from the fact that they result morphologically similar to the AGNs (see Section 1.5.2)

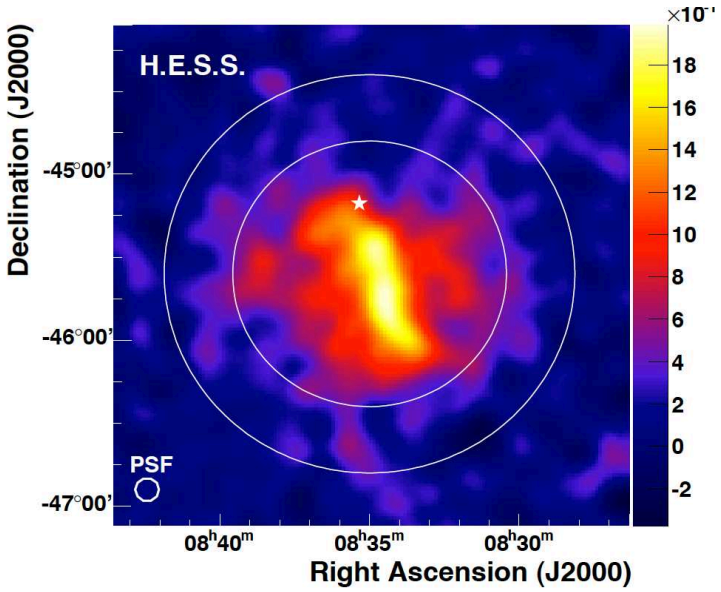

Figure 1.16: Very High Energy (VHE) gamma-ray brightness of Vela X as observed by H.E.S.S. [51].

in their jets, which implies the presence of relativistic nuclei. TeV gamma-ray emission has recently been reported from the X-ray binaries LS 5039 and LS I+61 303 [54] [55]. Also the Fermi Large Area Telescope (LAT) observed the gamma-ray emission in coincidence with the position of the microquasar Cygnus X-3 [56]. The rapid cooling of TeV electrons in the dense radiation fields associated with such objects suggests an hadronic origin for the gamma-radiation. While the gamma-ray emission from these sources is relatively weak, they are promising candidates for neutrino emission because of the strong gamma-ray absorption that likely occurs within them.

- **Galactic Centre**

  The centre of the Milky way is of primary interest for high energy neutrino astronomy and particularly appealing for a neutrino telescope operating in the Mediterranean Sea, because at such latitudes the Galactic Centre lies fully within the telescope field of view. The survey of the inner part of the Galactic Plane performed by H.E.S.S. [27] revealed 14 new TeV γ-ray sources including SNRs, PWNs, X-ray binaries, as well as sources with no known counterpart. One of the best candidates from this region is the super-massive black hole Sagittarius A*, observed as a point-like source by H.E.S.S.

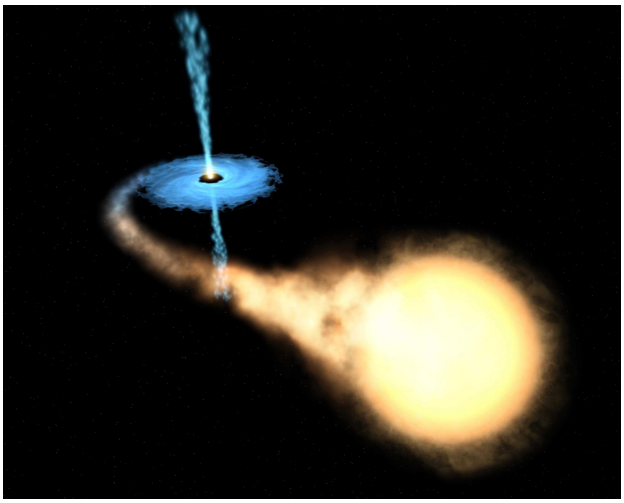

Figure 1.17: Artistic conception of a X-ray binary system where a black hole accretes matter from a companion giant star.

However, detecting a diffuse neutrino emission from the Galactic Centre (that appears to be correlated with the presence of giant molecular clouds in the environment) seems more likely to occur before the identification of an individual source.

1.5.2 Extragalactic sources

The first detection of an extragalactic TeV γ-ray source was done in 1992 in coincidence with Mrk 421 [57]. More than 50 extra-galactic sources producing VHE gamma-ray emission have been observed to date. Most interesting ones are the Active Galactic Nuclei and Gamma Ray Bursts. An important effect to take into account is that the observed gamma-ray spectrum from extragalactic sources is steepened due to absorption by the extragalactic background light (EBL), which has no effect on neutrinos.

- **Active galactic nuclei:**

  The Active Galactic Nuclei (AGNs) are bright objects located at the center of certain galaxies (namely active galaxies) that exhibit a very high luminosity over a wide range of the electromagnetic spectrum. The mechanism responsible of the up to $L_\gamma \sim 10^{47}$ erg/s luminosities observed for AGNs is most likely to be the accretion of matter by a super-massive black hole ($10^6 - 10^9 \mathrm{M}_\odot$) at the center of the host galaxy. There is

empirical evidence of correlation of the black hole mass and the velocity dispersion of the galaxy bulge [58] [59]. Apart from that, it is well known that accretion of matter is a very efficient mechanism to transform kinetic energy into radiation, as AGNs related emissions require. The angular momentum of the plasma of accreted matter falling into the black hole (forming a disc of dust) creates strong magnetic fields that cause charged particles to be ejected into the interstellar medium in two opposite directions producing the jets that characterize this type of astrophysical objects.

AGNs are conventionally divided, according to the intensity of their radio emission with respect to their optical flux, into two classes referred to as radio-quiet and radio-loud AGNs. Further sub-classification is based on their luminosity and on the different features they present depending on the angle between the rotation axis of the black hole and the observer (Figure 1.18).

Most of the extragalactic steady sources known to be high energy γ-ray emitters are radio-loud AGNs with one jet pointing towards the observer at small angles (Blazars). The spectrum of these objects is characterized by two broad peaks, one in the mm-soft X-rays and the other in the MeV-GeV band. While the origin of the lower energy peak is understood as synchrotron emission of leptons in the relativistic jet, the mechanism responsible for the high energy peak emission is still an open question and both IC scattering and hadronic processes have been suggested. Most of the blazars we know to emit gamma-ray are high frequency peaked BL Lac objects (HBLs). However, LBLs (low frequency peaked) are more favored for neutrino production than HBLs mainly because their higher photon density [60].

- **Gamma-Ray bursts**

  The most luminous and energetic phenomena ($\mathcal{O}(10^{51} - 10^{54})$ erg) observed in the universe are the Gamma-Ray bursts (GRBs). They consist of short (from milliseconds to minutes) flashes or bursts of γ-rays produced in the collapse of a massive star into a black hole (Figure 1.19). The Vela satellites, designed to detect gamma radiation pulses from nuclear weapons tests, observed the first GRB flash in 1967. The Burst and Transient Source Explorer (BATSE) instrument on-board the CGRO revealed an isotropic distribution of GRBs (Figure 1.20) and thus their extragalactic origin.

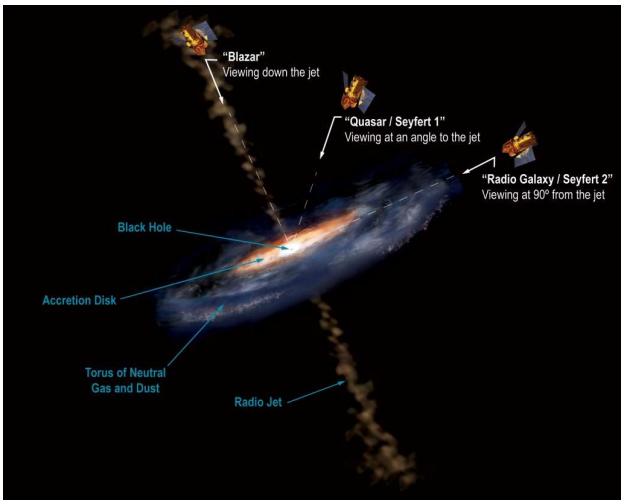

Figure 1.18: Illustration showing the different features of an active galactic nucleus, and how the viewing angle determines what type of AGN is observed.

Leading models for GRBs assume that a fireball [61], produced in the collapse, expands with a highly relativistic velocity (powered by the radiation pressure) ejecting large amounts of mass within a short time interval and forming successive plasma shells. When the outer shells slow down they are hit by the inner shells and internal shock fronts pile up. Along these fronts, particles can be accelerated up to very high energies. The observed gamma-rays would originate from IC and synchrotron emission of high energy electrons, while high energy neutrons would escape the fireball and later decay to protons, constituting the high energy cosmic ray flux observed at Earth. The accelerated protons will lose energy through photo-meson interaction with ambient photons yielding a significant production of pions which eventually will decay in neutrinos [62] [63]. It should be noticed that, as transient sources, GRBs detection has the advantage of being practically background free since neutrino events coming from a GRB should be correlated both in time and direction with γ-rays.

- **Starburst galaxies**

  The starburst galaxies are characterized by the existence of regions with a very high star formation rate in comparison with the typical rates observed in regular galaxies. From these regions, a galactic-scale wind blows out large amounts of mass into the intergalactic medium driven by the collective effect of supernova explosions and massive

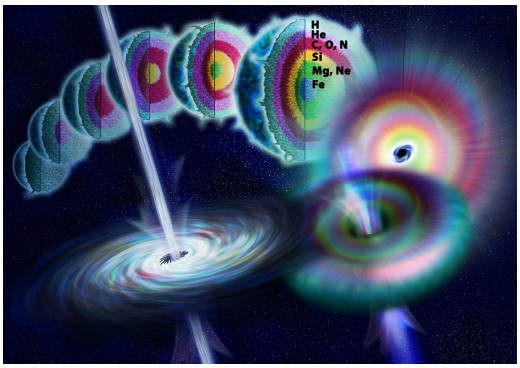

Figure 1.19: Artistic conception of the evolution of a massive star collapsing to a black hole and producing a GRB.

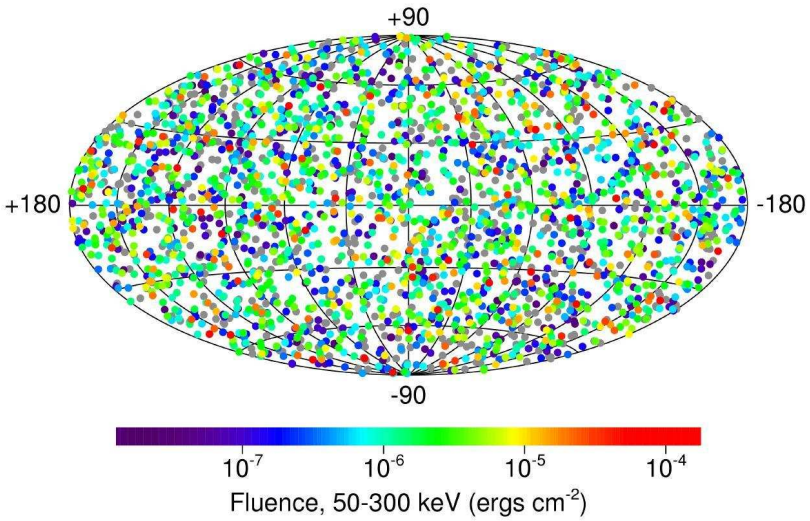

Figure 1.20: Galactic coordinates and fluence of the 2074 GRBs detected by BATSE between 1991 and 2000. Taken from [64].

star winds. The starburst galaxies M82 (Figure 1.21) and NGC253 have been recently detected by the IACTs H.E.S.S. and VERITAS [65, 66]. The burst of star formation indicates a high dense region of matter. In such a dense region, accelerated protons would interact to produce pions leading the emission of neutrinos. In some cases, since only neutrinos would be able to escape from the high dense regions, starburst galaxies will be hidden sources of CRs and thus purely neutrino accelerators.

Figure 1.21: A ground- and space-based HST/WIYN composite image of M82 and its optically bright superwind.

1.6 Neutrino telescopes

We review here the neutrino telescope that have been operative in the past, those which are operative at present and the projected ones. The basic concepts of the detection technique they employ and the description of the ANTARES detector are discussed in detail in the next chapter.

The DUMAND (Deep Underwater Muon and Neutrino Detection) experiment based in Hawaii in 1976 was the pioneer project to attempt the construction of a neutrino telescope. Although the detector was never completed because of the lack of funding, the technical studies performed during this period provided a valuable experience for the next generation of neutrino telescopes. The first project to demonstrate the feasibility of the construction and operation of an underwater neutrino telescope was BAIKAL. Located at a depth of

1100 m in the Russian Lake Baikal, the current detector (referred to as NT200+) consists of 12 strings holding 192+36 photo-multiplier tubes in two separated configurations. The AMANDA collaboration (Antarctic Muon and Neutrino Detector Array) [67] started in 1993 the construction of a neutrino telescope embedded in the Antarctic ice at the Amundsen-Scott station. The detector, which in its final configuration (AMANDA-II) consisted of 677 optical modules arranged in 19 strings, operated for more than 5 years.

According to the theoretical predictions on cosmic neutrino fluxes [68] the natural scale for a neutrino telescope is the km^3 instrumented volume. The IceCube collaboration has constructed under the Antarctic ice the first km^3 scale neutrino telescope. In addition, two solid projects exist for the installation of a kilometer-scale array in Lake Baikal and of a multi-km^3 detector in the Mediterranean Sea.

- **IceCube**

  Based on the experience gained with the AMANDA project, the IceCube collaboration completed in 2011 the installation of the world's largest neutrino telescope [69] [70]. This observatory is located at the geographic South Pole and uses the deep Antarctic ice for Cherenkov light detection covering a surface of about $1km^2$. Figure 1.22 shows a schematic view of the detector. The IceCube fundamental detection element is the Digital Optical Module (DOM) consisting of a photomultiplier tube and the readout electronics. There are 5160 DOMs placed in a lattice structure composed by 86 strings at a depth from 1450 m to 2450 m under the ice. The horizontal layout is hexagonal with a spacing between strings of 125 m and of 70 m for the 6 strings constituting the IceCube deep core for a low energy events increased detection efficiency. The observatory also includes a surface array (IceTop) for extensive air shower measurements on the cosmic ray composition and spectrum, which consists of 160 tanks placed in pairs above each detector string.

- **KM3NeT**

  The KM3NeT consortium [71] represents the major effort to achieve the construction of a multi-km^3 scale neutrino telescope in the Mediterranean Sea. The future detector will complement the observations of the IceCube experiment with an unprecedented angular resolution of 0.1 degree at high energies. In particular, it will have an optimal visibility of one of the most interesting regions of the sky for the neutrino astronomy, the Galactic

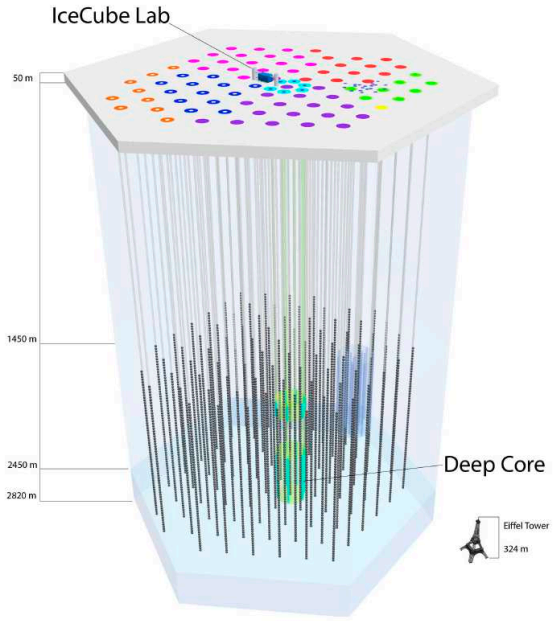

Figure 1.22: The IceCube Neutrino Observatory.

Centre. The Conceptual Design Report [72] and the Technical Design Report [73] have been published. A preliminary scheme of the detector configuration is shown in Figure 1.23. In its current design concept the detector would consist of 12,800 optical modules on 610 strings covering an instrumented volume of approximately 5 km^3. The optical modules are based on a novel approach of integrating a sizeable number of 31 small PMTs of about 75 mm cathode diameter into one optical sensor, which is referred to as the multi-PMT.

- **GVD**

  The Baikal Collaboration aims the installation of a Gigaton Volume Detector (GVD) in the Lake Baikal [74]. The instrument would consist of strings carrying 24 optical modules (housing 10" photomultipliers) spaced uniformly from 900m down to about 1250 m depth (Figure 1.24). This design results in a relatively flexible structure, which allows for rearranging the clusters and meets better the deployment conditions for the ice. Simulations have been performed for 96 strings in 12 clusters and a total of 2304 OMs. In April 2011, a prototype cluster with three mini-strings and all key elements of

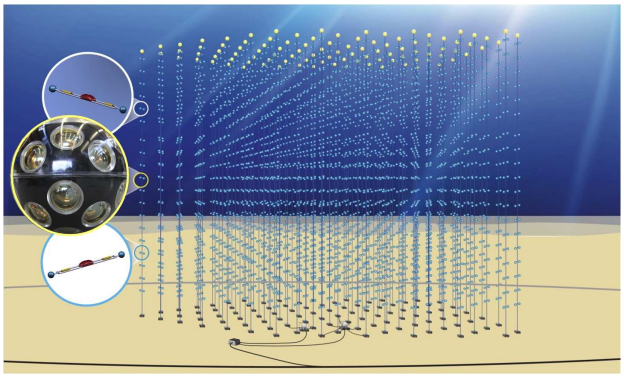

Figure 1.23: Preliminary scheme of the future KM3NeT detector design including a picture of the multi-PMT.

DAQ electronics and the communication system was deployed.

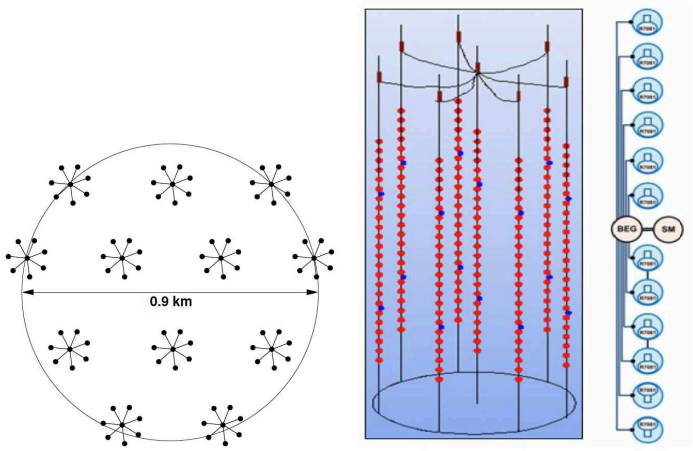

Figure 1.24: The Baikal Gigaton Volume Detector. Arrangement of the 12 clusters (left), one cluster (center) and schematic view of a string section (right).

2

The ANTARES neutrino telescope

Neutrino telescopes are a special kind of Cherenkov detectors consisting in a large number of photomultipliers arranged in a lattice structure placed at high depths in natural water or ice. We review in this chapter the basic principles of operation of a neutrino telescope, describing in detail the ANTARES detector.

2.1 Neutrino interactions

Neutrinos interact with matter through the weak nuclear force. In the energy range of interest for neutrino astronomy the interaction is dominated by the inelastic scattering on a target nucleon. Depending on the weak gauge boson exchanged two types of currents can be distinguished:

$$\begin{aligned} \nu_l(\bar{\nu}_l) + N &\longrightarrow l^-(l^+) + X \qquad \text{charged current (CC)} \\ \nu_l(\bar{\nu}_l) + N &\longrightarrow \nu_l(\bar{\nu}_l) + X \qquad \text{neutral current (NC)} \end{aligned} \tag{2.1}$$

where N is the target nucleus and X is, in general, one or more hadrons forming a shower. Charged current (CC) interactions are mediated by the $W^{\pm}$ bosons and the products of the reaction include a charged lepton. Neutral current (NC) reactions occur when a Z^0 is

exchanged and produce a neutrino in the final state. The NC interaction may be detectable by looking for the associated hadronic cascade, but in this work the CC interactions are the focus.

The differential cross section of the deep inelastic charged current interaction of the neutrino can be written as [75]

$$\frac{d^2\sigma_{\nu N}}{dxdy} = \frac{2G_F^2 M E_\nu}{\pi} \frac{M_W^4}{(Q^2 + M_W^2)^2} [xq(x,Q^2) + x(1-y)^2 \overline{q}(x,Q^2)], \tag{2.2}$$

where G_F is the Fermi constant; M and M_W are the nucleon and the $W^\pm$ masses; E_ν is the incident neutrino energy; Q^2 is the square of the invariant momentum transfer between the neutrino and the lepton; x and y are the so-called Björken scaling variables, and $q(x,Q^2)$ and $\bar{q}(x,Q^2)$ the parton distribution functions for quarks and anti-quarks. Figure 2.1 shows the dependence with the neutrino energy of the νN cross sections. As it can be seen, the interaction rates increase with the energy of the neutrino leading to a better chance for observation and compensating partially the expected decrease of the cosmic flux of neutrinos at high energies.

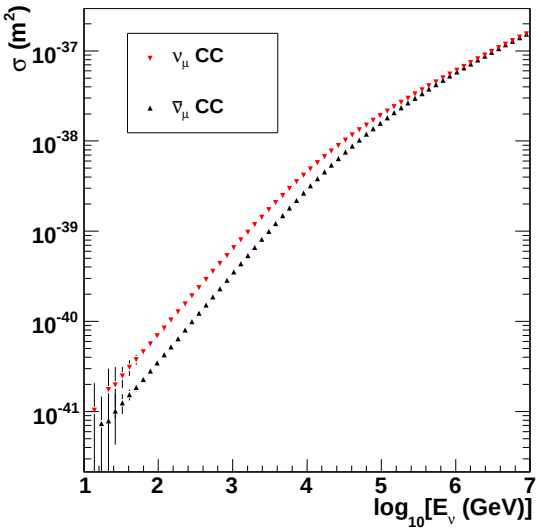

Figure 2.1: Muon neutrino and muon anti-neutrino interaction cross sections as a function of the neutrino energy according to CTEQ6-DIS [75] parton distribution.

Different event topologies are associated with the CC interaction (see Figure 2.2). Concerning neutrino astronomy the most interesting one is characterized by the production of a muon capable of traveling very large distances in matter. In such cases, interaction vertex tens of kilometers away from the detector can be located, giving a clean experimental signal which allows the precise reconstruction of the muon track. The average angle between the muon and the neutrino can be approximated by

$$< \theta_{\mu,\nu} >= \frac{0.64^{\circ}}{(E_{\nu}/TeV)^{0.56}} \tag{2.3}$$

at high energies of the neutrino ($E_{\nu} > 10$ TeV) the neutrino direction and the muon track are almost collinear, and sub-degree accuracies can be achieved.

Electron neutrinos and tau neutrino interactions can be also detected. The electron neutrino events produce an electron (which induces an electromagnetic cascade) and a hadronic cascade. In this case, the electron produces a short-track event. The tau neutrino interaction produces a tau which, at energies below $\sim$ 1 PeV, decays immediately and, therefore, it can not be separated from the subsequent shower. On the contrary, when the tau neutrino energy is high enough the resulting tau particle can travel several meters before decaying producing a second shower and yielding a pattern known as double bang which can be identifiable in a wide energy range. It may happen that the hadronic or electromagnetic cascade of the tau decay is not contained in the detector, so it will not be possible to distinguish it from a muon neutrino signal. Although these signatures are potentially background free events the expected rate is too low.

2.2 Cherenkov radiation

The emission of the Cherenkov radiation occurs inside a dielectric medium when it is crossed by a charged particle traveling with speed greater than the phase velocity of light in the medium. This effect was discovered in 1934 by the Russian physicist Pavel A. Cherenkov and awarded with the Nobel prize in Physics in 1958. The phenomenon is the result of the polarization of the medium molecules, which are displaced from equilibrium by the electromagnetic field of the passing charged particle. Emission of photons take place when the electrons of the dielectric restore themselves to the equilibrium, creating a coherent radiation which propagates along the relativistic particle track with a characteristic angle θ_c given by

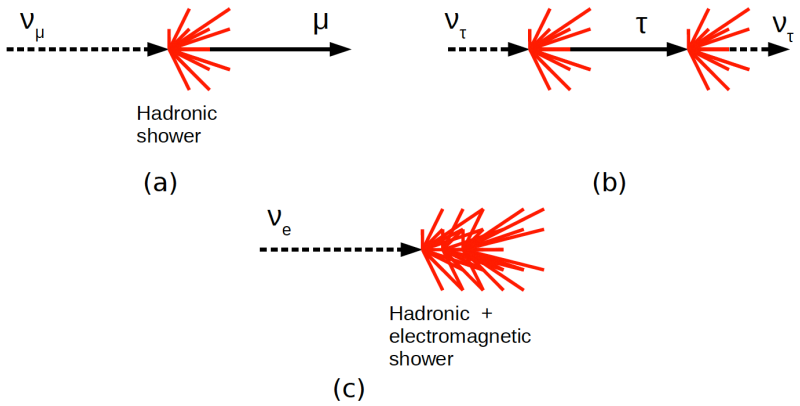

Figure 2.2: Event topologies in CC neutrino interactions: a) the interaction of a muon neutrino produces a hadronic shower plus a muon, b) tau neutrino interactions yield a τ particle which promptly decays into a ν_τ and, at sufficient energy, produces a double bang signature, c) when an electron neutrino interacts, both an electromagnetic and a hadronic shower are produced.

$$\theta_C = \arccos(\frac{1}{\beta n}), \tag{2.4}$$

where β is the velocity of the particle expressed as a fraction of the velocity of light in vacuum an n is the refractive index of the medium (figure 2.3).

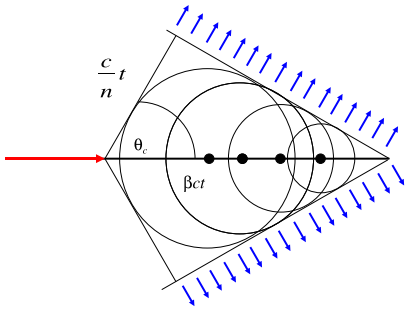

Figure 2.3: Cherenkov light emission.

In the approximation of $\beta = 1$ and taking n=1.38 (at 469 nm) from measurements on the ANTARES site [76], the Cherenkov angle in deep sea water is about $43°$. The number of photons N_γ emitted per unit of length x and wavelength λ by a particle with charge z traveling at speed β in a medium of refractive index n is given by

$$\frac{d^2N}{dxd\lambda} = \frac{2\pi\alpha z^2}{\lambda^2}\left(1 - \frac{1}{\beta^2 n^2}\right), \tag{2.5}$$

where α is the fine-structure constant. Consequently shorter wavelengths contribute more significantly to the Cherenkov radiation. In the wavelength range between 300 and 600 nm (where the efficiency of the ANTARES photomultipliers is maximum) this amounts to 3.5×10^4 photons emitted per meter of track.

2.3 Detection principle

Neutrino telescopes operate by observing the Cherenkov light induced by the leptons emerging from the CC interactions of neutrinos with the matter. The detectors themselves consist, typically, of a matrix of light sensors distributed in a transparent medium. Because of the low expected fluxes of cosmic events and the small interaction cross section of the neutrino, very large instrumented volumes are required. The use of natural mediums like sea/lake water or ice was first proposed by Markov [77] in 1960. Figure 2.4 depict the detection principle for an underwater Cherenkov detector.

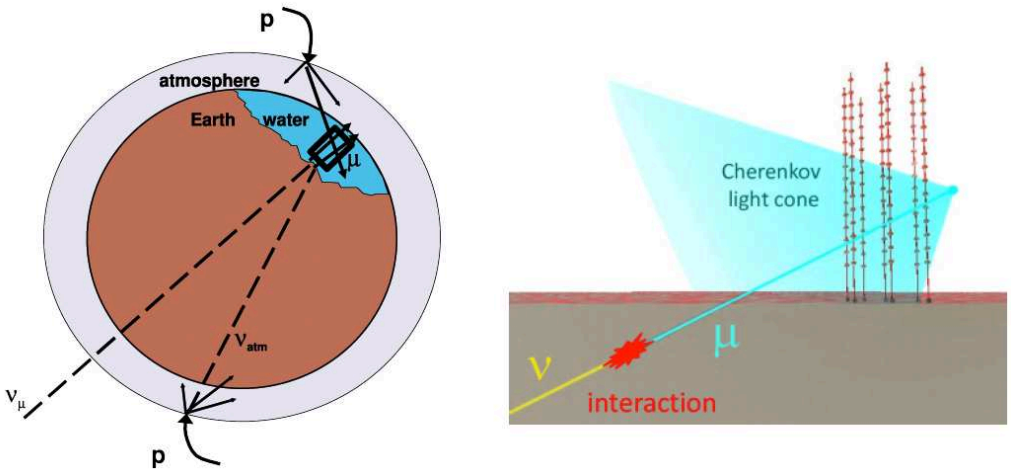

Figure 2.4: Description of the detection principle of a neutrino telescope. Atmospheric muons and atmospheric neutrinos produced by the interactions of cosmic rays in the atmosphere constitute the main source of physical background. Cosmic neutrinos (the searched signal) interact with the matter near the detector after traversing the Earth. The resulting muon induces a Cherenkov light cone which is detected by an array of photomultiplier tubes.

- **Physical background**

  Cosmic rays arrive continuously to the Earth producing air showers of secondary particles in their interaction with the atmosphere nucleons. The resulting hadronic cascades are composed, among others particles, of charged pions which decay producing the so-called atmospheric muons and atmospheric neutrinos, that represent the main source of physical background for a neutrino telescope.

  Atmospheric muon flux at the Earth's surface is several orders of magnitude larger than the flux of atmospheric neutrinos (figure 2.5). Muons with sufficient energy can penetrate the atmosphere and up to several km of sea water reaching the detector. In order to reject as much atmospheric muons as possible, neutrino telescopes are installed at large depths and look downward using the Earth itself as a filter. This means that only events reconstructed as upward going tracks are selected, so that a neutrino telescope covers the opposite half of the sky which would be visible for an optical telescope. However, bundles of parallel muons coming from the same cascade may be mis-reconstructed as upgoing events and can only be removed by applying tight requirements on the quality of the reconstruction.

  Atmospheric neutrinos, on the other hand, can fully cross the Earth and produce a muon which will be detected as an upward going event. They constitute an unavoidable source of background which can only be discriminated by looking for accumulation of events at a certain direction and on the basis of the different spectral index predicted for the atmospheric neutrinos and the cosmic signals (or using the time information of the events when searching for transient sources).

- **Muon propagation and reconstruction**

  As mentioned before, muons with sufficient energy can completely traverse the detector giving an experimental signal that allows an accurate reconstruction of the muon trajectory, which will be closely correlated with the neutrino direction. A muon passing through matter loses energy by ionization and radiative processes. In the ionization process, the muon interacts with the electric field generated by the electron cloud of the atom. In the radiative processes (bremsstrahlung, pair production and photo-nuclear interactions) the muon interacts with the nuclear electric field of the atom. The muon energy loss per unit of length (x) can be parameterized as

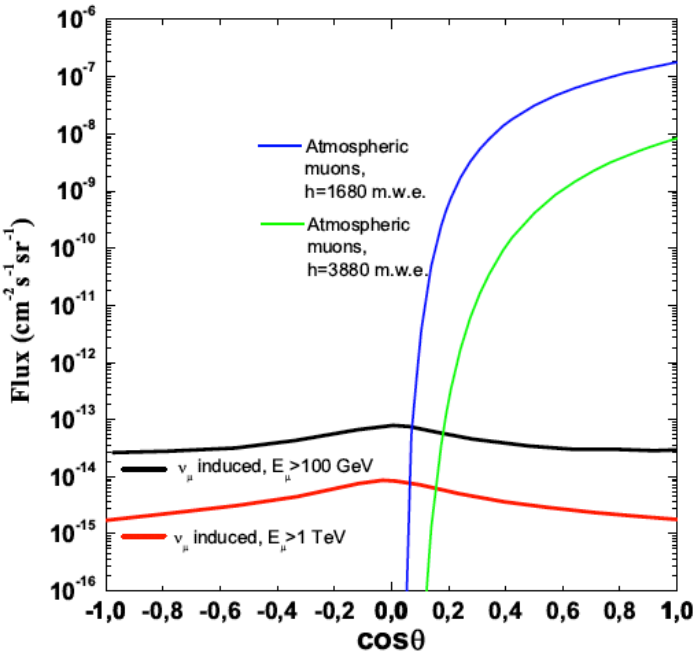

Figure 2.5: Muon flux due to atmospheric muons (computed according to [78]) at two different depths and to atmospheric neutrinos (from [79]) for two different muon energy thresholds as a function of the cosine of the zenith angle.

$$-<\frac{dE}{dx}>=\alpha(E)+\beta(E)\times E, \tag{2.6}$$

where α accounts for the ionization losses and β describes the energy loss by the three radiative processes. The first term is almost constant with the energy while the second term grows linearly. Figure 2.6 shows the dependence of the energy loss due to each interaction: ionization is the dominant process at low energies (1 TeV) and pair production governs the muon energy loss at energies above ~ 1 TeV. It should be noted that the stochastic nature of the radiative losses makes muon energy reconstruction a very difficult task putting an unavoidable limit on the accuracy that can be reached.

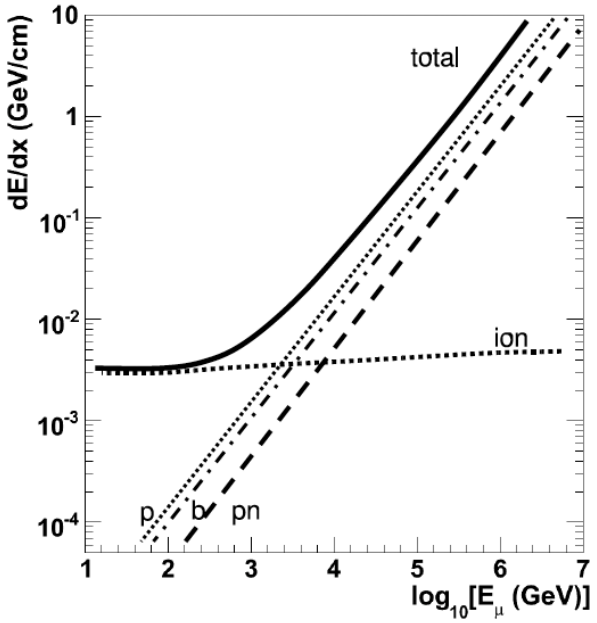

Figure 2.6: Energy losses of a muon passing trough water per unit of distance traveled as a function of the muon energy; "p" refers to pair production; "b" to bremsstrahlung; "pn" to photo-nuclear interactions; "ion" is for ionization.

2.4 The ANTARES experiment

The ANTARES Cherenkov detector [80] is the world's largest underwater neutrino telescope in operation. It consists of a three-dimensional array of 885 light sensors arranged in twelve

flexible lines deployed at a depth of 2450 m in the Mediterranean Sea (Figure 2.7), 42 km off the South coast of France ($42°50'N, 6°10'E$). A schematic view of the apparatus is shown in Figure 2.8. The detector architecture, data acquisition and calibration systems, as well as the environmental properties of the site, are described below.

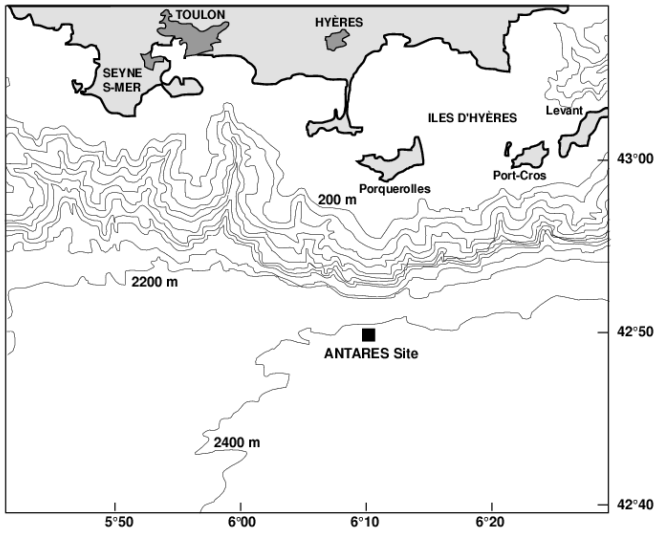

Figure 2.7: Map showing the location of the ANTARES detector site in the Mediterranean Sea, including the French coast are (in grey) and sea depths.

2.4.1 Detector architecture

- **The optical module**

  The optical module (OM) [81] is the basic sensor element of the ANTARES detector (see Figure 2.9). It comprises a 10" photomultiplier tube (PMT) [82] housed in a pressure-resistant glass sphere made up of borosilicate with a diameter of 42.3 cm (17") and 15 mm thick. The PMT is the 14-stage Hamamatsu R7081-20 and was chosen during the R&D phase after an extensive series of test performed on several commercial models. The optical coupling with the sphere is done with a special gel for which 60 cm absorption length and 1.4 refractive index was measured in the laboratory for wavelengths in the blue domain of the light spectrum. The magnetic shielding needed to reduce the influence of the Earth's magnetic fields is achieved with a μ-metal cage surrounding the bulb of the PMT. An internal LED is placed so that it can illuminate the

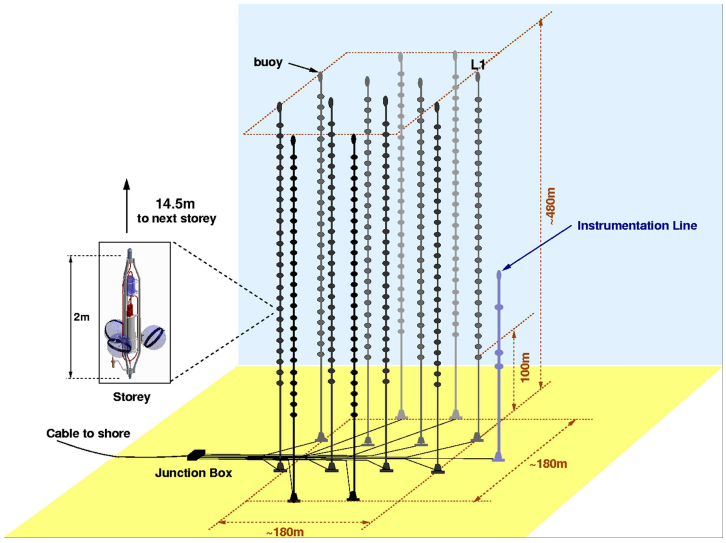

Figure 2.8: Schematic view of the ANTARES detector, which is made up of 885 photo detectors arranged in triplets of storeys along twelve instrumented lines.

PMT photo-cathode with the main purpose of monitoring its transit time. The inner surface of the glass sphere back hemisphere is painted black to absorb induced photons and to reduce the risk of inner reflexions. The linking of the OMs to the electronics container is done through a penetrator, which is a Ti socket with polyurethane over moulding.

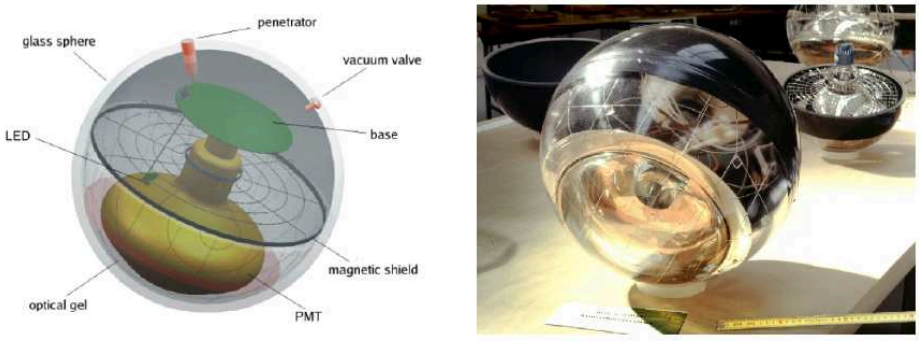

Figure 2.9: Schematic view of an Optical Module showing its different components (left). Picture from an OM at the integration site (right).

- **The storey**

  The storeys are the nodes of the telescope sensor matrix. Each storey is the assembly of a mechanical structure supporting three OMs, which are looking downward at 45° to increase the efficiency of upgoing neutrinos detection, and a titanium container, the Local Control Module (LCM), housing all the electronics boards needed at the storey level. Regular lines are formed by 25 storeys linked with Electro-Mechanical Cable segments (line twelfth is slightly different as it is explained later). The distance between consecutive storeys is 14.5 m being the deepest one located at 100 m above the Seabed. The OMs are symmetrically spaced around the vertical axis and the LCM is placed at the center of the structure. All the electronics commands, the clock signal, the slow control, the HV supply and the readout, arrive at the OMs via the electronics boards housed in the LCM. The main electronics board is the Analogue Ring Sampler (ARS) which digitizes the signals coming from the OMs, providing information about the amplitude, the arrival time and the shape. Additional instruments for calibration purposes can be found in some storeys: receiving Rx hydrophones (5 per line) devised for the acoustic positioning system [83], and a LED Optical Beacon [84] (4 per line) to perform the *in-situ* time calibration. Five storeys are grouped together to form a sector, which is the stand-alone unit concerning the power distribution and the data acquisition system. One out the five storeys in a sector holds a Master Local Control Module (MLCM) which contains additional electronics devices as an Ethernet switch and a multiplexor providing the functionalities needed at the sector level.

- **The line**

  The full detector configuration consists of 12 lines placed following an octagonal shape (Figure 2.11). This layout was chosen to ensure the flat response of the detector in azimuth angles. Each line holds 25 storeys and has about 450 m length. The separation between different lines is of 60 to 75 m.

  The lines are anchored to the Seabed with a dead weight at the Bottom String Socket (BSS) and vertically sustained by means of a buoy on the top end. Every line is instrumented with a String Control Module (SCM) at the BSS anchor housing the electronics required to control the traffic of data from the MLCMs. There is an additional Instru-

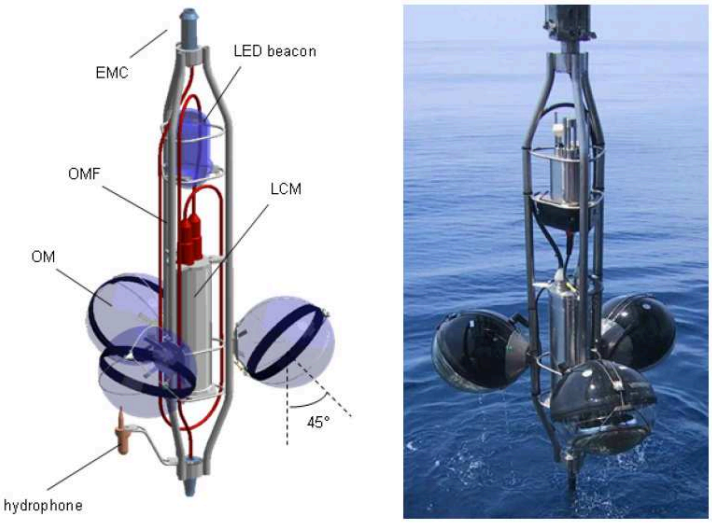

Figure 2.10: Scheme of a storey: the structure holds three OMs, the electronics LCM and (in some cases) the Optical Beacons used for timing calibration or the hydrophones for detector positioning (left). Picture of a storey taken during its deployment (right).

mentation Line (IL) which is equipped with different sensors to measure oceanographic properties.

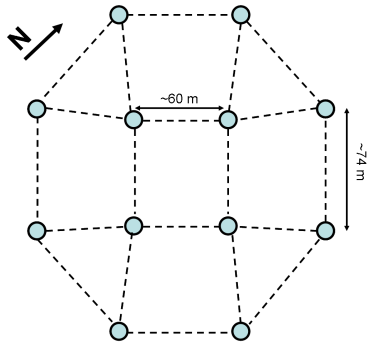

Figure 2.11: The ANTARES detector layout. The position of each line is indicated with a circle.

- **The Junction Box and the electro-optical cable**

  All the lines are connected from their own SCM and via electro-optical interlink cables

to the Junction Box (JB)[1] which provides the power and control signals, receives data from every line and links the detector with the shore station by means of the main electro-optical cable (MEOC) of 42 km length. The electronics components inside the JB are housed in an egg-shaped titanium vessel (Figure 2.12) installed in a parallelepiped frame equipped with two front panels with the connectors for the lines. The MEOC is composed of 48 mono-mode pure silica optical fibers and has a diameter of 58 mm. All the required connections have been performed using a submarine vehicle.

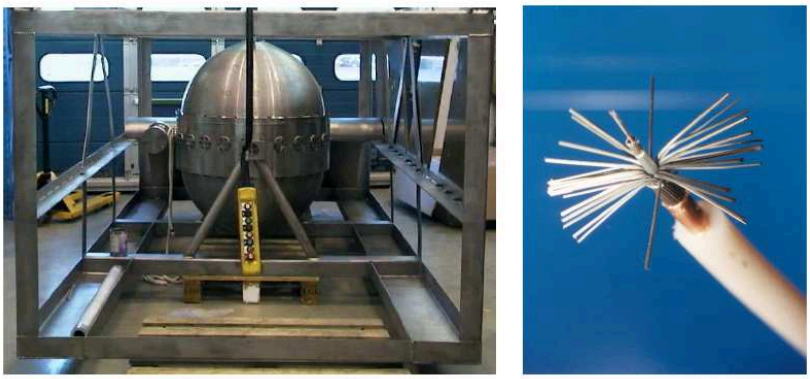

Figure 2.12: Pictures of the junction box vessel with its frame (left) and of the main electro-optical cable (right).

2.4.2 The Data Acquisition system

The Data Acquisition (DAQ) system [85] comprises the different aspects of the signal digitization, transport, filtering and storage, which are discussed in detail below.

- **Signal digitization**

  A photon arriving to the PMT photo-cathode can induce an electric signal on the anode of the PMT with a probability to occur determined by the PMT quantum efficiency. In order to avoid possible losses in the transmission of the signals registered by the PMTs to the (40 km off) shore station, those signals exceeding the so-called L0 threshold condition (typically set to 0.3 p.e) are digitized by the custom front-end electronics

[1] The JB has 16 electro-optical sockets to plug the cables but, in order to compensate for failures experienced in some of the 16 outputs, two separate lines are connected with one single socket by means of special cables which are denoted as "Y" links because their particular shape.

chip. In ANTARES the digitization is done by an ASIC chip, the Analogue Ring Sampler or ARS (see Figure 2.13), which has been specifically designed to match the detector requirements [86]. Their main functionalities are:

- It can discriminate between two modes, single-photoelectron (SPE) signals (i.e., signals which have a shape and an amplitude compatible with those of a single photoelectron) and complex (waveform-WF) signals.
- It can measure the charge and the arrival time of the event and, for WF type events, it can sample the signal at high speed and digitize it.

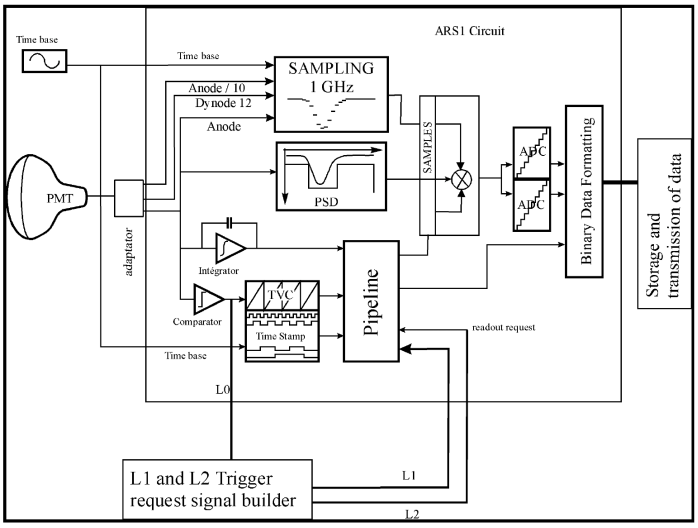

Figure 2.13: The ARS front-end electronics chip architecture.

An Analogue-to-Voltage Converter (AVC) is used to integrate all the signals within a time window of 35 ns chosen to limit the contribution from electronics noise. A local clock on the ARS board provides the reference time respect to which those hits crossing the threshold are time-stamped. A Time-to-Voltage Converter (TVC) provides time information as binary data (8 bits) allowing for measurements of the hit times within the 50 ns interval between two subsequent clock pulses: each clock cycle is subdivided in 256 bits so accuracies of $\sim$200 ps can be achieved.

There are six ARSs inside each LCM so every PMT is associated with two ARSs working in a token ring configuration to minimize the electronics dead time. The combined time and charge information of a digitized PMT signal is called a *hit*, and amounts to 6 bits. The read-out of the 6 ARSs in a LCM is performed by a Field Programmable Gate Array (FPGA) which arranges the hits produced in a certain time window into data-frames and buffers these data-frames in a 64 MB Synchronous Dynamic Random Access Memory (SDRAM). The length of the this time window ('timeslice') is set to a value ($\sim$ 104 ms) much larger than the time it takes for a muon to traverse the complete detector.

- **Data transfer and storage**

  In ANTARES all signals passing the L0 condition are sent to shore following the so-called *all-data-to-shore* strategy. The transmission process starts at the sector level, where the MLCM merges all the data incoming (via a bidirectional 100 Mb/s Ethernet link) from the 5 LCMs into a 1Gb/s link by means of an Ethernet switch. The data collected by the MLCMs in a line is then routed to the SCM at the anchor. Afterwards, the information gathered from all the SCMs goes to the JB and from there is sent to the control room on shore through the Main Electro-Optical cable. This is made using a Dense Wavelength Division Multiplexing (DWDM) which allows the transmission of different streams of data along a single fiber using different wavelengths. Figure 2.14 depicts the complete process.

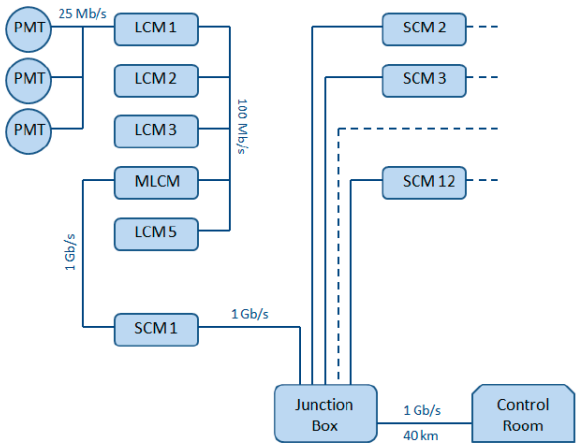

Figure 2.14: Schematic overview of the data transfer in ANTARES.

- **Data filtering and trigger**

  As mentioned no further filtering of the PMTs signals is done offshore except for the L0 threshold selection. Since the vast majority of the signals recorded are due to the optical background, a computer farm on shore is used to reduce the amount of data to be stored. This is done by applying a data filter algorithm based on different trigger criteria. Basically, the data filter software looks for space-time correlated hits consistent with a specific physics signal. Once filtered, data is formatted using the ROOT package [87]. At present, several trigger algorithms are used. A general purpose muon trigger ('standard') makes use of the causality relation

$$|t_i - t_j| <= r_{ij} \times \frac{n}{c}, \tag{2.7}$$

  where t_i (t_j) refers to the time of the hit *i* (*j*), r_{ij} to the distance between PMTs *i* and *j*, *c* is the velocity of light in water and *n* the index of refraction on the sea water. This trigger can operate with hit rates in each PMT up to ∼250 Hz. In order to limit the rate of accidental correlations the hits are preselected requiring either coincidence signals of two L0 hits collected in the same storey and in a time window of 20 ns, or signals exceeding a predefined High-Threshold condition (set to 3 p.e. or 10 p.e. depending on the data taking conditions). This preselection criterion defines the so-called L1 hits. Dedicated triggers are used for multi-messenger analysis and one minimum bias trigger for data quality monitoring. In addition, there are muon triggers based on local coincidences and also a directional trigger:

  - The T3 trigger algorithm searches for clusters of L1 hits on adjacent storeys or next-to-adjacent storeys and inside a particular time window. This time window is of 80 ns when the L1 hits are collected in two consecutive storeys and of 160 ns when the L1 hits are detected in two storeys separated by one storey. Under normal conditions, the T3 rate is 20 Hz.
  - The 3N requires at least 5 L1 hits in a time window compatible with a muon track. The typical rate of the 3N trigger is 10 Hz.

- The GC trigger, which is used to maximize the efficiency to detect neutrinos coming from the Galactic Center, demands one L1 and 4 L0 in the direction of the Galactic Center.
- The K40 needs two L0 in two optical modules in the same storey and within a time window of 50 ns.
- A special trigger referred to as TST is used to correlate events with alert signal sent by optical and gamma-ray telescopes.

2.4.3 Detector calibration

A good calibration of the detector is crucial in order to guarantee its optimal performance. In particular, a precise knowledge of the position and arrival time of the hits to the PMTs is needed for an accurate track reconstruction, as well as the measurement of the deposited charge to estimate the muon energy.

- **Time calibration**

  Several calibration systems and methods are used in ANTARES [88]. These are briefly summarized here and are described with detail in the next chapter.

  1. A 20 MHz master clock generator on shore and synchronized with the GPS is used to provide a common reference to all the detector elements. This system enables to measure the time delays due to the electronics paths and the absolute time-stamping of the detected events.
  2. At the integration sites, prior to the deployment of the lines, a special setup consisting of a laser sending light to the PMTs through an optical fiber is used to obtain the first calibration parameters by measuring the relative time offsets between the OMs.
  3. Time calibration is performed *in-situ* with a set of LED and laser-pulsed light devices referred to as the Optical Beacon (OB) system. These systems allow to check and correct (if needed) the calibration constants measured on shore.
  4. The results obtained with the OB system are cross-checked using the properties of the ^{40}K isotope, which can decay producing an electron of 1.3 MeV energy capable of inducing a Cherenkov light cone and illuminate a close-by OM.

5. An internal LED placed on the back of the PMT photo-cathode is used to monitor its transit time.

- **Positioning systems**

  Due to the sea currents and the flexible nature of the detector lines, the top storeys can move up to several meters from their nominal position depending on the sea conditions (see Figure 2.15). To allow track reconstruction without degrading the angular resolution, a precision on the OMs relative positions of 20 cm is required. In ANTARES, this is achieved using two independent systems:

  1. A High Frequency Long Baseline acoustic system (HFLBL) consisting of acoustic emitters and receivers along each line.
  2. A set of compasses and tilt-meter sensors in every storey.

  The acoustic system works by measuring the travel times of 40-60 kHz acoustic signals sent by RxTx emitting transducers at the line anchor and received by a set of Rx hydrophones regularly placed along a line (one every five storeys). From these measurements, the positions of the hydrophones are obtained on the basis of the triangulation technique and a least-square minimization procedure (Figure 2.16). The tilt-meter-compass sensors provide the local tilt angles of each storey with respect the horizontal plane (pitch and roll) as well as its orientation with respect the Earth Magnetic North (heading). Using the information gathered from these two systems, the shape of the lines is reconstructed every two minutes by performing a global χ^2 fit based on a model which predicts the mechanical behavior of the line under the influence of the sea current. The relative positions of the OMs are then deduced from the reconstructed line shape and from the known geometry of the storeys.

- **Charge calibration:**

  The charge calibration [89] enables to translate the signal amplitudes into number of photo-electrons (p.e.), which is the relevant information for muon energy reconstruction and the physics analysis. Moreover, the study of the ^{40}K counting rate shows a regular decrease with time which is thought to be caused by the ageing of the PMT photo-cathode. Since all channels are tuned to have an effective threshold of 0.3 p.e.periodic

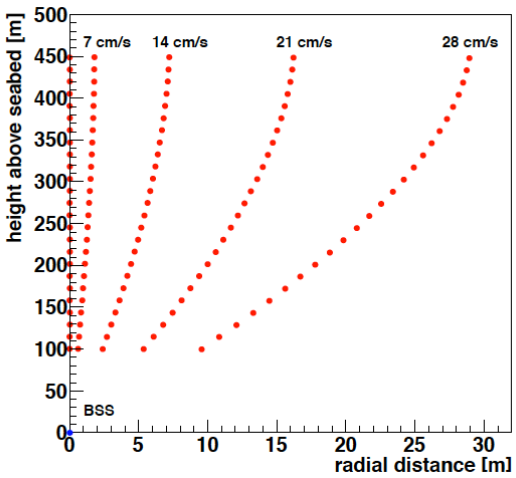

Figure 2.15: Calculated positions (height and radial displacement) of the storeys of a line (red circles) with respect to its anchor for different sea current velocities.

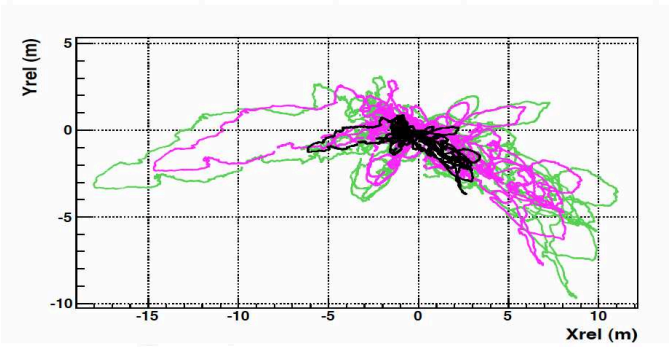

Figure 2.16: Displacements in the horizontal plane of three storeys of line 3 equipped with hydrophones at different heights (black: storey 1 placed about 100 m above the sea bed, pink: storey 14 above 290 m above the sea bed, green: storey 25 at the top of the line).

checks need to be performed and corrections applied when a change of the PMT gain is observed.

Assuming a linear response of the integrator and the ADC, the charge conversion over the full dynamical range of the ADC can be estimated from the known position of the single photo-electron peak and of the pedestal. The pedestal value of the AVC channel is measured using special runs during which the PMT current is digitized at random times. The optical activity from bioluminescent bacteria or from ^{40}K decays produce, on average, single photons at the photo-cathode level. These minimum bias events are used to study the single photo-electron peak.

It has been observed that time measurements in the TVC channel influence the charge measurements performed inside the ARS (the inverse effect does not occur). This "cross talk" effect can be corrected on an event-by-event basis using *in-situ* measurements of the AVC value versus the TVC value. The maximal size of this correction observed amounts to 0.2 photo-electrons. Once the cross-talk correction is made, the charge calibration is applied to reconstruct the amplitude of the individual PMT signals. The distribution for optical activity events is then single photo-electron charges as it is shown in Figure 2.17.

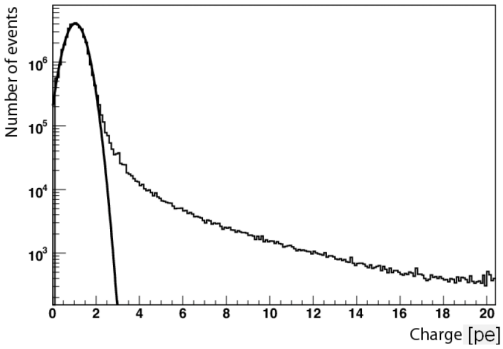

Figure 2.17: Calibrated charge distribution combining all the PMTs in the detector.

2.4.4 Site optical properties

During the R&D phase of the project, a detailed evaluation of the site was carried out to measure some environmental parameters and the optical properties of the deep sea water

location, which have an important impact on the detector performance.

- **Water optical properties**

  The main effects of the medium optical properties on the light propagation are the scattering and the absorption of photons. Both influence the reconstruction capabilities of the telescope. While scattering changes the direction of the Cherenkov photons, absorption reduces the amount of light arriving to the PMTs. These parameters depend on the wavelength and their combination allows to define the attenuation effective length (Equation 2.8) which gives an indication of the fraction of photons emitted by the source that are actually detected:

$$\frac{1}{\lambda_{\rm att}^{\rm eff}} = \frac{1}{\lambda_{\rm abs}} + \frac{1}{\lambda_{\rm scatt}^{\rm eff}}, \tag{2.8}$$

  where $\lambda_{\rm scatt}^{\rm eff}$ is defined as $\lambda_{\rm scatt}/(1- < \cos\theta >)$ being $< \cos\theta >$ the average cosine of the total scattering angular distribution [2].

  Measurements at the ANTARES site (see Figure 2.18) were performed with an autonomous mooring line using a pulsed isotropic light source placed at different distances from a 1" diameter PMT and for two wavelengths (blue and UV). At present, the optical beacon system is used to measure the optical properties of the sea water [90].

  The velocity of light in the sea water is given by the wave packet group velocity

$$v_g = \frac{c}{n_p} - \frac{ck \cdot dn_p}{n_p^2 \cdot d\omega}, \tag{2.9}$$

  where k is the wave number and ω the frequency of the wave packet. This is also a key parameter for muon track reconstruction. Measurements of the group refractive index as a function of the wavelength at the ANTARES site have been done recently using the optical beacons as well [76].

- **Biofouling and sedimentation**

  The detector sensors are exposed to underwater sedimentation and biofouling processes which affect their transparency reducing the efficiency in the light transmission into the PMT. Both phenomena are caused by the presence of microorganisms (mostly

[2] Equation 2.8 holds only when $< \cos\theta > \sim 1$, which is the case for multiple scattering in seawater.

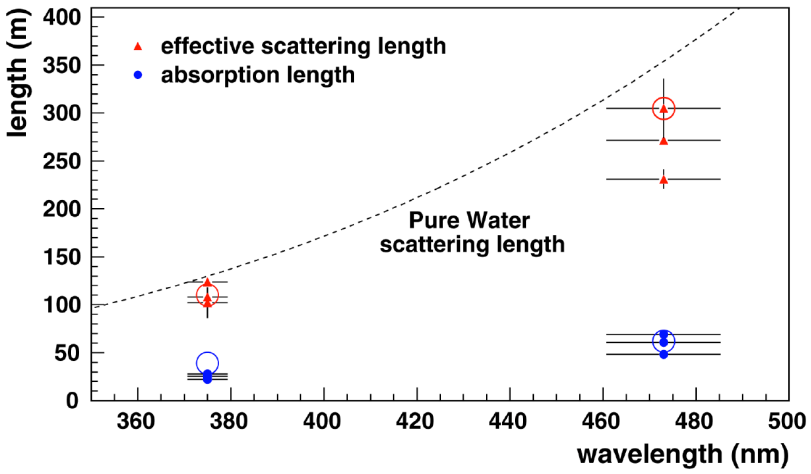

Figure 2.18: Absorption and effective scattering lengths measured at the ANTARES site [91] at various epochs for UV and blue data. Horizontal error bars illustrate the source spectral resolution. The large circles are estimates of the absorption and scattering lengths in pure sea water. The dashed curve is the scattering length for pure water, upper limit on the effective scattering length in sea water.

bacteria) in the medium, which can get adhered (biofouling) or gravely accumulate (sedimentation) on the external surface of the OMs, creating a very thin biofilm capable of absorbing part of the incident light. The average loss of light transmission caused by these two processes was measured at the ANTARES site [92] during the R&D phase of the project. The experimental setup consisted in two resistant glass spheres similar to those used for the OMs. One of them was equipped with five photo-detectors glued to the inner surface of the sphere at different inclinations (zenith angles θ) which were illuminated by two blue light LEDs contained in the second sphere. The measurements went on during immersions of several months and extrapolated to longer periods of time. Results showed a decreasing trend of the glass spheres transparency with time (Figure 2.19) which is less pronounced at higher zenith angles of the glass sphere as expected. After 8 months of operation, the loss of transparency in the equatorial region of the OM dropped only $\sim 2.7\%$ and then it seems to saturate. Extrapolations indicate a global loss after 1 year of $\sim 2\%$ (considering the two glass spheres used in the setup). Taking into account that the PMTs of ANTARES point 45° downward (zenith angle of

135°), the biofouling and the sedimentation do not represent a major problem for the experiment.

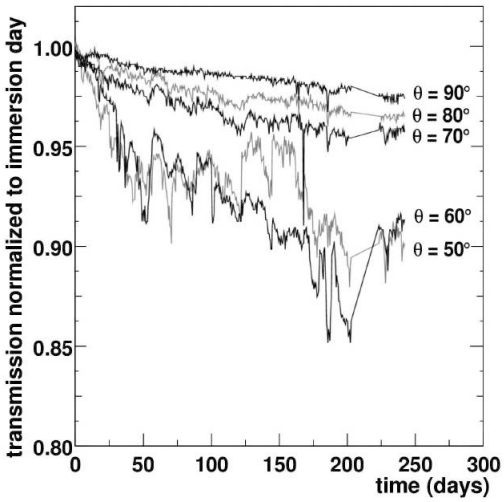

Figure 2.19: Light transmission into the OM as a function of time since the immersion day for five different zenith angles of the photodiodes. The measurements are normalized to unity at immersion day.

- **Optical background**

  At the location of the ANTARES site two natural phenomena producing light constitute an unavoidable environmental background that has to be accounted for. The sources of this optical background are the potassium 40 and the bioluminescent organisms present in the sea water.

  The ^{40}K is a radioactive isotope whose concentration in the sea water depends on the medium salinity. This isotope can decay (Equation 2.10) producing an electron with energy sufficient to exceed the Cherenkov threshold and emit up to 150 Cherenkov photons. Typically the light pulses due to the ^{40}K decay have low amplitude (∼1 p.e.) and are uncorrelated on time scales of a few nanoseconds.

$$\begin{aligned} {}^{40}\mathrm{K} &\rightarrow {}^{40}\mathrm{Ca} + \mathrm{e}^- + \bar{\nu_\mathrm{e}} \quad \mathrm{B.R} = 89.3\% \\ {}^{40}K + e^- &\rightarrow {}^{40}Ar + \nu_e + \gamma \quad \mathrm{B.R} = 10.7\% \end{aligned} \tag{2.10}$$

Bioluminescence is the production and emission of light by a living organism. This is a form of chemiluminescence induced (at the detector site) by bacteria and the activity of small marine organisms. Therefore, the rate of bioluminescent light detected in ANTARES is expected to be correlated to the amount of luminescent organisms around, and hence to be dependent of the sea current velocity. Bioluminescence and ^{40}K decays give a continuous contribution to the count rate. Measurements with the deployed detector lines have shown that the mean rate value of this baseline is of about 60 kHz.

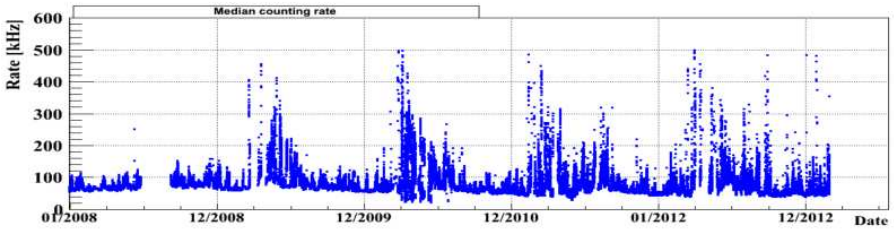

Figure 2.20: Median rates recorded between 2008 and 2013. High bioluminescence rates happen in coincidence with the spring.

Furthermore, there is an additional discontinuous component to the baseline composed by short flashes of light which are thought to be produced by light-emitting multicellular organisms. Bursts of light emission increasing the baseline rate up to several MHz have been observed (Figure 2.20). The fraction of time during which the instantaneous background rate exceeds the baseline rate by at least 20% is referred to as the burst fraction. Studies of this second component of the optical background showed a seasonal dependence. During these periods of high bioluminescence a safety threshold is established and if exceeded, the PMTs of the detector are switched off to avoid a fast ageing. In the meantime the rates are monitored with the IL.

2.4.5 Construction milestones

The ANTARES detector is the first deep-sea neutrino telescope. Its construction started in 2001 with the installation of the long distance electro-optical cable MEOC. Late in 2002 the underwater junction box was installed. For this purpose, the immersed end of the cable was recovered, the junction box connected to it, then tested on the deck of the ship and

finally deployed. During the following years a prototype line (with only 5 storeys) [93] and a mini-instrumentation line [94] were installed and operated in situ, allowing the validation and optimization of the design, as well as the evaluation of possible long-term effects. The first detection line was installed in 2006. Since January 2007, and until the deployment of five new lines during a sea campaign in December 2007, ANTARES was operated with 5 detection lines[3]. The construction of the apparatus ended with the installation of its twelfth line in May 2008. The complete detector collects atmospheric muons at a rate of 5-10 Hz. Each day an average of 3 upgoing neutrinos are reconstructed using two or more lines. Figures 2.21 and 2.22 show, respectively, the number of effective days of data taking per month and the number of neutrinos reconstructed as upgoing per day during year 2009 and 2011. The ANTARES project has proven the feasibility of the installation and operation of a neutrino telescope at high depths in the Mediterranean Sea. In [95] a review of the most relevant physics results published by the ANTARES Collaboration can be found.

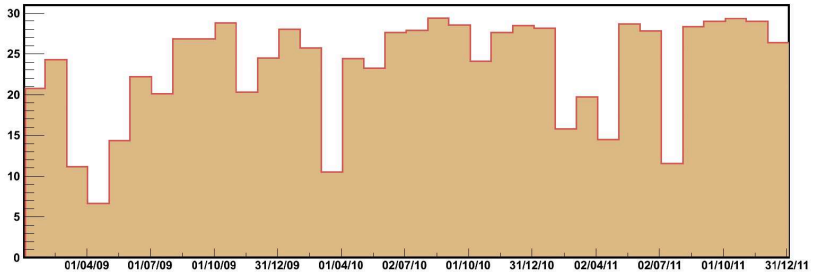

Figure 2.21: Number of effective days of data taking per month during the period 2009-2011.

[3]The first physics analysis presented used data collected from this period.

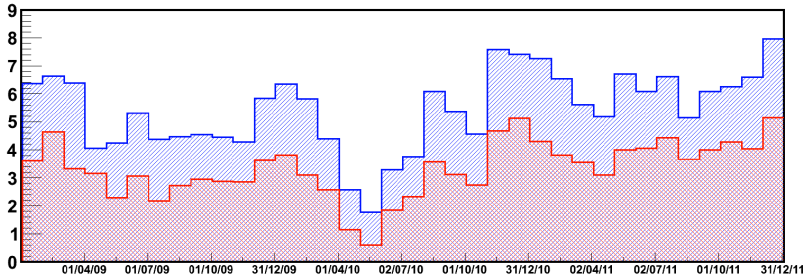

Figure 2.22: One month average number of upgoing neutrinos detected per active day of data taking. In red are shown those events which were reconstructed with multiple lines and in blue the single line events.

3

Event simulation and track reconstruction

The Monte Carlo (MC) simulation of the atmospheric neutrino and atmospheric muon fluxes, as well as the detector response to the generated events which end up reaching it, are discussed in this chapter. The methods used in ANTARES for muon track and energy reconstruction are also described.

3.1 Simulation scheme

Three different stages (Figure 3.1) can be distinguished in the MC simulation chain: 1) the generation of events, 2) the particle propagation and the Cerenkov light emission and 3) the PMT response and digitization. In the first place, the event generators create the primary particles with a given energy and spatial distribution. Then, propagators transport leptons (e.g. muons) through different media (water and rock) accounting for energy losses and the production of secondary particles. The Cherenkov light generated by charged particles is then tracked by photon propagators. When the photons reach the OMs, the detector response is simulated.

For convenience the instrumented volume of the detector is treated as a wide cylinder containing all the PMTs. Surrounding this volume there is a larger cylinder referred to as the "can" that defines the volume within which the Cherenkov light is generated, i.e., the limit between simple muon propagation and propagation plus Cherenkov light generation (Figure

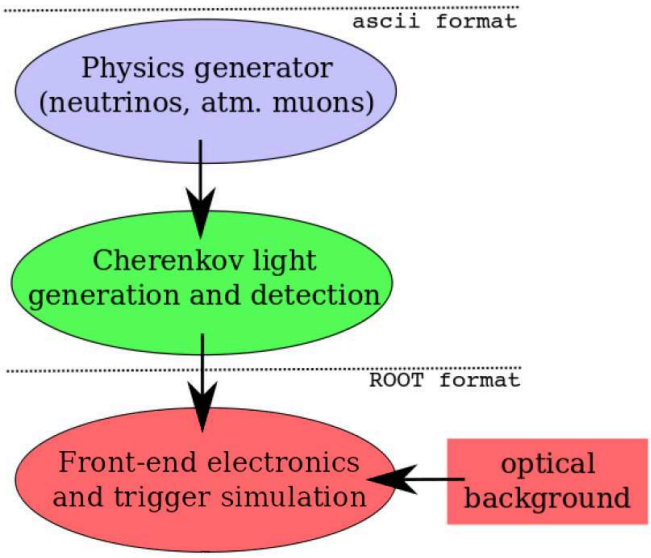

Figure 3.1: Monte Carlo simulation chain scheme.

3.2). It should be noted that the can is purely a useful artifact that allows to distinguish between particles that can produce a signal in the detector and for which it is necessary to calculate the detector response (volume events), from those that interact outside the can and only produce muons crossing the can surface (surface events).

The can has to be sufficiently large to contain the volume within the vast majority of the Cherenkov light detected by the experiment is generated. Typically it extends three attenuation lengths beyond the instrumented volume. The emission of Cherenkov light needs to be simulated only when the particles are close to the detector. Outside the can only energy losses are considered in the particle propagation.

3.2 Event generation

Two different physical events can produce Cherenkov light detectable at the ANTARES site:

- Single muons and muon bundles (two or more muons coming from the same air shower) produced in cosmic ray interactions in the atmosphere.
- Muons produced in neutrino interactions near the detector volume.

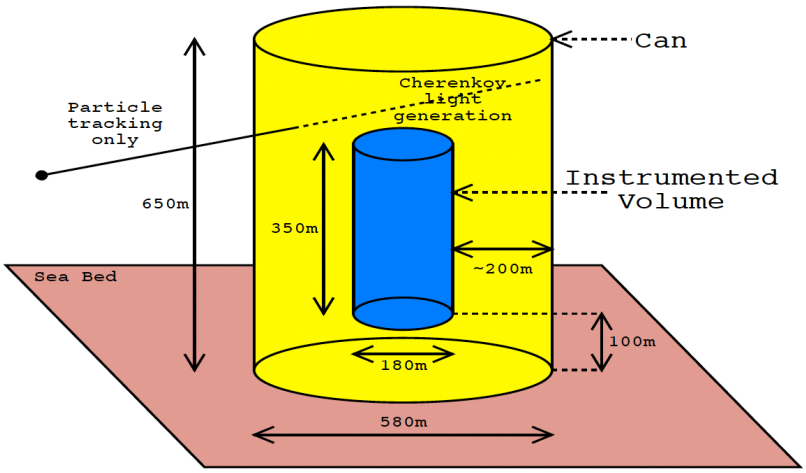

Figure 3.2: Definition of the detector geometry for the event generation.

Description of the methods and software packages used to simulate their signals is given below.

3.2.1 Atmospheric muon generation

Atmospheric muons are the remains of hadronic showers produced in the interaction of cosmic rays several kilometers high in the atmosphere. Even though the OMs in ANTARES are facing downwards many of these muons produce detectable light. They are the most abundant events observed by a neutrino telescope and, therefore, they constitute the primary source of physical background. The vast majority of these events can be rejected by selecting only upgoing tracks in the physics analysis. The remaining background of atmospheric muons stems from downgoing events which are mis-reconstructed as upgoing. Particularly dangerous in this respect are bundles of muons.

In ANTARES, the packages CORSIKA [96] and HEMAS [97] allow to produce muons from hadronic showers and track them up to the sea surface. Afterwards, MUSIC[1] [98] propagates them down to the can surface using accurate measurements of the cross sections for the interaction of muons with matter. This software allows for a full muon Monte Carlo simulation that, starting from the generation of atmospheric showers, can accurately reproduce the main features of the muons reaching an underwater/ice neutrino telescope.

[1] MUon SImulation Code

The main drawback of full simulations is the large amount of CPU time they require. Parameterizations of the muon flux can be used to reduce the resources needed. Following this approach, the MUPAGE code [78] was developed to provide a fast Monte Carlo generator of atmospheric muon bundles. The program uses parametric formulas derived from complete Monte Carlo simulations of primary cosmic ray interactions and shower propagation in the atmosphere to generate muons in bundles and propagate them down to 5 km w.e. (water equivalent) depth. The energy of the generated events depends on the vertical depth, on the zenith angle, on the muon bundle multiplicity and on its distance with respect to the shower axis. The multiplicity of the muons in the bundle, the muon lateral distribution and energy spectrum are simulated according to a specific model of primary cosmic ray flux, with constraints from measurements of the muon flux by underground experiments.

The muons are assumed to be parallel to the shower axis and to reach at the same time a plane perpendicular to the shower axis; muon bundles at $\sim$ 2 km water equivalent depth can contain a thousand of muons which can be hundreds of meters far away from the axis shower. The MUPAGE simulation range of validity extends from 1.5 km to 5.0 km of w.e. vertical depth and from 0° up to 85° for the zenith angle. The livetime corresponding to the number of generated events is also calculated. The output contains all the kinematics of the muon on the can surface.

To optimize the simulation, the code was restricted to follow only secondary particles with energies E $>$ 500 GeV. Those muons are then propagated through water using MUSIC. Muons traveling several absorption lengths far from the detector have a small probability to give a signal on photo-multipliers. The so-called *prompt muons* (originated from the decay of charmed mesons and other short-lived particles), which are expected to give a non negligible (but small) contribution for muon energies as high as $\sim$10 TeV or $\sim 10^3$ TeV depending on the charm production model, are not included.

3.2.2 Atmospheric neutrino generation

The generation of atmospheric neutrinos is performed in ANTARES with the GENHEN package [99]. This software allows to simulate neutrino interactions and to propagate the resulting muons to the can. The goal is to produce distributions of the particles created in these interactions, both on the can surface and inside it. GENHEN is suitable for the full range of studies

performed in ANTARES, from neutrino oscillations to high energy astrophysics analysis.

The simulation process goes as follows (see Figure 3.2). A large number of neutrino interactions $\mathcal{O}(\sim 10^{10})$ is generated in a restricted volume surrounding the detector. This generation volume must be large enough to ensure that all interactions that could give place to a muon inside the detector are generated: the size is determined from the maximal muon range that is associated with the highest neutrino energy that is generated (typically $E_{\max} = 10^8$ GeV).

All three neutrino flavors and both neutral and charged current interactions are supported in GENHEN. The LEPTO code allows to integrate the corresponding neutrino interaction[2] differential cross sections over a specified range of kinematic variables by using the CTEQ6-D parton distribution functions (Figure 2.1). The code is very accurate up to lepton energies of 10 TeV. For higher energies extrapolations are done.

The high energy muons produced outside the can must be tracked until they are stopped or reach the surface of the can. Cuts are made on the muon energy and direction in order to avoid full simulation of events with a negligible probability of producing a muon in the can. For events inside the can, the production of the hadronic shower at the interaction vertex must be simulated as charged secondary particles can contribute to the total amount of Cherenkov light emitted.

The effect of the different media (rock and water) around the detector is taken into account in both the neutrino interaction and muon propagation. The probability for a neutrino to be absorbed along its path is determined by the particle interaction cross-section ($\sigma(E_\nu)$) and the density of matter (Figure 3.3) through the Earth ($\rho(\theta)$), and is given by

$$P_{\mathrm{Earth}}(E_\nu, \theta_\nu) = e^{-N_A \sigma(E_\nu) \rho(\theta)}, \tag{3.1}$$

where N_A is the Avogadro number. This probability must be taken into account in the calculation of the expected event rate. Figure 3.4 shows how the absorption starts to be significant for events close to the vertical at energies of 10 TeV. Above 1 PeV only neutrinos close to the horizontal remain unattenuated.

[2] Being the dominant process the charged current deep inelastic scattering (DIS).

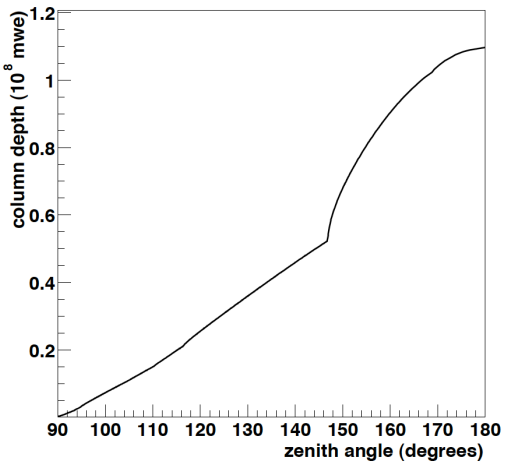

Figure 3.3: Density of the Earth as a function of the neutrino direction expressed in w.e. meters. The kink observed is caused by the density discontinuity associated with the boundary of the Earth's core.

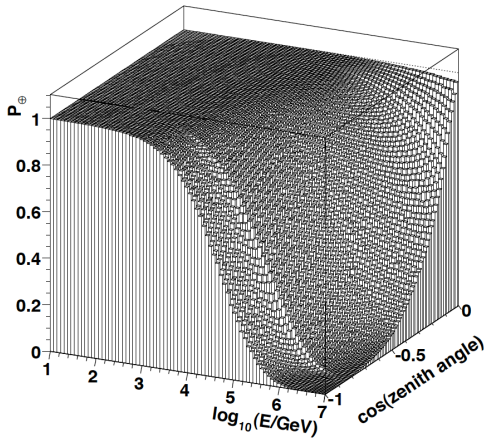

Figure 3.4: Probability of a neutrino to transverse the Earth without undergoing an interaction as a function of the neutrino energy and direction.

3.2.3 Atmospheric neutrino fluxes and weights

Neutrinos are generated following a power law $E^{-\gamma}$ energy spectrum. A generation weight $W_{\rm gen}$ is defined to easily calculate neutrino fluxes in accordance with specific models:

$$W_{\rm gen} = V_{\rm gen}\ t_{\rm gen}\ I_\theta\ I_E\ E^\gamma\ \sigma(E_\nu)\ \rho N_A\ P_{Earth}(E_\nu, \theta_\nu), \tag{3.2}$$

where:

- $V_{\rm gen}$ is the total generation volume (m^3),
- $I_\theta = 2\pi \times (cos(\theta)_{max} - cos(\theta)_{min})$ is the angular phase space factor, which depends on the specified range of neutrino zenith angle ($cos(\theta)_\nu$),
- I_E is the energy phase space factor depending on the input spectral index (γ) for the neutrino interaction rate (this is the integral of the generation spectrum between the minimum and maximum energies),
- $N_{\rm total}$ is the total number of generated events, another simulation input which can be specified by the user,
- $t_{\rm gen}$ is the time represented by the simulation, an arbitrary term that appears in the flux calculation and is usually given in number of seconds in a year.

Then, to calculate the equivalent flux for any particular neutrino model $\phi^{model}(E_\nu, \theta_\nu)$ all the events have to be re-weighted in each interval or bin of energy and zenith angle:

$$\phi^{\rm model}(E_\nu, \theta_\nu) \cdot W_{\rm gen}^{-1} = \frac{dN_\nu^{\rm model}}{dE_\nu dS dt} \cdot W_{\rm gen}^{-1} \tag{3.3}$$

In ANTARES neutrinos and anti-neutrinos[3] are simulated separately with a generation spectral index $\gamma = 1.4$ (in order to increase the statistics at high energies), over a 4π solid angle and within the energy range $10^2 - 10^8$ GeV.

There are different estimations of the atmospheric neutrino flux which depend on measurements of the primary cosmic ray spectrum (flux) and on different interaction models in the atmosphere. These calculations usually rely on extrapolations of hadronic interaction models to high energies. The Bartol model [100] is used in the majority of the ANTARES physics

[3] It is assumed that the two fluxes are equal.

analysis, with the extension up to ∼100 TeV energies taken from tables in [79]. A 30% uncertainty on the high energy neutrino flux [101] is estimated based on the uncertainties in the input parameters. For the atmospheric muon flux a 50% uncertainty is considered [102].

3.3 Cherenkov light emission and propagation

All long-lived particles stored in the output of the physics generators are tracked through the water into the volume of the can using the GEASIM [103] and the KM3 [104] programs, both based in the GEANT software package [105]. The production of the Cherenkov light is simulated for the muon itself and the secondary particles. The influence of absorption and scattering of light is taken into account by a model that has been tuned to data acquired during measurements in the ANTARES site.

GEASIM is used to track all particles but muons. The arrival time of the Cherenkov light into the OMs is calculated analytically for photons inside a wavelength window of 300-600 ns. At each tracking step the Cherenkov cone produced by the relativistic charged particles is calculated and, for all OMs inside it, the hit probability is determined and converted into a photo-electron number using Poisson statistics. To evaluate this probability the wavelength dependent absorption length, the quantum efficiency and the transmission coefficients of the OM glass sphere and gel are used. The relative orientation of the PMT with respect to the Cherenkov front and its angular acceptance are also taken into account. The arrival time of photons is calculated based in the group velocity of the light front and includes smearing factors from the TTS (transit time spread) of the PMT as well as from the wavelength dispersion, where the latter depends on the distance between the track segment and the OM. The main drawback of GEASIM is that the scattering of the Cherenkov photons is not considered, while this is an important effect to account for in order to obtain a realistic estimate of the angular resolution of the detector.

The KM3 software package[4] allows to simulate the response of the ANTARES detector to the passage of high energy muons including the effect of the photon scattering in the sea water.

A full simulation where every Cherenkov photon is generated and propagated individually is not possible due to the very large number of photons produced by a single muon and the

[4] It uses a modified version of the MUSIC code to propagate the muons through the detector.

need for high statistics, especially in the study of the atmospheric muon background. Therefore, an alternative simulation of photon scattering is needed. In KM3 this is achieved by building photon tables which store the distributions of the number and arrival time of PMT hits at different distances, positions and orientations with respect to a given muon track or electromagnetic shower. The procedure is the following: track pieces of 1 m length are sent to GEANT within a large water volume. Energy loss, multiple scattering and radiative processes below a given energy threshold (typically 0.1-1 GeV) are enabled. Individual Cherenkov photons are created and tracked in the water. A diffusion and absorption model has been implemented which allows to track each photon through various scattering processes until it gets absorbed or leaves the volume. Each time a photon penetrates one of several concentric spheres around the muon track origin, its position, direction and time are stored (Figure 3.5). This photon field is then convoluted with different orientations of the OMs with respect to the sphere radius.

Muons from physics event generators are tracked in the can volume using MUSIC. After each tracking step the hit probabilities for all OMs are evaluated using the scattering tables. No Cherenkov photon tracking is necessary at this step. High energetic radiative processes like bremsstrahlung are also treated with MUSIC and their Cherenkov photon yield is given by the electromagnetic shower table. One set of scattering tables can be reused as long as the underlying scattering and absorption model does not have to be changed.

3.4 Detector simulation

The detector response is simulated using the TriggerEfficiency program [106]. This software is in charge of the addition of the optical background to the hits generated by physical events, the simulation of the electronics and the triggering of events, i.e., it makes the output of the generators plus propagators look like hits from the DAQ.

The amount of background light added (according to a Poisson distribution) to the PMTs corresponds to a counting rate taken from a real detector situation, so it takes into account the background due to the radioactive decay of the ^{40}K but also the contribution from bioluminiscence in the sea water and temporary problems related to the electronics.

The front-end ARS chip integrates the analogue signal from the PMT over a time window of 25 ns. This is simulated by summing up the number of photons detected in that window.

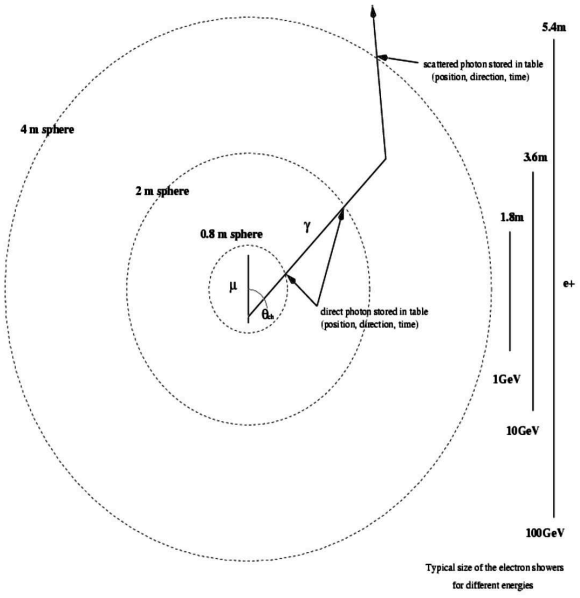

Figure 3.5: Scheme followed in the creation of the Cherenkov photons scattering tables.

The time resolution for single electronic signals is of 1.3 ns (decreasing for higher amplitudes). To account for this effect the hit times are smeared using a Gaussian function with width

$$\sigma = \frac{1.3}{\sqrt{N_\gamma}}\text{ns}, \tag{3.4}$$

where N_γ is the number of photons detected simultaneously. The events are triggered using the same algorithm as for real data. The amplitude measurement (required by the L0 trigger condition) is simulated by smearing the integrated number of photons with an empirical function.

3.5 Muon track reconstruction

Track reconstruction algorithms use the time and position information of the hits detected by the PMTs to estimate the trajectory of a muon crossing the detector. This trajectory can be described by the direction and position of the lepton at some fixed arbitrary time $(\overrightarrow{r_0}, \overrightarrow{p}, t_o)$. The muon direction can be parameterized in terms of the zenith and azimuth angles and, thus, only five independent parameters need to be estimated by the reconstruction methods. The accuracy achieved in the reconstruction of the muon direction determines the pointing

accuracy of the detector and is a crucial parameter in the search for point sources of cosmic neutrinos.

In ANTARES two reconstruction algorithms are used referred to as the offline (`aafit`) and the online (`bbfit`) methods. Both codes exploit, in the fitting procedure, the time difference between the observed hit time t_i and the expected arrival time of photon t_i^{th}, which defines the hit time residual $r = t_i^{th} - t_i$ that is calculated for a given set of track parameters.

3.5.1 Online reconstruction method

The online algorithm [107] is a robust reconstruction method that allows for a quick fit of the track parameters producing reliable results without requiring a precise positioning calibration. It is used in the online display (see Figure 3.6) showing reconstructed events in real time.

The strategy followed by the online method is based on the fact that both a detector line and a muon track can be considered as straight lines in the space. The geometry of the OMs triplet is ignored and the storeys are treated as space points. In both the hit selection and in the fitting procedure `bbfit` makes use of the so-called points of closest approach that (placed on the muon track) are defined with respect to the detector line so most of the Cherenkov light detected is emitted from the vicinity of these points.

All the hits detected within a time window of 20 ns are merged, and only one hit per storey is allowed. The scattered photons and those produced in electromagnetic and hadronic showers are also ignored in the fit. For the selected hits a χ^2 function is defined and minimized. Its value defines the quality of the track reconstruction.

Additionally and in contrast to a particle track, a 'bright-point' is defined as a point-like light source which emits a single light flash at a given moment. The light emission is assumed to be isotropic and the bright-point is defined by four parameters: three for its position and one for its time. The model of a bright-point helps to recognize light from hadronic and electromagnetic showers, for which the actual extension of the shower is typically smaller than the detector line distances.

3.5.2 Offline reconstruction method

The real detector geometry and parameterizations of the hit time distributions (derived from simulations) are used by the offline algorithm [108] to produce high accuracy results in the

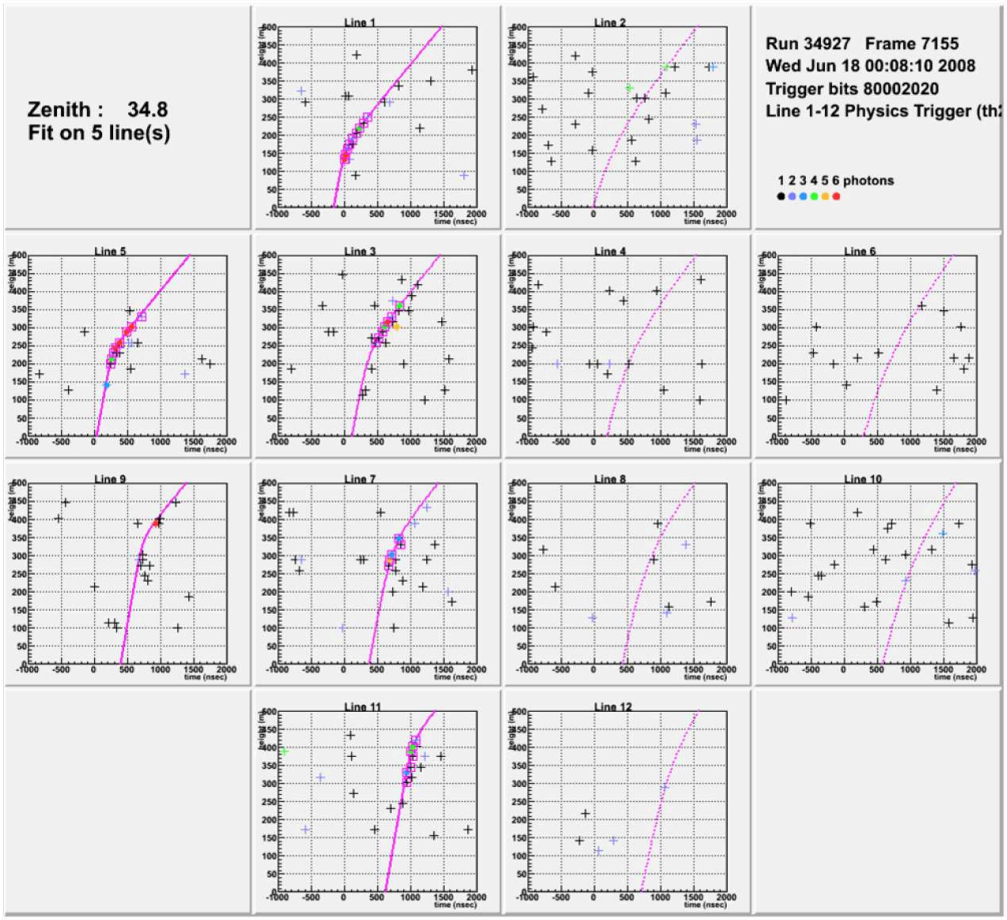

Figure 3.6: Caption of the online display showing a neutrino candidate giving light in all the detector lines. Each panel shows, for each detector line, the vertical position (y-axis) and the arrival time of the hits (x-axis). Crosses are hits in a time window of 3 microseconds around the trigger; full circles are hits passing the trigger condition; open boxes are hits used in the final fit which is represented by the pink lines.

estimation of the muon track direction. This method is used in the majority of the ANTARES physics analysis because it offers an optimal angular resolution and a better detection efficiency at higher energies.

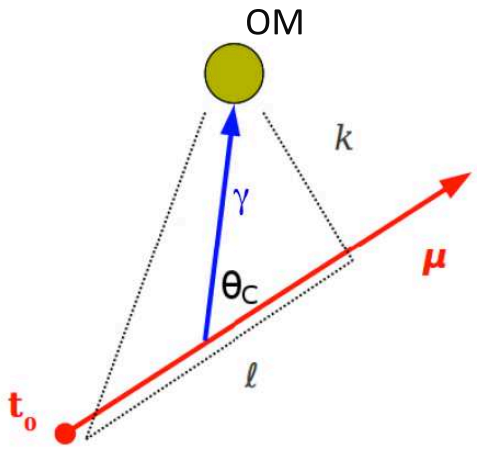

Figure 3.7: Geometry of the detection of a Cherenkov photon. The muon passing through the detector (read arrow) induces Cherenkov light emission at an angle θ_C with respect its trajectory. A photon (blue line) traveling at speed *v* is detected by an OM with *k* distance of closest approach to the muon track.

The algorithm consists of several and consecutive fitting procedures of increasing sophistication and inclusive hit selections. The last step produces the most precise results but requires prior estimates of the muon track parameters that should be close to the true values. The purpose of the first stages of the chain is then to provide such a starting point. In the final step a maximum likelihood fit is performed, where the likelihood is defined as the probability density for the residuals where the expected hit time is given by[5]

$$t_i^{th} = t_0 + \frac{1}{c}(l - \frac{k}{\tan\theta_c}) + \frac{1}{v_g}(\frac{k}{\sin\theta_c}) \tag{3.5}$$

for a certain set of track parameters. The offline method fit chain is listed below.

- Linear prefit: The first step of the fitting chain consists of a linear fit through the positions of the hits that is performed with the hit time as an independent variable.

[5]See Figure 3.7 for a description of the parameters in the equation.

The advantage in the prefit is that it does not require a starting point to converge. The hit selection used relies on local patterns, coincidences and hits in neighboring floors. This is followed by a clustering algorithm based on the causality criterion.

- M-estimator fit: The hits used for this fit are those for which the linear prefit calculates a distance to the initial fitted track smaller than 100 m and which fall inside a $\pm$ 150 ns time window with respect to the expected hit times using the prior track parameter estimates. The M-estimator works by minimizing the function $g(r) = \sqrt{1 + r^2}$ of the residuals.

- The maximum likelihood fit: In this step a set of track parameters is found to maximize the probability to obtain the observed events. This probability is called the likelihood of the event, which is described by parameterizations (previously derived using simulations) of the probability density function of the hit time residuals

$$\mathcal{L}(\overrightarrow{r}, \overrightarrow{p}) = \prod P(t_i | t_i^{th}, \overrightarrow{r}, \overrightarrow{p}), \tag{3.6}$$

where the sum runs over the number of hits that are selected in the last stage of the algorithm.

The full pdf used for the final likelihood fit (see Figure 3.8) takes into account the contribution from hits arriving late due to Cherenkov emission by secondary particles or light scattering, which causes the long tail at positive values, and the effect of the TTS of the PMT smearing the hit arrival times. The probability of a hit being due to background is also accounted for. The quality of the track fit is quantified by the parameter:

$$\Lambda = \frac{\log(\mathcal{L})}{N_{\mathrm{DOF}}} + 0.1 \times (N_{\mathrm{comp}} - 1), \tag{3.7}$$

which incorporates the maximum value of the likelihood $\mathcal{L}$ and the number of degrees of freedom in the fit $N_{\mathrm{DOF}} = N_{\mathrm{hits}} - 5$, which is equal to the number of hits used minus the number of free parameters. N_{comp} is the number of times the repeated initial steps of the reconstruction converged to the same result and, in general, takes large values for well reconstructed tracks and small ones for badly reconstructed events. The Λ variable

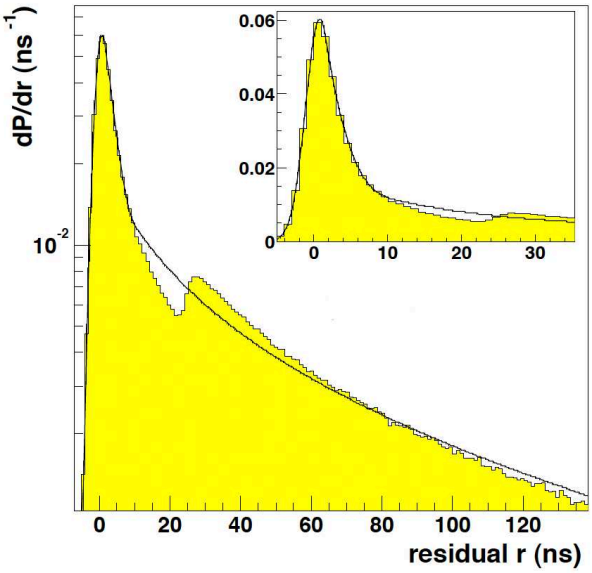

Figure 3.8: The full time residuals pdf used in the reconstruction algorithm last step fit. The filled histograms is derived from MC simulations and the solid line represents the parameterization used in the likelihood.

can be used to reject badly reconstructed events, in particular atmospheric muons that are misreconstructed as upgoing.

The uncertainty on the reconstructed track direction can be used for further event selection. Assuming that the likelihood function near the fitted maximum follows a multivariate Gaussian distribution, the error on the zenith and azimuth angles can be derived from the covariance error matrix. From these errors, the parameter

$$\sigma = \sqrt{\sin^2(\theta_{\rm rec})\sigma_\phi^2 + \sigma_\theta^2}, \tag{3.8}$$

referred to as the angular error estimate, is obtained. As Figure 3.9 shows, cutting on the angular error estimate is highly efficient with signal events while cutting out a large contribution from mis-reconstructed atmospheric muons. On the other side, the large width of the zenith angle pull distribution (Figure 3.10) points out that this estimator does not offer a very precise description of the true error. However, in this work we rely on it to adopt an event-by-event angular resolution search approach for an improved sensitivity to an astrophysical neutrino signal as is discussed in chapter 7.

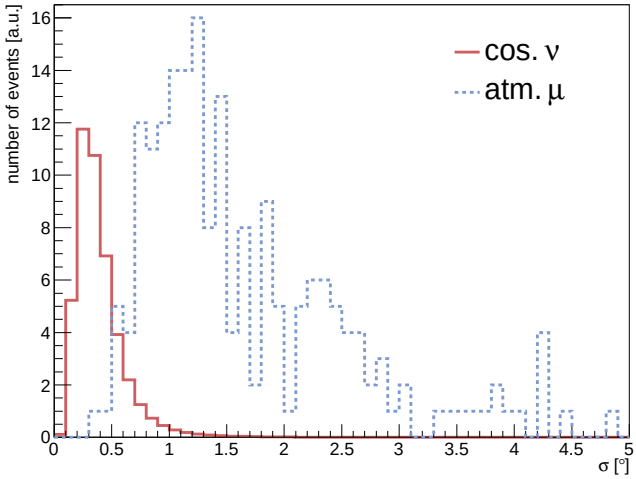

Figure 3.9: Distributions of the angular error estimate for signal neutrinos reconstructed 2 degrees off the true neutrino direction and atmospheric muons are shown. Events are required to be well reconstructed as upgoing.

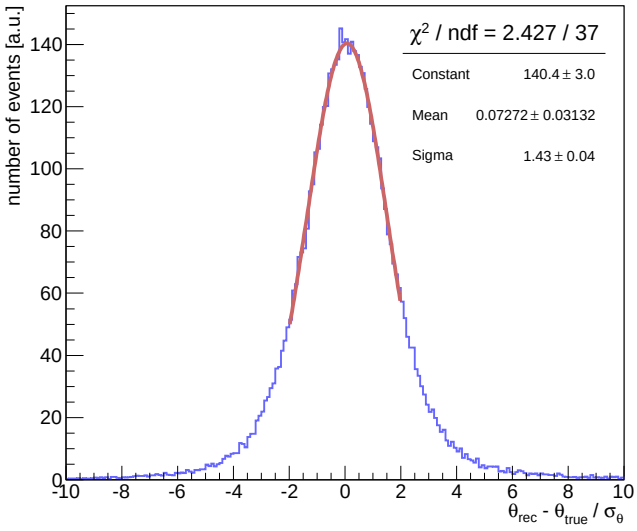

Figure 3.10: Zenith angle pull distribution for upgoing events reconstructed with $\Lambda > -5.2$ and $\sigma < 1.0°$. The width of the Gaussian fit done in the region between -2 and 2 is ∼1.4.

4

Time calibration systems and methods in ANTARES

An accurate time calibration of the detector optical modules is of primary importance in order to achieve an optimal performance of the apparatus. In particular, a good timing resolution is required to ensure the best angular resolution attainable, which in ANTARES is expected to be better than 0.5 degrees at high energies. Therefore, several systems and methods on-shore and in-situ have been developed within the Collaboration in order to perform the time calibration. Their main features are described in this chapter.

4.1 Absolute and relative time calibration

Concerning the detector time calibration it should be distinguished between the absolute and relative time resolutions. The absolute time calibration is important in order to correlate the reconstructed events with transient phenomena like GRBs or supernova explosions. A precision of 1 ms is sufficient for this purpose. The main uncertainty comes from the fluctuations in the path common to all signals, i.e., the 40 km electro-optical cable between the junction box and the on-shore station.

Because track reconstruction methods are based on the pdf of the arrival times of the photons to the PMTs, the relative time differences between individual PMTs have to be precisely corrected to guarantee a good reconstruction of the muon trajectory and, thus, the optimal pointing accuracy of the ANTARES neutrino telescope. The different uncertainties

contributing to the spread of the photon arrival times (Equation 4.1) come from the transit time spread ($\sigma_{\rm TTS}$) of the PMT, which is of about 1.3 ns, the optical properties of the sea water ($\sigma_{\rm water}$), mainly the light scattering and chromatic dispersion, adding $\sim$ 1.5 ns at a distance of 40 m from the OM, the contribution of the small PMT inside the OB reading the signal emission time ($\sigma_{OB} = 0.8$ ns) and the intrinsic contribution due to the electronics ($\sigma_{\rm elec}$).

$$\sigma^2_{OM} = \frac{\sigma^2_{\rm TTS}}{N_{pe}} + \frac{\sigma^2_{\rm water}}{N_\gamma} + \sigma^2_{\rm OB} + \sigma^2_{\rm elec} \tag{4.1}$$

ANTARES is designed to reach an angular resolution better than 0.5° for neutrino energies exceeding 10 TeV. In order to achieve this goal, all electronics and calibration systems are required to contribute less than 0.5 ns to the overall relative time resolution.

4.2 On-shore calibration: dark room T0 parameters

Prior to the deployment of the detector lines, a complete calibration of the OMs is performed on-shore during the integration test of each detector line. These tests have been performed in two laboratories (CPPM in Marseille and CEA in Saclay) using a high intensity (E $\sim 1\mu$J) Q-switched Nd-YAG laser to send very short (FWHM ~ 0.8 ns) pulses of green light ($\lambda = 532$ nm) through optical fibers to all the PMTs within a line sector [109] following the scheme shown in Figure 4.1. A 1-to-16 optical signal splitter is used to provide a synchronous signal to the 15 OMs involved, which are placed in a dedicated dark room. Each optical fiber is coupled to a Lambertian diffuser which spreads out the laser light over the full area of the corresponding PMT photo-cathode.

The arrival times of the photons are digitized by the two ARS cards associated to each OM. The time reference for the laser light emission is provided by an internal photo-diode. After correcting for differences on the fiber path, the time offset between each OM and the first OM of the first storey (from the bottom) of the line (which is chosen as a reference) are calculated for every ARS. These time offsets define the `ARS_T0` parameters (Equation 4.2) which are stored in the ANTARES database and are used as initial calibration constants for a prompt data analysis after the lines deployment:

$$\mathrm{ARS\_T0}_{ij} = (\mathrm{T}_i - \mathrm{T}_j^{\rm pthd} - \Delta\mathrm{T}_{ij}) - \mathrm{T}_{\rm ref} \tag{4.2}$$

where $\mathrm{ARS\_T0}_{ij}$ represents the offset of the ARS *i* in the sector *j*, T_i is the time read by the ARS, $\mathrm{T}_j^{\mathrm{pthd}}$ is the time given by the laser internal photo-diode, $\Delta\mathrm{T}_{ij}$ includes the clock phase plus the optical fiber path times, and $\mathrm{T}_{\mathrm{ref}}$ is the reference ARS time.

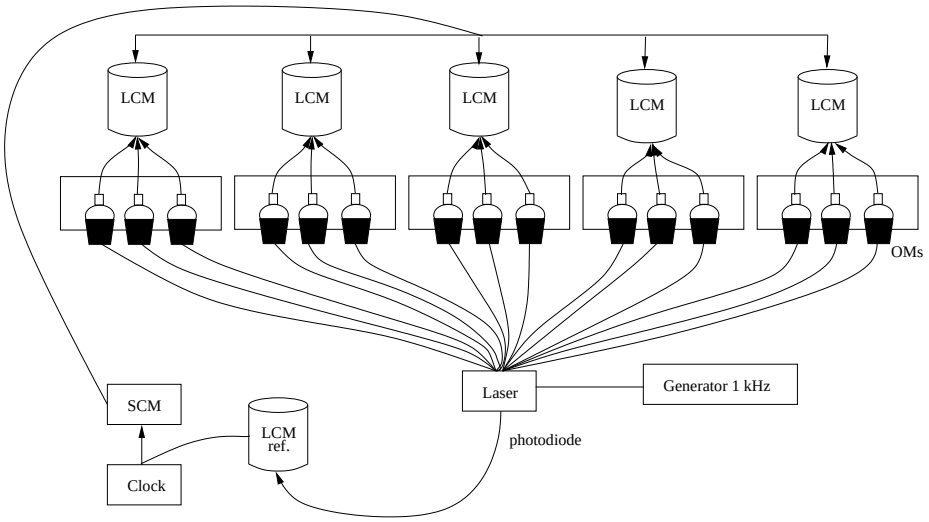

Figure 4.1: Scheme of the setup used during the integration test at laboratory which allows to determine the first calibration parameters.

Figure 4.2 shows the time offsets measured for all ARSs in one sector of a detector line. The spread observed is due to differences in the internal cabling of the OMs to the LCM and to differences in the transit times of the PMTs. During the detector operation these offsets will be monitored and corrected (if needed) by the *in-situ* time calibration systems.

4.3 The echo-based master clock system

The master clock system is used to provide a common synchronization signal to all the electronic modules and to determine the time delays due to the fiber paths from shore to each LCM. This system is also used to broadcast other signals as, for instance, the trigger of the LED Optical Beacon flash (see Section 4.5). The master clock consists of an on-shore based 20 MHz clock signal generator synchronized with the GPS, plus a clock signal distribution system and a set of transceiver boards on each LCM electronics module echoing the signals received back to the shore station (Figure 4.3).

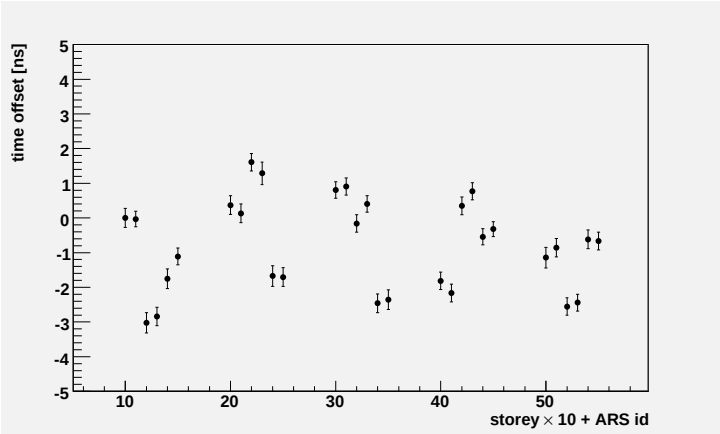

Figure 4.2: Time offsets measured, in the integration laboratory dark room, for all ARSs in one sector of a detector line.

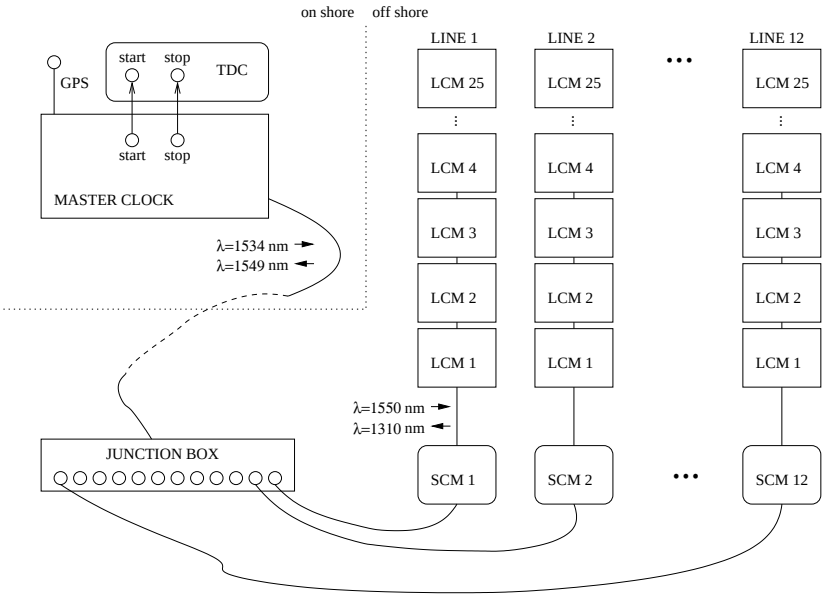

Figure 4.3: Scheme of the echo-based clock system. Signals generated on shore travel through the MEOC and reach the JB splitter which propagates them to each electronics control module.

For the time-stamping of the physics events a reset time-stamp signal (derived from the GPS time) is delivered, from shore and at regular intervals, to the junction box and then to the SCMs and LCMs of each line; the time of the events within a data taking run is obtained by simply counting the number of signal resets. Start and stop clock signals are generated every hour (and in parallel with the physics data taking) to measure, by means of a time to digital converter (TDC), the round trip times between the shore station and the electronics modules. The time delays observed are, therefore, twice the propagation time along the cables to each individual LCM.

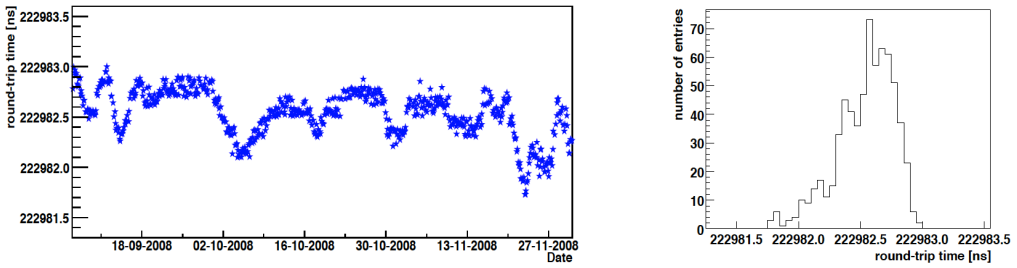

Figure 4.4: Measurements of the round trip time delay between the shore station and the SCM of a line performed during a period of near three months. The projection of the time differences is shown on the right plot. The resolution of the system is of about 200 ps.

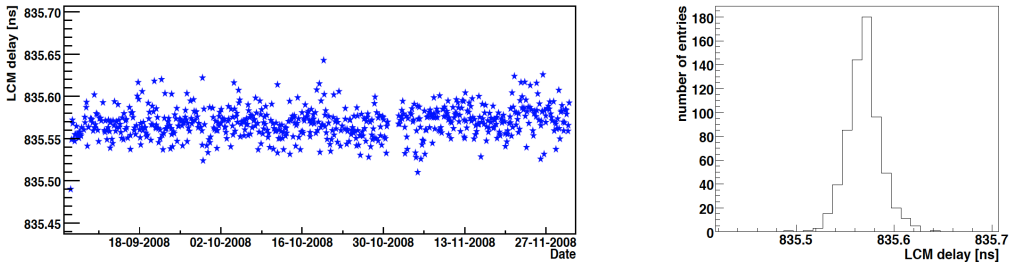

Figure 4.5: Measurements of the round trip times for clock signals sent between the SCM and one of the LCMs performed in a period of near three months. The distribution of the projection of the time delays (right) has a RMS of about 15 ps.

Figure 4.4 shows the round trip times measured between the shore station and one SCM during a period of near three months. The average fluctuation on the observed time delays ($\sim$223 μs) is of $\sim$ 200 ps in one year. This result perfectly matches the requirements concerning the absolute time calibration. All the individual LCM time paths are then referred to

the SCM of the corresponding line. The precision achieved in the measurement of the time delays between the SCM and any of the 25 LCMs in the corresponding line is of the order of 15 ps (see Figure 4.5), well within the requirements concerning the relative time calibration.

4.4 The internal LED

In order to monitor the transit time of the PMTs, every OM has an internal blue ($\lambda = 472$ nm) LED glued to the rear part of the bulb of the PMT in order to illuminate the photocathode. This internal LED emits, pulsed by the clock, light flashes at a rate of about 100 Hz. Monitoring the flashing times obtained from the TVC distributions in each ARS, the internal transit time of each OM can be controlled. Figure 4.6 shows the mean time of the TVC distributions produced when flashing the internal LED of the PMTs within a storey along a period of near one month. The variations observed, from *in-situ* measurements that are performed every week, are less than 0.2 ns (RMS) over an eight month period.

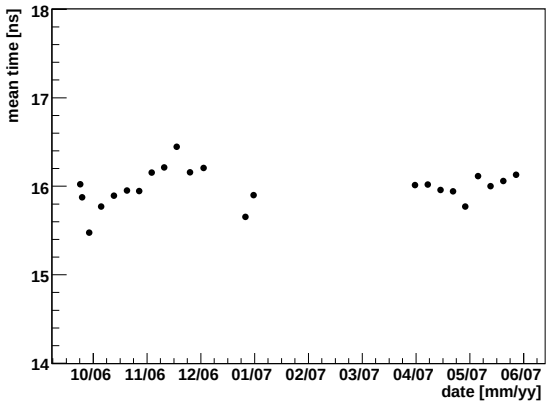

Figure 4.6: Monitoring of the mean time of the TVC distributions obtained when flashing the internal LED inside an OM.

4.5 The Optical Beacon system

The Optical Beacon system consists of a series of LED and laser devices distributed uniformly along the detector which can emit high-intensity light pulses with a well known time of emission. The system was conceived to perform the *in-situ* relative time calibration, but

it can also be used to monitor the optical properties of the sea water [90], as well as to cross-check the positioning system [110].

4.5.1 The LED Optical Beacons

The LED Optical Beacons (LOB) are made up by 36 individual blue LED (472 nm, 35 nm FWHM) light sources arranged in groups of six on electronic boards placed side by side forming an hexagonal prism (Figure 4.7) which is enclosed in a glass container. This container, of the same manufacturer as the OM sphere, has a cylinder shape completed by two hemispheres joined by titanium flanges. Its dimensions are 210 mm for the outer diameter and 443 mm length.

The six LEDs in each board are distributed on each face of the prism as follows; one bulb on top, another LED in the center of the face, and a group of four LEDs surrounding the central bulb. This configuration ensures the light to be emitted isotropically in azimuth. The top LED is used to illuminate the OMs placed above on the same line, while the central LEDs are used to flash the nearby lines.

Each board and sub-group of LEDs can be configured to flash independently triggered by a pulsing circuit based on the Kaputinsky design [111]. At maximum intensity, $\sim 4 \times 10^8$ photons ($\sim$160 pJ) are emitted per flash. The time of the light emission is obtained by means of a pencil PMT (8 mm size) placed in the center of the LOB hexagonal frame. The readout of this internal PMT is done using a specific ARS card. The voltage of the photo-cathode as well as the LEDs light intensity can be controlled and adapted to specific purposes.

There are 4 LED Optical Beacons positioned regularly (in the 2nd, 9th, 15th and 21st storeys from bottom) on each detector line. The non consecutive LOBs pairs inside a line are fired simultaneously at maximum intensity during a nominal calibration run. In total 24 runs of 5 minutes duration are taken once per month for *in-situ* time calibration purposes.

4.5.2 The Laser Optical Beacon

In order to calibrate the lowest storeys of the lines (which can not be illuminated with the LED OBs) and to measure the relative offsets between the detector lines, two Laser Beacons (LB) are placed at the bottom of two central lines, attached to the BSS of lines 7 and 8 (but only the latter could work after deployment). These devices are composed by a Nd-YAG laser

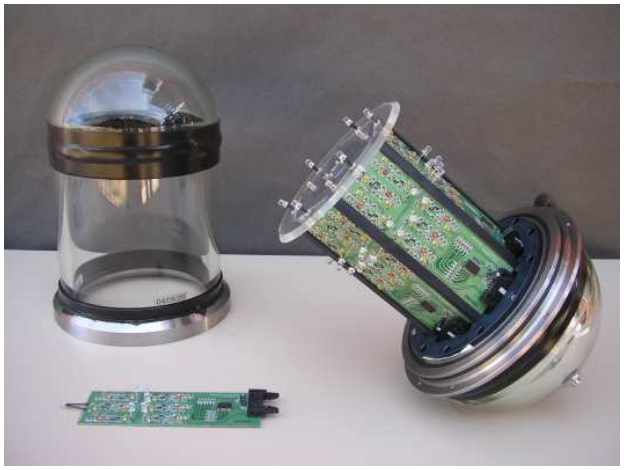

Figure 4.7: The LED hexagonal frame and its container.

which emits green light ($\lambda = 532$ nm) and short (< 1 ns, FWHM) pulses of high intensity ($\sim 1\mu$J) being capable to illuminate up to the 10th floor of every detector line.

The laser is activated using the master clock. The maximum time delay between the trigger and the emission of the light pulse is of the order of microseconds. To avoid this jitter, the emission time is measured with high precision by means of an internal photodiode integrated in the laser head and which is readout by an ARS card. The amount of light emitted by the LB can be varied by means of a voltage-controlled optical attenuator resulting from the assembly of a linear polarizer and a retarder made of liquid-crystal.

All the Laser Beacon components are enclosed in a pressure-resistant titanium container (Figure 4.8) of 17 cm diameter and 70 cm long. In the upper end-cap of the container a Lambertian flat disc diffuser spreads out the light beam following a cosine distribution. Because the laser beam points upwards, a quartz rod attached to the upper surface of the diffuser is used to minimize the transmission losses due to the accumulation of micro-organism in the outer surfaces. The rod cylinder dimensions were chosen accordingly with the refractive index of quartz to conserve the cosine distribution, due to Snell law, when light leaves the beacons through its vertical walls.

Currently, one laser beacon run of 5-10 minutes long is taken every week. This data are regularly analyzed to monitor the time offsets between the detector lines.

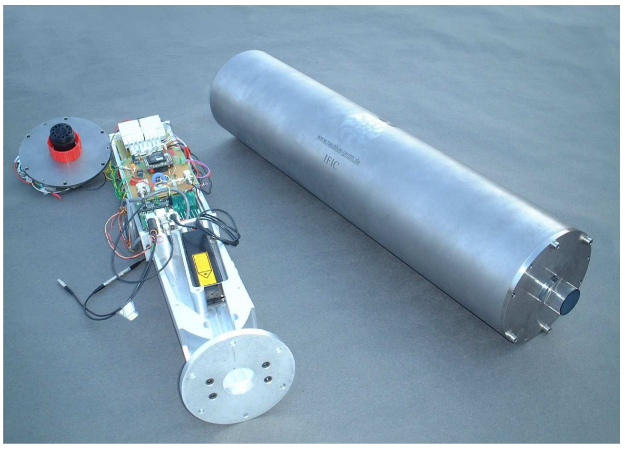

Figure 4.8: Laser beacon together with its titanium container. The internal structure holding the laser electronic components is visible on the left of the picture.

4.6 Calibration with ^{40}K

The Potassium-40 based method employs natural radioactivity of the sea water to calibrate the OMs sensitivities and relative time offsets. As said before, the decay of this isotope can produce an electron with energy sufficient to induce the emission of Cherenkov photons. If the light emission occurs in the vicinity of a storey it may illuminate two OMs in coincidence; the light is simultaneously registered by the two PMTs being the time of the two pulses correlated.

The presence of a coincident event result on a visible bump over the distribution of the relative time differences between the hits collected by two OMs in the same storey. Random coincidences occur when, by chance, two hits coming from two independent decays appear to be close in time. These coincidences are not correlated and give a flat contribution. Figure 4.9 shows an example of the time offsets distribution measured for two nearby PMTs. The observed peak is the result of a genuine coincidence signal from ^{40}K decay. This peak is well fitted with a Gaussian. In case the two PMTs monitored are well calibrated the peak offset should be equal to zero. Therefore, the measurement of the coincidences hits peak position can be used to characterize the level of agreement with respect to the time calibration parameters provided by the Optical Beacon system. At present, the data to perform this ^{40}K calibration is obtained directly from physics runs without the need to perform special dedicated calibration runs as in the past.

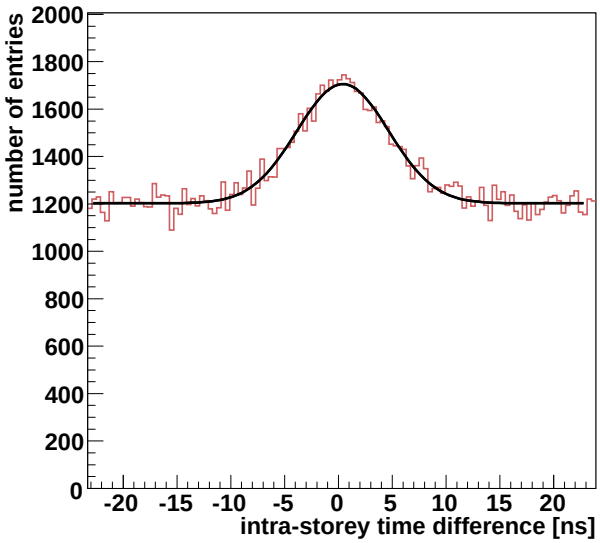

Figure 4.9: Distribution of the time differences between hits registered by two neighboring OMs in the same storey. The solid line is a fit to a Gaussian peak, due to ^{40}K decay coincidence hits, plus a flat background caused by random coincidences.

4.7 Time calibration with muon tracks

The reconstructed trajectories of the atmospheric muon events, which are detected in ANTARES at a rate of a few Hz, can be used to estimate the relative time offsets between the electronic modules. The method (discussed in detail in Chapter 7) is based on the time residual distributions derived for a sample of the collected hits which is not considered in the track fit. This procedure ensures that the observed residuals are not biased as the muon track has not been fitted to minimize them.

The atmospheric muon method has the advantage that physics data taking is not stopped to perform specific calibration runs as needed in the case of the Optical Beacon calibration. A drawback is the uncertainty introduced by the multiple scattering suffered by the muon induced Cherenkov light which spreads out the hit time residuals distributions. This could be solved by requiring good quality upgoing muon events from atmospheric neutrino interactions. However, the lack of statistics makes this an unpractical solution.

4.8 TVC measurements

The digitized hit times produced by the ARS consist of two components. The first component is the value of the 20 MHz clock signal used for the time stamp. The second component is provided by the Time to Voltage Converter (TVC) which allows finer time measurements by interpolating between two consecutive clock pulses (see Figure 4.10). Each ARS contains two TVCs operating in flip-flop mode to avoid the dead time spent to recover the ramp shape. The TVC ramp values are digitized by means of the 8-bit ADC card inside the ARS. Time conversion from ADC channels to nanoseconds is given by the translation function:

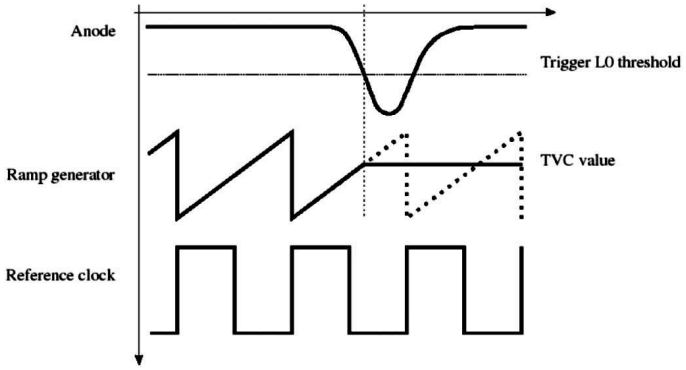

Figure 4.10: Time measurement done inside the ARS. A TVC value is generated when a signal exceeds the L0 threshold.

$$\mathrm{t(ns)} = \mathrm{T}^{0,1}_{\mathrm{slope}} \times (\mathrm{tvc} - \mathrm{TVC}^{0,1}_{\mathrm{min}}) \tag{4.3}$$

with

$$\mathrm{T}^{0,1}_{\mathrm{slope}}(\mathrm{ns/bit}) = \frac{\mathrm{Clock\ Period} = 50\ \mathrm{ns}}{(\mathrm{TVC}^{0,1}_{\mathrm{max}} - \mathrm{TVC}^{0,1}_{\mathrm{min}})}, \tag{4.4}$$

where tvc is the measured TVC value and the indexes (0,1) distinguish between the two TVCs in each ARS board. Only the $\mathrm{T}_{\mathrm{slope}}$ parameter needs to be evaluated for calibration as will be explained in Chapter 5.

4.9 Effects of the front-end electronics

In ANTARES a total of 2700 front-end ASICs electronic boards, the ARS chips, process the photo-tube signals (that cross the pre-defined L0 threshold), measure their arrival times, amplitudes and shapes and also perform monitoring and calibration tasks. Despite all these functionalities, limitations of the ARS capabilities to process the analog signals have been shown to influence the hit time measurements in a non negligible way. Description of the main effects on the signals time processing is given below.

4.9.1 Walk effect

The fact that the analog signals recorded by the PMT are discriminated by the ARS using a fixed amplitude threshold leads to the so-called *walk effect*: signals with higher amplitude cross the discriminator earlier than simultaneous signals of lower amplitude, which introduces a delay in the arrival time of the PMT signals which depends on the collected charge (see Figure 4.11). The effect can be corrected using waveform information of the PMT signal which allows to extract the photo-electron pulse shape. This extraction is done by fitting the average waveform obtained from SPE events of all detector ARS. The walk-effect is systematically corrected before event reconstruction.

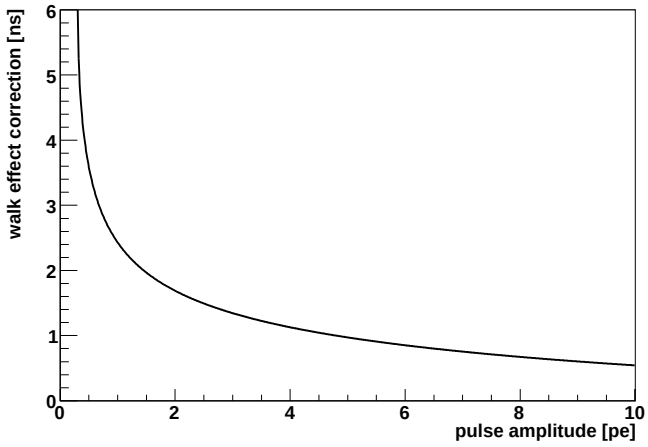

Figure 4.11: Time offset introduced by the walk-effect as a function of the PMT pulse amplitude expressed in units of photo-electrons.

4.9.2 Differential Non Linearities

The Differential-Non-Linearities (DNL) consist on the unequal bin size of the ADC channels of the TVC caused by an imperfection on the ARS comparator used for the conversion of the analog signal into a binary output. The DNLs effect produces changes in the shape of the time distributions that affect the time measurements. The DNLs are particularly problematic in the analysis of the LED OB data, where the signals are always digitized with approximately the same value of the TVC, since the LED Beacons runs are triggered synchronously with the master clock.

Several approaches have been proposed in order to correct the effect of the DNLs. One way is to reassign a new width to each ADC channel, so overfilled bins will get a larger width and conversely for under-filled bins. This can be done by computing the TVC cumulative distributions normalized to 50 ns. For each ADC channel in the horizontal axis a different bin size (the vertical axis, or bin content) is assigned. In this way, instead of assuming a linear behavior within the TVC dynamic range $(\mathrm{TVC}_{\mathrm{min}}, \mathrm{TVC}_{\mathrm{max}})$, the time corresponding to each ADC channel is assigned depending on the bin size. The main drawback of this procedure is that it would require to store in the database the amount of 256 values for each TVC ramp, which means to introduce near 1 million parameter values in the calibration tables (evidently an unpractical solution).

4.9.3 Early-photon effect

The "early-photon effect" is a consequence of the inability of the PMTs to resolve multiple photons arriving very close in time. This is a common situation during LED Optical Beacon runs, where short and high intensity light flashes are emitted. The result is that only the time of the first photons is recorded. This effect, which is further emphasized by the walk-effect, has a linear dependence with the distance between the light source and the OM being illuminated: the closer it is, the more light it receives and therefore the sooner the PMT signal crosses the threshold of the ARS.

5

Results on time calibration

As mentioned earlier, achieving a good muon track reconstruction demands the precise measurement of the arrival times of the Cherenkov photons induced by muon tracks passing through the detector. In this chapter, we introduce a method based on atmospheric muon data which fulfills the requirements on time calibration. This method is described and the results obtained are presented with focus on the measurement of the relative time offsets between the detector lines. Additionally, the calibration and stability of the TVC parameters is discussed.

5.1 Time calibration with muon tracks

Muons from cosmic rays interactions in the atmosphere are detected in ANTARES at a rate of 5-10 Hz. These events can be used to accomplish the detector time calibration without stopping the acquisition of the physics runs, as it is required when using the Optical Beacon system. The method is based on the hit time residuals, which are defined (see Chapter 3) as the difference between the measured arrival time of the collected photons to the PMTs and the time expected from the reconstructed trajectory of the muon given a certain set of track parameters. The distribution of these residuals is shown in Figure 5.1 for events in a small sample of data runs. The sharp peak around zero is populated with photons originating from a muon and arriving directly to the OM without suffering scattering, so their arrival times are only perturbed by the effect of the TTS of the PMT. The tail of the distribution is caused by photons from secondary electrons or scattered photons in the water, so they

arrive delayed with respect to the direct photons. Finally, optical background photons give a constant baseline contribution.

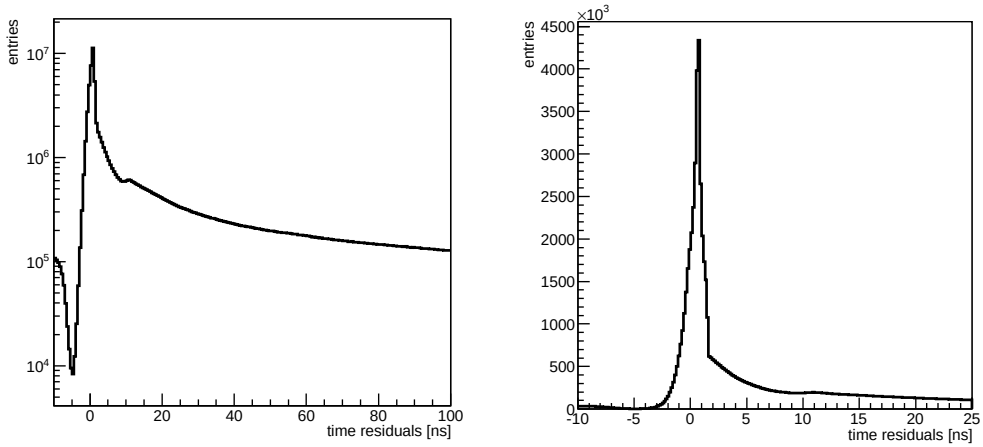

Figure 5.1: Time residuals (all ARSs) from data events using runs recorded with the 12 lines detector fully operative. Distributions are shown in logarithmic (left) and linear (right) scales.

The position of the peak of the distribution depends on the time calibration constants: if a time offset is not properly corrected the peak would appear shifted with respect to the "correct" position as given by the time PDF used in the reconstruction algorithm. We can exploit this feature to calculate time corrections. In this work we probe the capability of this method based on track residuals to measure the time offsets between detector lines. Its ability for determining the $\mathrm{ARS\_T0}$ calibration parameters is later discussed.

5.2 Inter-line calibration

As said in the previous chapter, during the integration of each detector line, time measurements are performed in a dedicated dark room using a laser system to illuminate the PMTs. For each single OM, time deviations with respect to the reference OM of the line[1] are calculated and then corrected. However, no further calibration was performed off-shore to determine the time differences between the optical modules used as reference in the different lines. These time differences have to be corrected in-situ.

[1] This is one of the OMs placed in the lowest storey of the line.

The first hint of the existence of time offsets between the detector lines was found studying the distributions of the quality reconstruction parameter [112]. A large discrepancy between data and MC simulations was found in the tracks traversing the detector diagonally, whereas tracks that went straight down showed better agreement at higher Λ values. A method for measuring these offsets based on the reconstructed trajectories of the atmospheric muons was promptly developed within the `aafit` software framework. A detailed description of the procedure is given below.

5.2.1 Method description

Using physics events we aim to determine the quantities $T_{\rm line}^{\rm off}$ corresponding to the relative differences in the hit times measured by each line with respect to a common reference value defined for all the lines. The next iterative procedure is followed:

1. A "probe-line" is randomly selected among all the lines which have collected hits.
2. The muon track is reconstructed using only the hits recorded in the other lines.
3. Time residuals for the probe-line are calculated with respect to the fitted track.
4. Distributions of these residuals are histogramed and the peak is fitted with a Gaussian function, whose mean value is interpreted as the line offset ($T_{\rm line}^{\rm off}$).
5. Hit times are corrected with these time offsets.

The previous 5 steps are repeated for a new iteration. The complete process ends when the recomputed offsets are small enough ($T_{\rm line}^{\rm off} < 0.5$ ns). Excluding the probe-line hits ensures their time residuals are not biased as the muon track has not been fitted to minimize them. The top plot in Figure **??** shows the distributions of these probe-line residuals obtained after the first iteration of the procedure and using data runs gathered in November 2010. The fit range was chosen to avoid the contribution from scattered photons and to match the most Gaussian-like region of the distribution.

The reconstructed muon tracks which are used for the computation of the residuals are also influenced by the offsets. The quality of the reconstruction improves with the number of iterations and, therefore, the number of reconstructed events with larger quality parameter

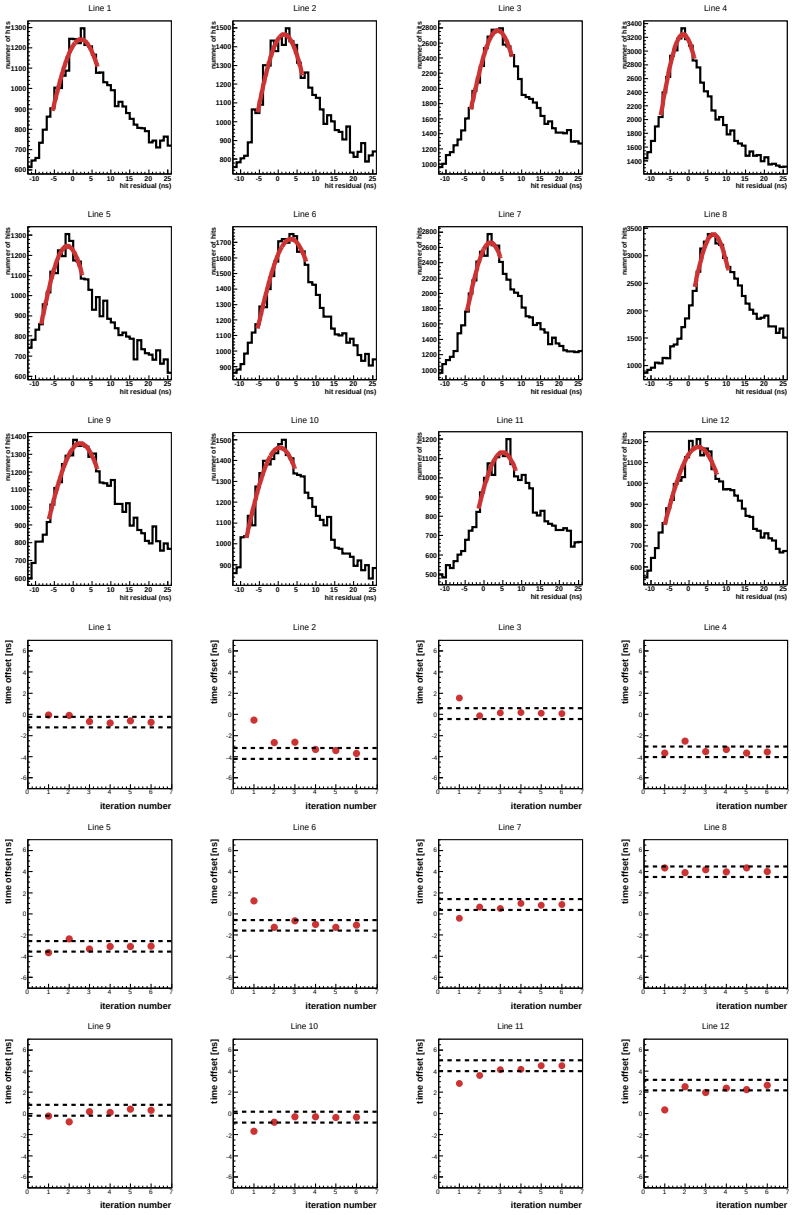

Figure 5.2: (Up) Distributions of probe-line time residuals after a first iteration of the method. The peak is fitted using a Gaussian function whose mean value is taken as $T_{\text{line}}^{\text{off}}$. (Down) Cumulative time offsets as a function of the iteration number. The dashed lines indicate ± 1 ns distance from the last iteration point.

Line	L1	L2	L3	L4	L5	L6
Offset	-1.26	-3.87	-0.50	-2.13	-3.42	-1.29
Line	L7	L8	L9	L10	L11	L12
Offset	0.63	4.91	0.27	-0.47	3.96	2.15

Table 5.1: Interline offsets measured with the track residuals method. These values are currently used for data processing.

values increases. The procedure reaches a solution as the corrections converge to a common limit. The spread of the corrections about this limit is $\sigma(T^{\rm off}_{\rm line}) < 0.5$ ns (see Figure 5.3).

Using runs recorded in March 2010 we have determined the inter-line offsets corrections that we have to apply to the data. These values are summarized in Table 5.1 and shown in Figure 5.4. Because we are interested in correcting relative differences we have subtracted a common constant (of about 2 ns) to obtain the final set of inter-line offsets corrections. The largest deviation (~ 5 ns) was found on line 8. This line has some particularities, which are discussed in Section 5.2.3.

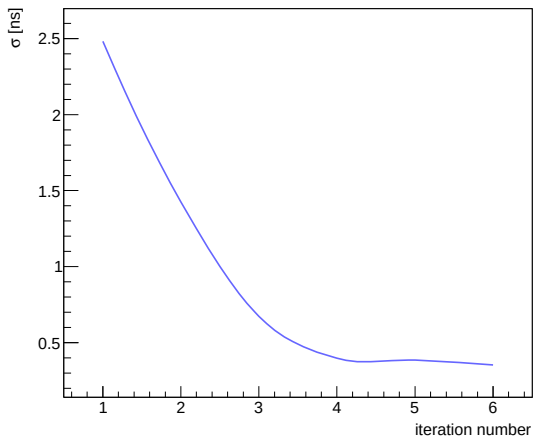

Figure 5.3: Width of the inter-line time corrections as a function of the number of iterations of the procedure.

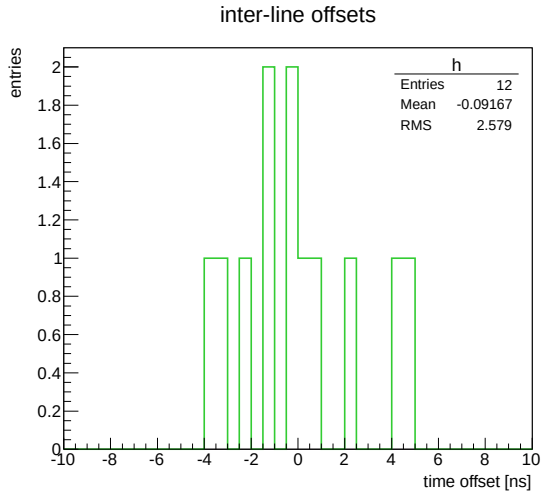

Figure 5.4: Inter-line offsets measured using the distributions of the time residuals from reconstructed muon tracks.

5.2.2 Impact on the reconstruction

Once the inter-line timing is corrected we verify an improvement in the reconstruction which is reflected by an enhancement of events at high Λ values. The improvement is particularly important (see Figure 5.5) for events crossing the detector diagonally, while for vertically down-going events, which are mostly single-line reconstructed, the improvement is slighter, as expected. Data and MC distributions of the Λ parameter are in good agreement after calibrating the line offsets.

In order to study the effect of the inter-line timing on the detector resolution we have compared the standard simulation with MC events reconstructed after miscalibrating the lines timing by artificially adding offsets to the hit times. Figure 5.6 shows the distribution of the angular difference (Ψ) between the reconstructed track direction and the generated one (i.e. the true neutrino direction) for the default MC (solid line) events and for the events reconstructed using miscalibrated lines: adding the offsets results on about 40% degraded resolution for the selected events ($\Lambda > -5.4$ & $\cos(\theta) > 0.0$ & $\beta < 1^\circ$). The median value of the distribution worsens from a value $\psi \sim 0.40^\circ$ to $\psi \sim 0.55^\circ$ for the subsample of MC runs analyzed.

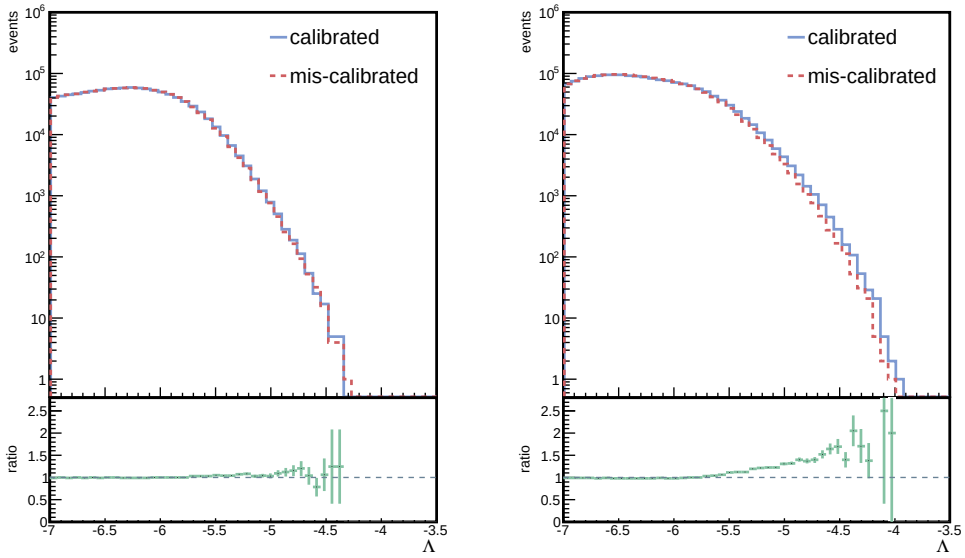

Figure 5.5: Distributions of the reconstruction quality parameter before and after correcting the inter-line offsets for (left) vertically down-going tracks ($\cos(\theta) < -0.9$) and (right) inclined tracks ($cos(\theta) > -0.8$). The lower pads show the ratio between the number of events reconstructed after applying the inter-line timing correction and before correcting the time offsets. An improvement of up to a factor 2 is observed for inclined down-going events when correcting the inter-line offsets we have measured using atmospheric muon data.

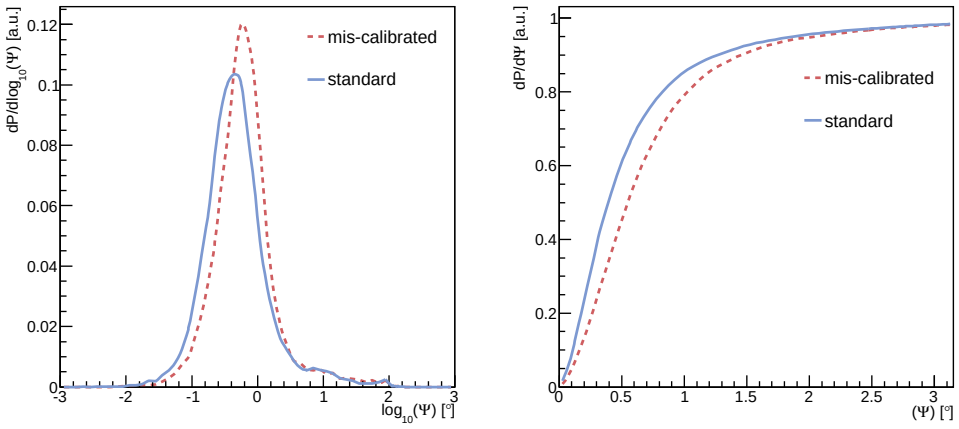

Figure 5.6: (Left) Angular error for degraded timing MC tracks (dashed line) and standard simulation (solid line). (Right) The corresponding cumulative distributions.

5.2.3 Comparison with the Laser OB system

The Laser Beacon can be used as well to determine the time offsets between the detector lines [110]. This system provides an independent calibration method to cross-check the results obtained using the information of the track residuals. For this purpose, one single calibration run is taken every month in ANTARES, when the laser at the bottom of line 8 illuminates the detector for about 10 minutes. These data are then analyzed following a similar procedure as the one applied for the ARS_T0 in-situ calibration [110]. The method is based on the study of the time differences between the emission of the light pulse and the time when this light is detected by the OMs. By correcting for the time it takes the light to travel from the source to the optical modules, time residuals are calculated. Their corresponding time residual distributions are fitted to a Gaussian function convoluted with an exponential, which produces more stable results. The fit peak values obtained are then plotted as a function of the distance from the OM to the Laser Beacon position. Only those OMs which are illuminated by the laser at the photo-electron level are used in the calculation, because in that region a constant relation between residuals peak position and the distance to the light source is expected. The resulting time peak versus OM distance distribution is fitted (see Figure 5.7) to a polynomial function of degree zero (a flat line). The coefficient of this second fit defines the time offset of the line.

In Figure 5.8 the inter-line offsets measured with the Laser OB are compared to the results obtained using the track residuals method. The values (which are summarized in Table 5.2) agree within 1 ns, except for line 1 and line 8. In particular, for the later detection line there is a discrepancy larger than 2 ns. This line is indeed problematic because the Laser Beacon is placed at its bottom, so its light does not arrive directly to the OMs. This discrepancy will be clarified by analyzing the data obtained with a new laser (already deployed at the bottom of the IL 11, which is outside the ANTARES layout) that has been recently connected.

Examining the reconstructed events we found that, by correcting for the inter-line offsets provided by the track residuals method, the number of high quality tracks is slightly larger than what we obtain using the time offset corrections measured with the Laser Beacon (see Figure 5.9). This result supports the use of the track residuals inter-line offset as the official calibration parameters for data processing.

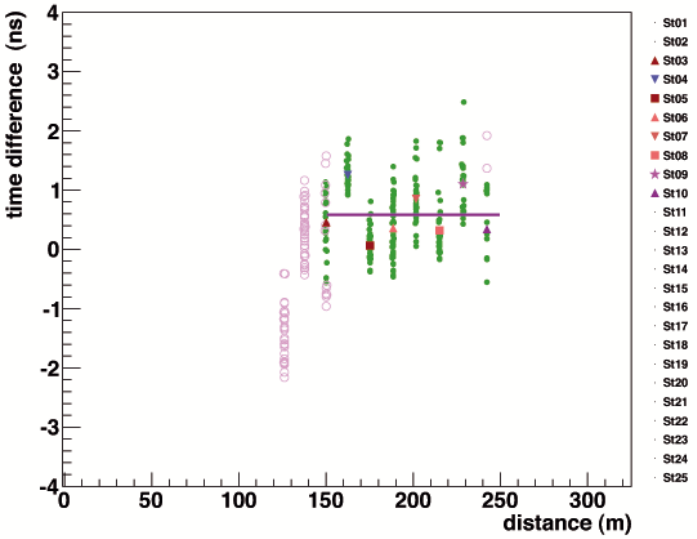

Figure 5.7: Time difference (peak of the fit to a Gaussian plus exponential convoluted function) versus the distance from the OM to the Laser Beacon position. The filled circle marks indicate which values are fitted to the flat line while the empty circles refer to those OMs which are not used in the fit. The other markers in the plot refer to the average value of the time differences calculated with the OMs in a particular floor or storey.

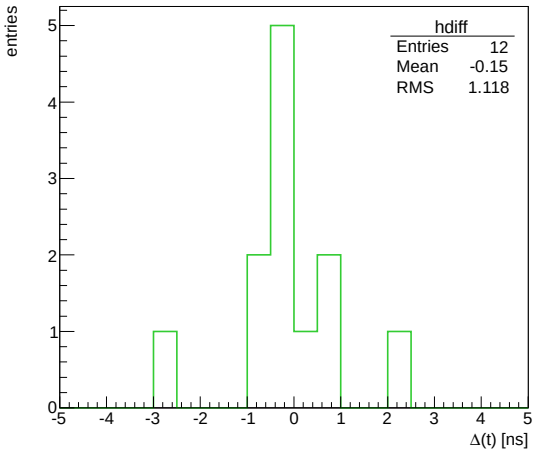

Figure 5.8: Differences between the inter-line offsets measured using the reconstructed muon tracks and the values obtained using the Optical Beacon system.

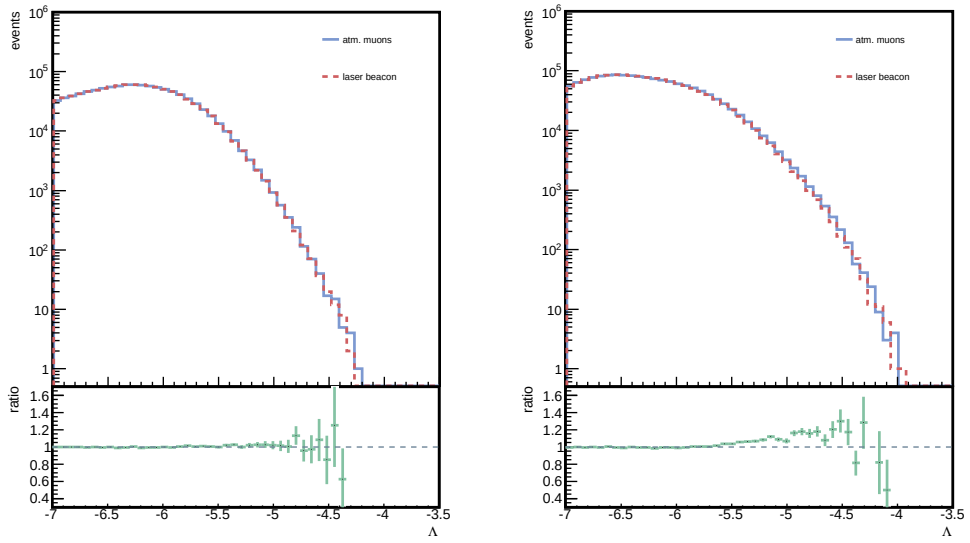

Figure 5.9: Distribution of the quality of the reconstruction parameter for events that have been reconstructed ($\cos(\theta) < -0.9$ left, $\cos(\theta) > -0.8$ right) using the inter-line offset corrections provided by the track residual method (solid line) and those obtained using the laser Beacon data (dashed line). The bottom plot shows the ratio between the number of reconstructed events for each case (muons/laser).

Line	TR offset [ns]	LB offset [ns]	Difference [ns]
1	-1.3	-3.3	2.0
2	-3.9	-3.4	-0.5
3	-0.5	0.0	-0.5
4	-2.1	-2.0	-0.1
5	-3.4	-3.5	0.1
6	-1.3	-0.6	-0.7
7	0.6	-0.3	0.9
8	4.9	7.8	-2.9
9	0.3	0.5	-0.2
10	-0.5	-0.4	-0.9
11	4.0	4.6	-0.6
12	2.1	1.3	-0.8

Table 5.2: Interline offsets obtained applying the track residuals method (TR) and using the Laser Beacon (LB) data and their differences.

5.3 Inter-line offset stability

No changes in the inter-line time offsets are expected if no reference PMTs are substituted or their HV are tuned. However, it is always interesting to monitor the stability of the calibration parameters. In Figure 5.10 the inter-line offsets measured using the method of the track residuals as a function of time are shown. The studied period covers the years 2008 to 2012. For each measurement we have used about 50 runs collected in periods when every detector line was operative. The distribution of the measurements per line we have done has a RMS smaller than 1.0 ns, which can be understood as an estimation of the accuracy of the method. At the moment of writing no need for updating the inter-line timing constants has been found and a unique set of calibration parameters is used for data processing.

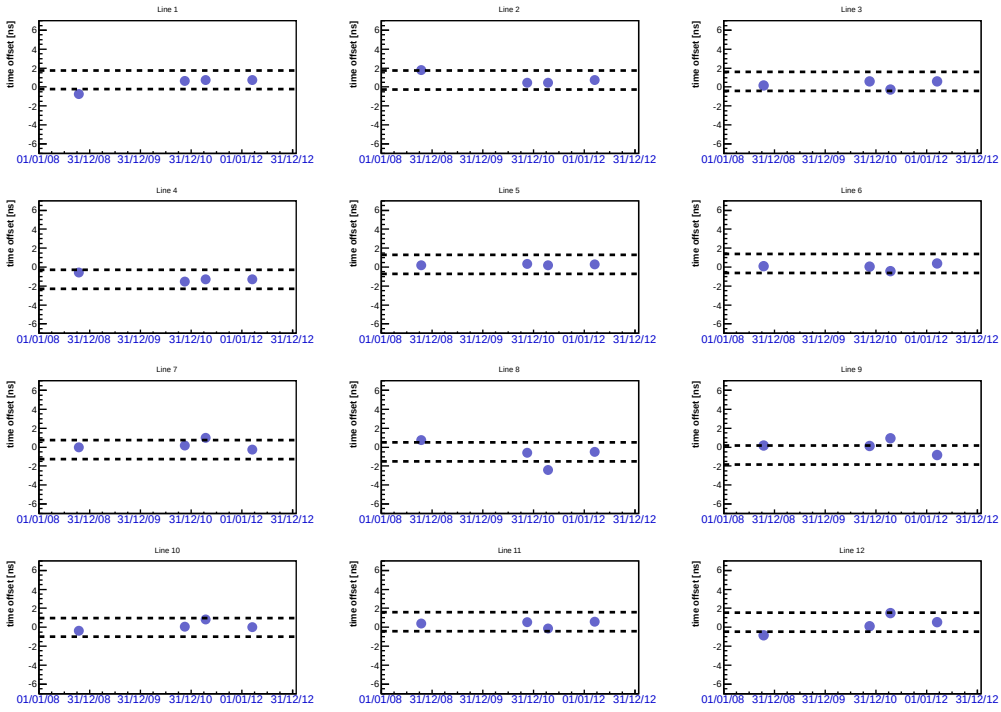

Figure 5.10: Measurements of the inter-line offsets as a function of time. The RMS of the Y-projection of these values is smaller than 1 ns.

5.4 Intra-line calibration

Calibrating the lines means to find a common reference for all the OMs in the detector. Prior to this, the intra-line offsets, i.e. the corrections we need to apply to calibrate every OM inside a line with respect to the reference OM in the line, have to be determined. These intra-line corrections that we refer to as the $\mathrm{ARS\_T0}$ time calibration constants are currently provided by the LED OB system. In this section we discuss the possibility of using the track residual method to measure the complete set of time calibration constants. To accomplish this, it would be particularly interesting to cross-check the $\mathrm{ARS\_T0}$ for those OMs which can not be directly illuminated by the LED OB system due to their position in the line; the OMs placed below the LED beacons or those which are too far from the LED light source that result poorly illuminated.

For the intra-line calibration the procedure we follow is analogous to the one used in order to calculate the inter-line offsets corrections (Section 5.2.1) but, in order to accumulate enough statistics using a reasonable number of data runs, we first loop over the hits per event to pre-select the OMs which have collected at least one hit. These OMs will be used to calculate the unbiased probe-hit residuals per ARS: having N number of OMs with hits, every track is reconstructed N times by removing from the fit the hits collected by the current probe-OM. As a first test, we have applied the track residuals procedure on data collected in early 2010. An example of the unbiased time residual distribution obtained is shown in Figure 5.11. By fitting the peak of the distributions to a Gaussian function the ARS time offsets are determined. The distribution of these offsets, as obtained for all ARSs with sufficient entries, has a RMS of about 0.6 ns (see Figure 5.12). Because the LED OB calibration constants are used during the event reconstruction, we are actually calculating corrections to the T0s obtained using the Beacons. Being 90% of these corrections smaller than 1 ns we validate the T0 timing provided by the LED OB calibration method. At the moment of writing, the track residuals method have only been applied to cross-check the LED Beacon results on the $\mathrm{ARS\_T0}$ calibration. Work is in progress to evaluate the feasibility of this procedure to determine the full set of time calibration constants.

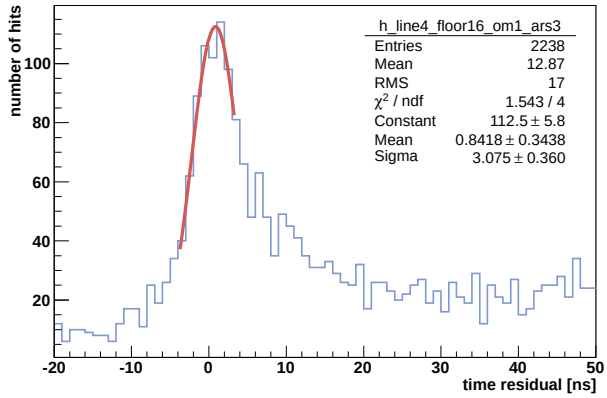

Figure 5.11: Unbiased time residuals distributions for the ARS 3 in the floor 16 of line 3. The peak of the distribution has been fitted to a Gaussian function whose mean value is interpreted as the ARS time offset.

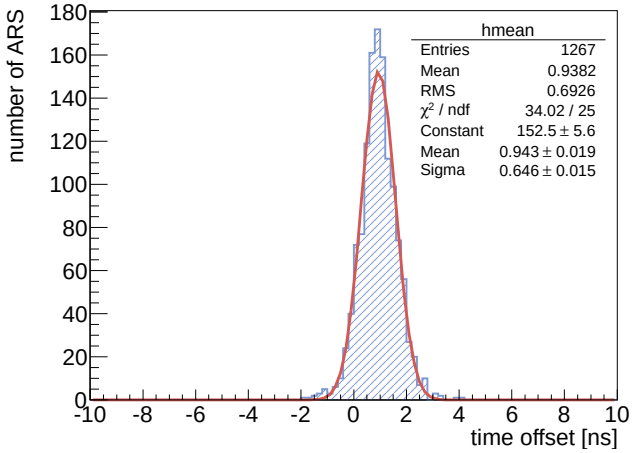

Figure 5.12: Distribution of the ARS time offsets corrections determined by the track residuals method. The small width of the distribution confirms the goodness of the LED OB calibration.

5.5 TVC calibration

The TVCs inside each ARS are used to perform high precision time measurements of the electronic signals collected by the PMTs. Ideally, the TVC dynamic range has 256 ADC channels, which means a resolution of $\sigma = \Delta t\ \sqrt{12}$ ~0.05 ns, where $\Delta t = 50/256$ ns. This resolution assumes an equal TVC binning and the full use of the available dynamic range. However, in reality only ~150 ADC channels are used and not all the bins have the same width because the effect of the DNLs (see Figure 5.13), so the effective precision is about 8 times worse.

Calibrating the TVCs requires to determine the effective dynamic range of the TVC distribution, i.e. the $\mathrm{TVC_{min}}$ and $\mathrm{TVC_{max}}$ parameters. By using random signals uniformly distributed in time we determine the $\mathrm{TVC_{min}}$ and $\mathrm{TVC_{max}}$ parameters, assuming the TVC ramps to be linear, as the first and the last bin respectively to exceed 10% entries of the TVC distribution average bin occupancy. This procedure is used to calibrate each TVC ramp individually. In Figure 5.14 the $\mathrm{TVC_{min}}$ and $\mathrm{TVC_{max}}$ values extracted from one single Physics run acquired in August 2009 are shown for all the TVCs available in the detector.

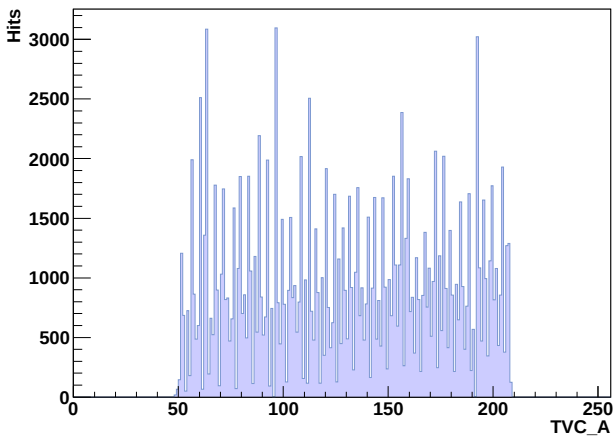

Figure 5.13: Example of a TVC distribution from random signals. Only about 150 channels are useful for timing. The average bin content of these distributions is used to determine the $\mathrm{TVC_{min}}$ and $\mathrm{TVC_{max}}$ parameters for the two TVC ramps in each ARS.

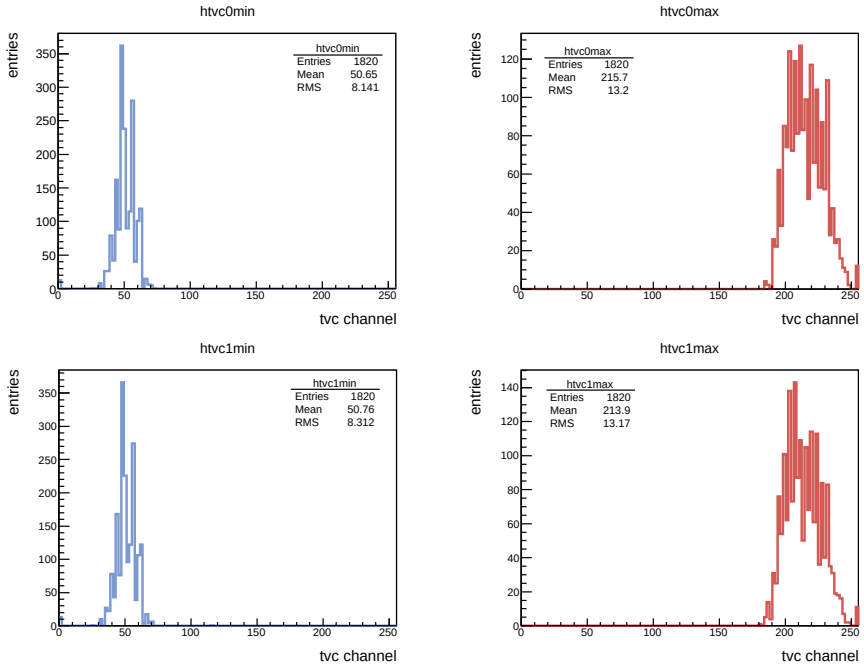

Figure 5.14: Distributions of the $\mathrm{TVC}_{\mathrm{min}}$ and the $\mathrm{TVC}_{\mathrm{max}}$ parameters for the two TVC ramps in each ARS.

TVC	ramp	mean	RMS
TVC_{min}	0	50.2	0.4
TVC_{max}	0	215.1	0.3
TVC_{min}	1	50.3	0.3
TVC_{max}	1	213.3	0.3

Table 5.3: Mean and RMS values of the distributions of the TVC parameters (all ARSs) obtained using runs collected along several years of data taking.

5.5.1 Monitoring of the TVC parameters

In order to study the stability of the effective TVC dynamic range we have used more than 20 runs recorded in a period of more than 4 years (from May 2008 until December 2012). Figure 5.15 shows the evolution of the mean values of the TVC_{min} and TVC_{max} distributions for each TVC ramp. In the upper plot these values are shown for all ARS while in the bottom plot they are split in detection lines. The mean and RMS values of the projection histogram for the TVC_{min} and TVC_{max} evolution top plot that includes all ARSs are summarized in table 5.3. The small width ($\sigma \sim 0.4$ channels) probes the TVC dynamic ranges are stable at the level demanded by the time calibration in the studied period.

Indeed, small variations are expected for the TVC constants only after performing the HV tuning on a group of detector channels (which may happen twice a year) or after the deployment of a new line, because the environment temperature and pressure conditions influence the operation of the TVC electronics. In May 2008 took place the operation which led to the connection of the lines 11 and 12 to the Junction Box completing the detector. In order to update the TVC parameters measured in the dark room with *in-situ* calibration constants, the TVC_{min} and TVC_{max} parameters for all ARSs were calculated using real data. A comparison between the TVC parameters obtained *in-situ* and the dark room set is shown in Figure 5.16 for the lines 5 and 12. It clearly shows the change in the TVC values after the line connection and so the need for an update TVC calibration. To measure the impact on the reconstruction of the TVC calibration set update, events in one single physics run were reconstructed using the dark room measurements (v10.746.202) and the values obtained *in-situ* (v16.684.668). Figure 5.17 shows the track fit quality parameter for both groups of events. The difference in the number of reconstructed events is negligible because the

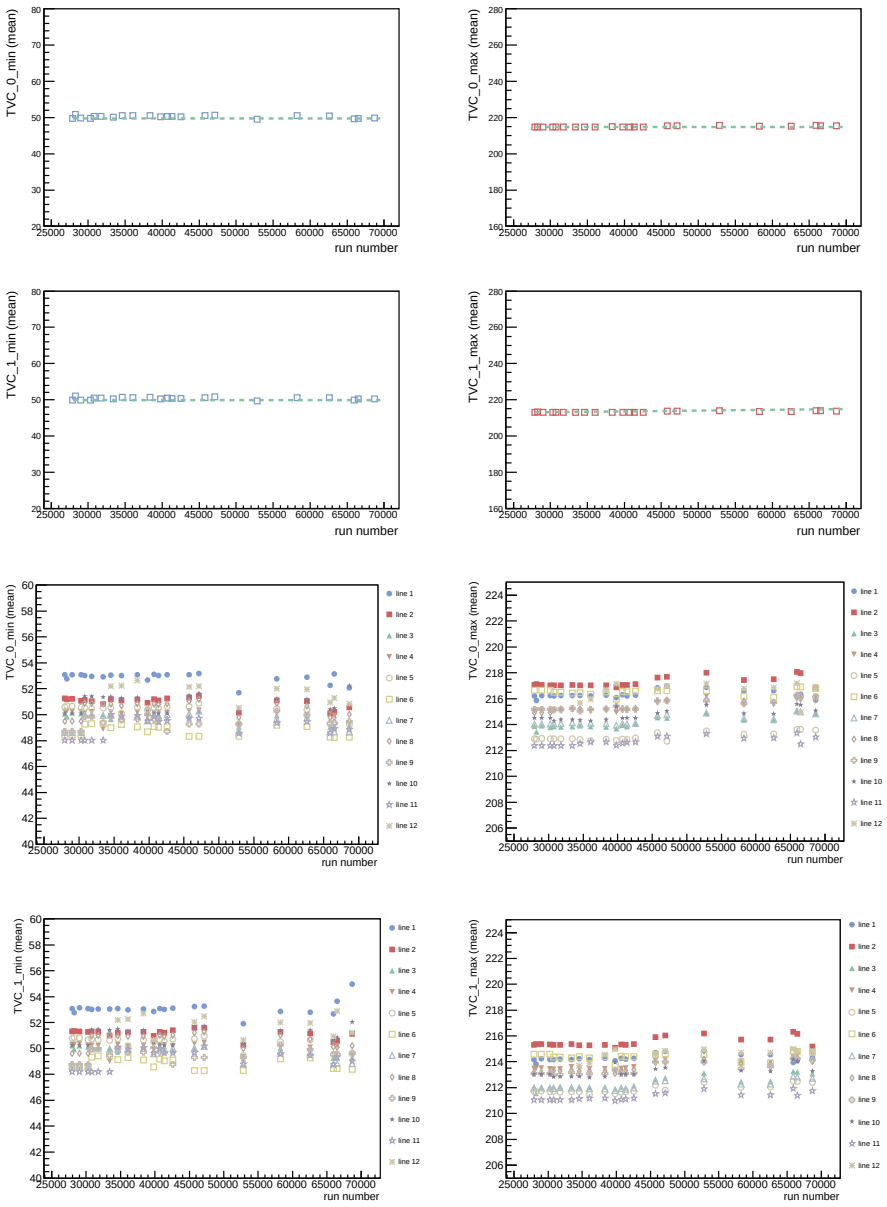

Figure 5.15: Distributions of the mean values of the $\mathrm{TVC_{min}}$ and $\mathrm{TVC_{max}}$ parameters versus the run number for all ARSs (top). Mean $\mathrm{TVC_{min}}$ and $\mathrm{TVC_{max}}$ values for ARSs in each detector line (bottom).

robustness of the reconstruction method at the level of the TVC time corrections.

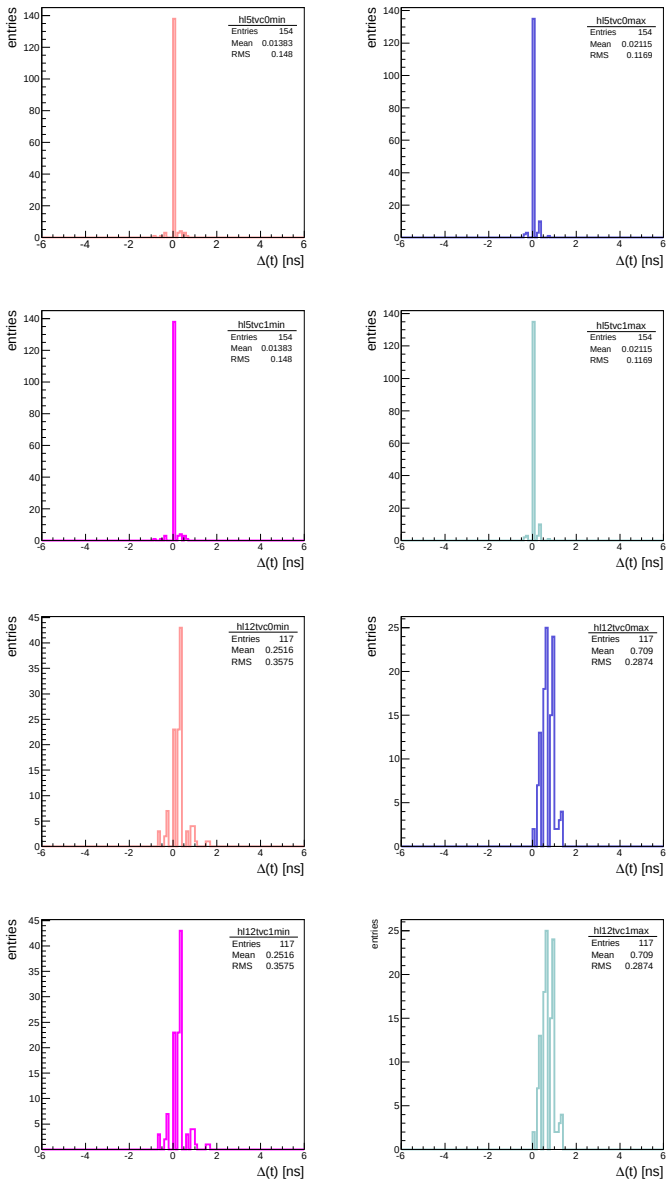

Figure 5.16: Variations in the TVC channels (translated to ns) for the ARSs in lines 5 (top) and 12 (bottom) from using dark room values and the updated *in-situ* TVC set. The variation of the TVC parameters after the deployment of the line 12 is clearly noticeable.

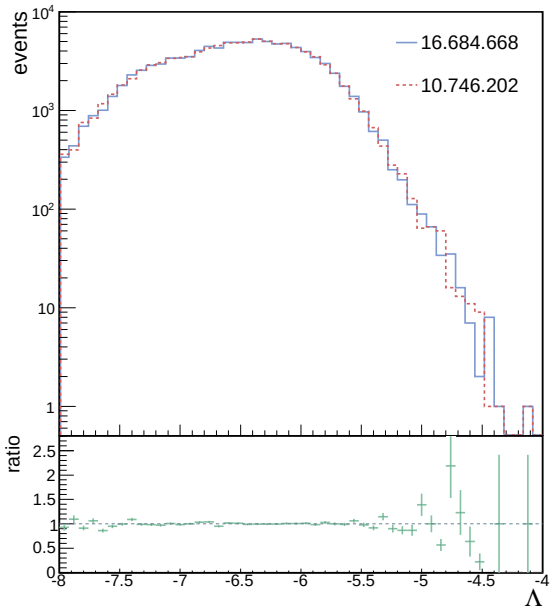

Figure 5.17: Quality of the reconstruction parameter distributions for events processed using dark-room TVC parameters (v10.746.202) and *in-situ* TVC constants (v16.684.668).

6

Data and simulation comparison

In this chapter, the data selection and processing and the criteria to select the final sample of neutrino candidate events that is used to search over for cosmic neutrino sources are described. The level of agreement between data and MC simulation is discussed for particularly interesting distributions and the detector response is studied for neutrino fluxes with a $\propto E^{-2}$ energy spectrum.

6.1 Data selection and processing

In order to decide which runs (among all the runs recorded in near four years of ANTARES operation) are included in the physics analysis, a selection criterion is defined on the basis of data quality principles. A review of the data taking conditions along this period and the description of the data processing and calibration are presented. The computation of the analysis livetime, which amounts for 813 days for the data selected, is described as well.

6.1.1 Run selection

The data used in this work were collected during the period between January 29th, 2007 and December 31th, 2010. From a total of $\sim 10^4$ runs recorded in these four years, we have chosen those satisfying the following set of minimum requirements:

1. An effective run duration $\mathrm{T_{eff}} > 1000$ s,

2. An apparent run duration similar to its effective duration ($0 \leq T_{app} - T_{eff} \leq 450$ s)[1],
3. No double frames, i.e., there is not an ARS producing more than one frame in a given timeslice.
4. No synchronization problems: a) no more than 2% of timeslices with an offset between their start time and the reset-time-stamp signal, b) no more than 2% of timeslices with frame(s) exhibiting a mismatch between their time time, c) the index of the last timeslice has to matches (roughly) the total number of slices.
5. A reasonable muon rate between 0.01 Hz and 100 Hz,

All this information is stored in the `Data_Quality` table of the ANTARES data base and can be retrieved through SQL commands. Runs with high hit multiplicity events (see Figure 6.1), which is a characteristic of sparking OM activity, were removed from the resulting list of runs. Because they can not be properly simulated, runs for which the information of the detector conditions was not recorded were discarded as well. The 7419 runs selected can be grouped in four different categories according to the Qbasic quality flag which takes higher values for better quality data[2]:

1. Qbasic $= 1$, identifies those runs that satisfy the set of minimum requirements previously introduced.
2. Qbasic $= 2$, defined for runs where at least 80% of the OMs expected to be working are effectively working at the data taking time.
3. Qbasic $= 3$, when the baseline rate is below 120 kHz and the burst fraction < 0.4 (silver runs).
4. Qbasic $= 4$, for those runs recorded with baseline rate $<$ 120 kHz and a burst fraction < 0.2 (golden runs).

Figure 6.2 shows, for the majority of the selected runs, the Qbasic flag as a function of the run number as well as the number of runs recorded under each of the four mentioned Qbasic flags.

[1] The apparent run duration is defined as the difference between the run acquisition stop time and its start time, while the effective duration is the product of the number of frames times the frame duration.

[2] A run with a given Qbasic value will also fulfill the conditions defined for smaller Qbasic values.

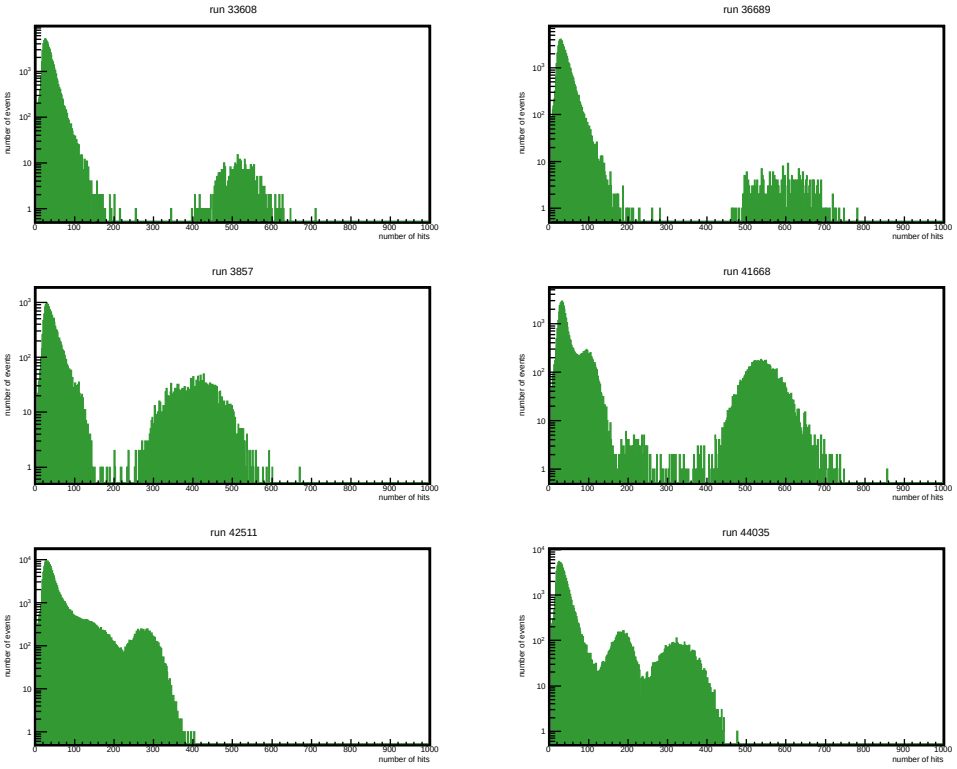

Figure 6.1: Distribution of the number of hits for several anomalous runs showing an excess of events as result of sparking OM activity.

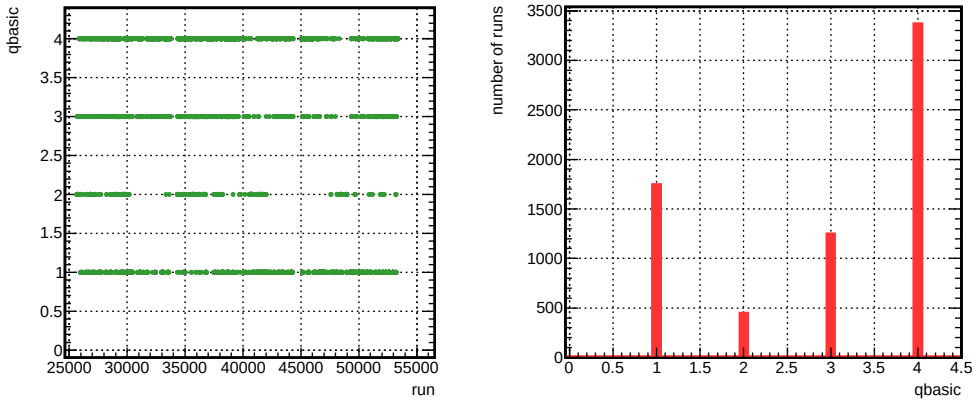

Figure 6.2: Quality flag for selected runs as a function of the run number (left). Number of runs included in each of the different quality categories (right). Golden and silver runs dominate the sample.

6.1.2 Data taking conditions

During the data taking period we have analyzed, the detector operated under different configurations. The first data runs selected were recorded when only 5 detection lines had been installed. The acquisition continued in this mode until the installation of five more lines during a sea operation carried out in December 2007. The subsequent period of 10 lines lasted near four months, until the connection with line 4 was lost. Data collection proceeded using the remaining 9 operative lines. In May 30th 2008, the operation for the ANTARES detector completion took place. Soon after starting taking data in the full detector configuration, the connection with the apparatus was lost due to the fail of the MEOC cable. The cable was repaired and connected in September, continuing smoothly the data taking in the full detector configuration. As of January 2009, line 10 had to be disconnected due to a problem with the "Y" link cable. Additional problems also affected lines 12, 9 and 6 during 2009. The detector run with eleven lines since November 2009 and until the reconnection of line 9 almost one year later. The recording of the last data run included in this analysis began last night of 2010.

The optical background conditions during these 4 years are shown in Figure 6.3. The baseline rate, computed as the mean value of a Gaussian distribution fitted on the rising slope of the counting rate distribution, and the burst-fraction, obtained as the fraction of entries in the counting rate distribution giving a rate higher than the mean value of the Gaussian distribution plus 20% of this mean value, are plotted as a function of the run number. Two periods of high rates can be distinguished around run numbers 41000 and 48000. In Section 6.3 we discuss how such extreme conditions can affect the muon track reconstruction.

6.1.3 Data processing and calibration

All the selected data runs were processed and calibrated within the SeaTray framework[3] using up-to-date calibrations (see Table 6.1) by reading the corresponding parameters stored in the ANTARES data base, with processing date as of May 27th, 2011. To obtain the alignment constants the last software version available was used. All calibration constants with their

[3]SeaTray [113] is a software framework for data analysis and MC simulation with a core that has been developed by the IceCube Collaboration [114] and later extended for under-water neutrino telescopes.

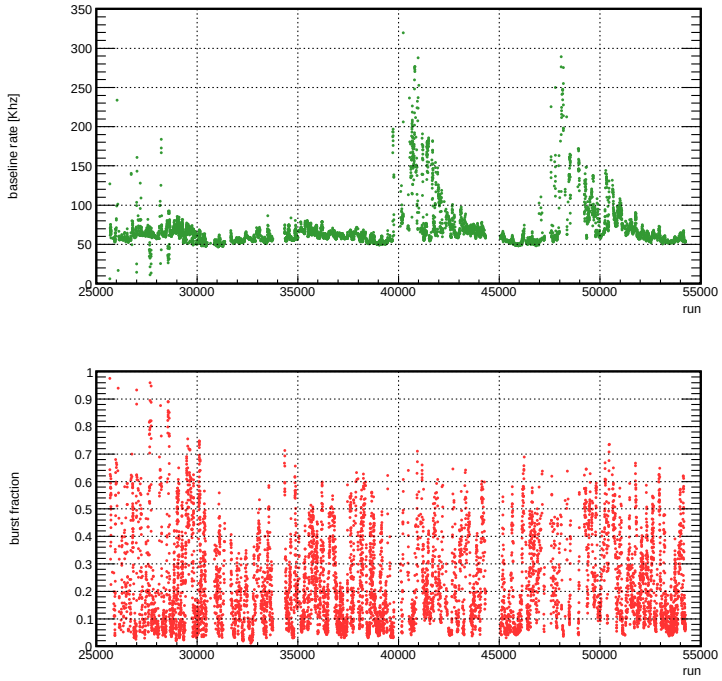

Figure 6.3: Baseline rate (top) and burst-fraction (bottom) for runs used in this analysis. Two flaring periods are visible for two relatively large group of runs (around run numbers 41000 and 48000).

Table 6.1: Summary of all calibration sets used.

First run	Last run	Label
25669	26769	2007:L5:V6.0
26770	27658	2007:L5:V6.0-bis
27659	28803	2007:L5:V6.1
28980	29761	2007:L5:V6.1-bis
29762	30427	2007:L5:V6.2
30508	31374	2007:L10:V7.0
31675	32491	2008:L10:V7.1
32529	33756	2008:L10:V7.2
34346	34976	2008:L12:V6.0
35000	36215	2008:L12:V6.1
36218	37475	2008:L12:V6.2
37591	38759	2009:L12:V6.3-interlineoffset
38760	39589	2009:L12:V6.4
39590	40809	2009:L12:V6.6
40841	42425	2009:L12:V6.7
42477	42686	2009:L12:V7.1
42756	43282	2009:L12:V7.2
43285	44315	2009:L12:V7.3
45054	45565	2009:L12:V8.1
45569	47263	2010:L12:V2.0
47536	48064	2010:L12:V2.1
48484	49942	2010:L12:V2.2
50225	50955	2010:L12:V2.3
50958	52301	2010:L12:V2.4
52305	52853	2010:L12:V2.5
53074	53483	2010:L12:V2.7
53484	54045	2010:L12:V2.8
54049	54250	2010:L12:V2.9

versioning information were stored in the SeaTray output files. The `aafit` package (see Chapter 3) was used for event track reconstruction.

6.1.4 Livetime

In ANTARES the maximum length of a data run is constrained by a memory size limit of 2 GB. The run duration strongly depends on the detector conditions. Under quiet conditions, runs last, on average, near 2 hours, but this time could be several times larger when restrictive triggers are used in order to prevent a fast aging of the OMs during periods of high bioluminescence.

The effective livetime for each data run can be computed by multiplying the corresponding number of frames by the duration of each frame, which is a fixed quantity of $\sim$104 ms. These values are recorded for every run, together with detailed information on the environment

Description	Number of runs	Livetime [days]	Livetime [%]	Efficiency [%]
Final selection	7419	813	100	58
12-lines	6023	630	78	60
5-lines	1396	183	22	57
2010	2319	232	29	64
2009	1644	208	26	57
2008	1987	181	22	50
2007	1469	192	24	53

Table 6.2: Number of runs and livetime for different data taking periods. The last two rows show, respectively, the percentage of livetime that represents each sub-period considered and the data collection efficiency. The integrated livetime for all runs selected is 813 days, out of which only 22% were recorded with the 5-lines detector.

conditions, and stored in the data base, so that it is possible to calculate the corresponding livetime for any set of runs (see Table 6.2)[4].

The 7419 runs selected in this analysis have a total livetime of 813 days, out of which only 183 days correspond to data gathered with the 5-lines detector. Figure 6.4 shows the cumulative livetime as a function of the run number for the whole analyzed data set.

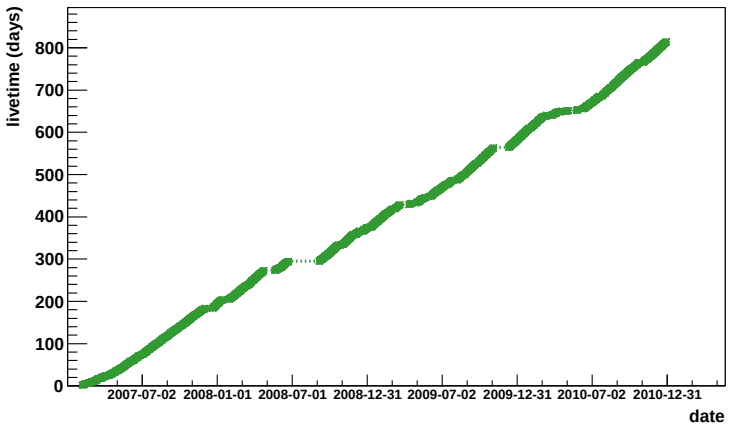

Figure 6.4: Cumulative days of livetime as a function of the run taking date for the whole data collection period discussed.

[4]Note that the 12-lines configuration is also used to refer to the periods where only 9, 10 or 11 lines were working, as such small changes in the detector configuration do not affect its performance significantly.

The data collection efficiency (livetime over collection time) is $\sim 60\%$ and is increasing every year. Loss of efficiency are due to several facts: sea operations, as for the deployment of new lines or their repairing; high bioluminescence activity periods, when more restrictive trigger criteria have to be applied; performing of calibration runs and sporadic losses caused by different problems with the detector.

6.2 Event selection

In order to select the final sample of neutrino candidate events we only accept tracks with reconstruction parameters

$$\theta < 90^\circ \quad \text{AND}$$
$$\sigma < 1^\circ \quad \text{AND}$$
$$\Lambda \geq -5.2,$$

where θ is the muon zenith angle.

To reduce as much as possible the background of down-going atmospheric muons only events reconstructed as upgoing ($\theta < 90^\circ$) are used. However, still a high number of down-going muons, which are mis-reconstructed as upgoing, stay. A cut on $\sigma < 1^\circ$ was adopted that rejects an important fraction of the mis-reconstructed muons while is highly efficient with signal neutrinos.

The quality of the reconstruction parameter is then used to further eliminate badly reconstructed tracks by imposing an appropriate cut on its value. It was found that requiring $\Lambda \geq -5.2$ is the optimal choice to achieve the best E_ν^{-2} signal discovery potential (see Chapter 7 Section 7.4). The Λ quality cut optimization was done in a blind manner by using right ascension scrambled data events.

Out of a total of $\sim 4 \times 10^8$ triggered events, only 3058 survived the three cuts previously described (see Table 6.3). Monte Carlo simulations indicate that the final sample has 14% atmospheric muon contamination (see Figure 6.8). The total expected background is 2766 $\pm$ 743 for 50% (30%) uncertainty on the atmospheric muon (neutrino) flux at Earth. These uncertainties have been estimated as described in [102] and [115]. The observed number of events in the final sample is therefore consistent with the predictions within the quoted uncertainties. The equatorial coordinates of the 3058 selected events are shown in the skymap

Selection level	Data	Atm. μ	Atm. ν
Trigger level	3.94×10^8	3.06×10^8	1.54×10^4
$\theta < 90^\circ$	6.08×10^7	2.98×10^7	1.24×10^4
$\theta < 90^\circ \,\&\, \sigma < 1^\circ$	3.90×10^7	1.57×10^7	8.35×10^3
$\theta < 90^\circ \,\&\, \sigma < 1^\circ \,\&\, \Lambda > -5.2$	3058	358	2408

Table 6.3: Number of data and background events remaining after applying each of the three final selection cuts adopted.

of Figure 6.5. For the convertion of the reconstructed track zenith and azimuth angles to right ascension and declination coordinates the library `ConvertCoordinates` from the ANTARES software repository was used.

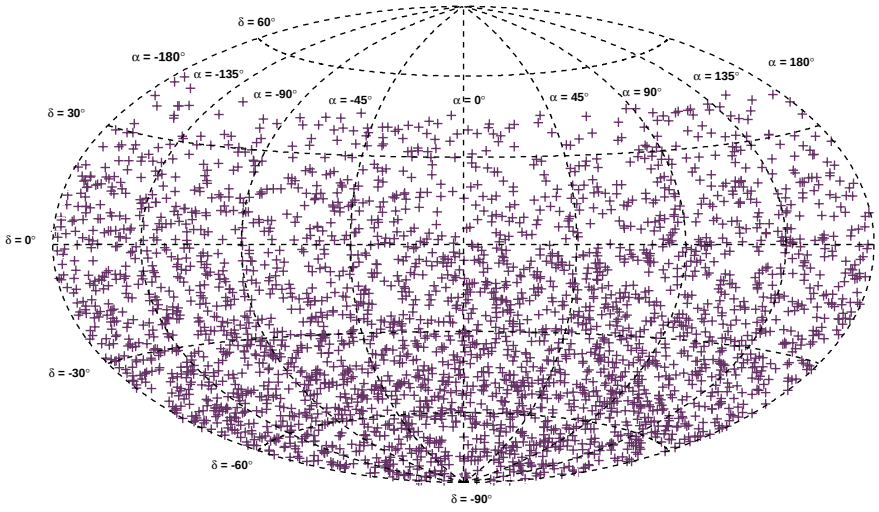

Figure 6.5: Skymap in equatorial showing the position of the 3058 neutrino candidate events selected.

6.3 Data and MC comparisons

Monte Carlo simulations try to reproduce all the processes involved in the physics analysis, from the generation of background events to the detector characterization. A good agreement

between MC and data is an indication of the good understanding of the involved physical processes and of the detector response.

In this analysis the first official version of the run-by-run scheme MC production[5] was used. This simulation takes into account the available information about the OMs counting rates to better reproduce the detector conditions happening during data taking. Atmospheric muon events were generated with the MUPAGE package in a number equivalent to 10% livetime of the corresponding data run. A total of 5×10^8 atmospheric neutrinos and anti-neutrinos (both down-going and up-going) in the $100 - 10^8$ GeV energy range were produced (per file) with GENHEN according to the Bartol model. In previous investigations [112] it was found that the MC and data distributions agree better when a smearing of 2 ns is applied to the arrival time of the hits. This behavior has been recently clarified as the result of an optimistic simulation of the OMs transit time spread, which is being corrected in updated MC productions. For what concerns the analysis being discussed here, this effect has been accounted for by applying a smearing of 2 ns to the arrival time of the hits. In the following plots, the black color is used to represent data events (with statistical errors), the green color for atmospheric muons, atmospheric neutrinos are shown in red and the total background (atm. ν + atm. μ, when plotted) is drawn in magenta. The ratio between the number of data and background events (in each bin) is shown in the bottom panels, with error bands calculated by adding on quadrature the uncertainties on the atmospheric muon (50%) and atmospheric neutrino (30%) fluxes [116].

In order to illustrate the run-by-run dependent MC generation scheme Figure 6.6 shows the run number distribution for data and MC events at the trigger level. In general data are underestimated, but the trends observed in data are well reproduced by the simulation. Two regions can be distinguished where expectations are clearly surpassed. This happens around run number 41000 and run number 48000, where high bioluminescence activity conditions (see Figure 6.3) were taking place. The reconstruction strategy does not work well in these situations, therefore the number of poorly reconstructed tracks rises. However, when requiring strict selection cuts, MC and data distributions match well.

Figure 6.7 shows data and MC zenith angle distributions for all (3N + T3) triggered events, for downgoing events reconstructed with $\Lambda > -5.2$ and $\sigma < 1^\circ$ and for events passing

[5] http://antares.in2p3.fr/internal/dokuwiki/doku.php?id=run by run

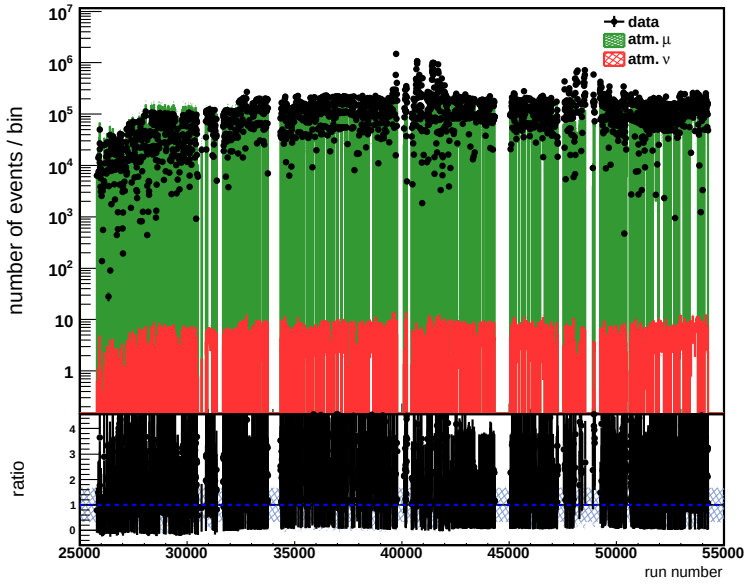

Figure 6.6: Number of (3N + T3) triggered events as a function of the run number. Simulations underestimate data moderately but reproduce the observed trends, except in periods of very high bioluminescence activity.

the final selection cuts. When requiring good quality tracks the agreement between data and MC is good in both the downgoing and the the upgoing region ($\theta < 90^\circ$).

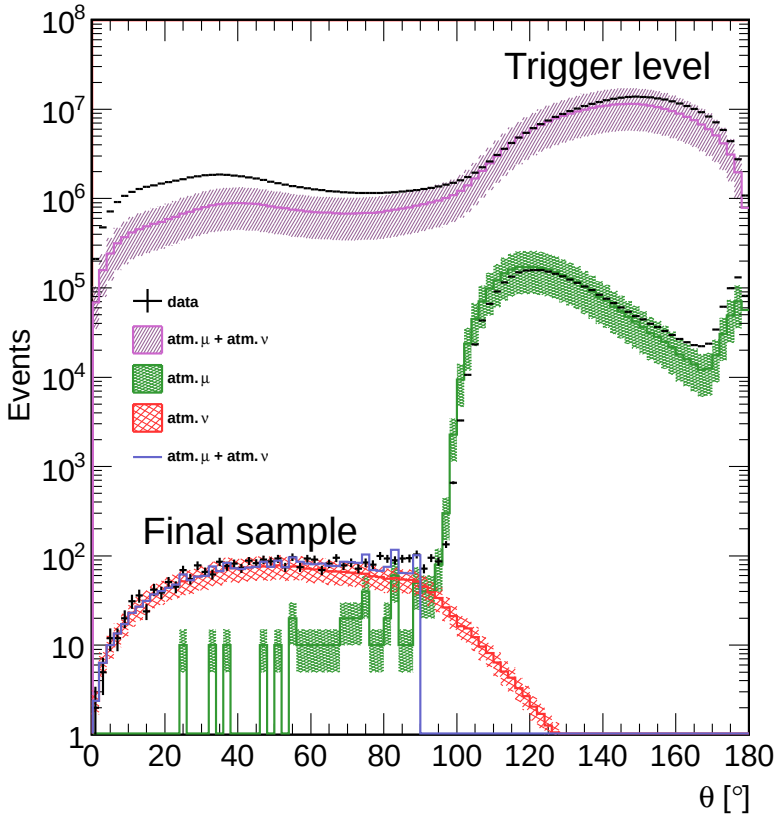

Figure 6.7: Reconstructed zenith angle distributions (of data, atmospheric muons and atmospheric neutrinos) at trigger level, for $\Lambda > -5.2 \,\&\, \sigma < 1^\circ$ events and for the 3058 events that survive the final selection cuts.

The cumulative distribution of the quality of the reconstruction parameter, Λ, is shown in Figure 6.8 for data and MC events reconstructed with $\theta < 90^\circ$ and $\sigma < 1^\circ$. The agreement in the parameter region defined by $\Lambda > -5.2$ is well within the 30% systematic uncertainty on the neutrino flux. Figure 6.9 shows the angular error estimate for both data and MC upgoing events reconstructed with $\Lambda > -5.2$. The MC expectations agree, as well, with data within the quoted uncertainties in the final quality cuts selection region. In Figure 6.10 the azimuth angle, declination angle, number of hits and number of lines used in the fit distributions are

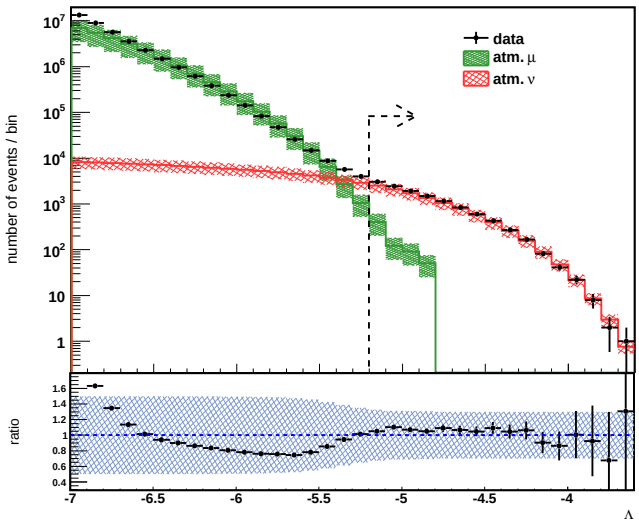

Figure 6.8: Cumulative distributions of the quality of the reconstruction parameter for data, atmospheric muon and atmospheric neutrino events reconstructed as up-going and with values of the angular error estimate smaller than 1 degree. The vertical dashed line with an arrow indicates where the final selection cut is applied, i.e. $\Lambda > -5.2$.

shown for data and MC events passing the final quality cuts.

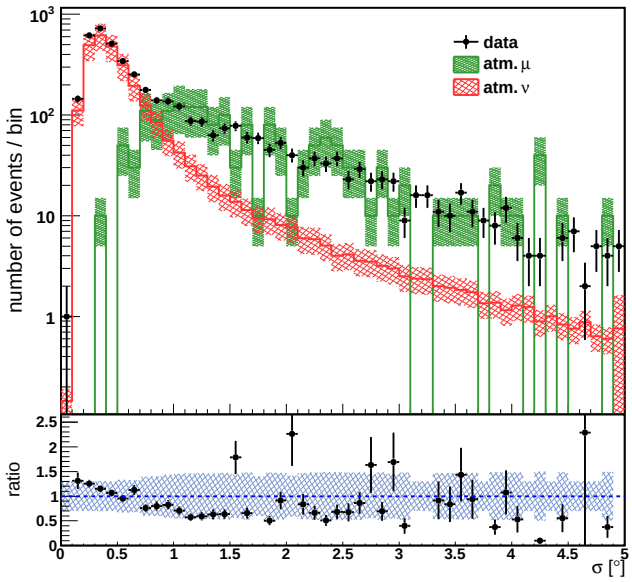

Figure 6.9: Distribution of the angular error estimate for data and background (atm. μ + atm. ν) events reconstructed as up-going and with $\Lambda > -5.2$. The agreement below $\sigma < 1^\circ$ is within the uncertainties.

6.4 Detector performance

The effective area and the angular resolution, which are the main parameters that describe the ANTARES response to a point-source search, are studied at the final quality cuts level using simulations. The angular resolution, which is defined as the median value of the angular difference between the reconstructed muon trajectory and the generated neutrino direction, is the crucial parameter for a neutrino telescope to make astronomy. For a neutrino signal proportional to E_ν^{-2} it is $0.46^\circ \pm 0.10^\circ$, being 80% of the events reconstructed within one degree off the simulated neutrino track. When considering only the 12-lines detector configuration, the angular resolution is $0.42^\circ \pm 0.10^\circ$, while for the period when there was only 5 lines installed it is $0.58^\circ \pm 0.10^\circ$. The uncertainty on this magnitude was estimated by varying the hit time resolution in the simulation [112]. Figure 6.11 (left) shows, for the 12-Lines period,

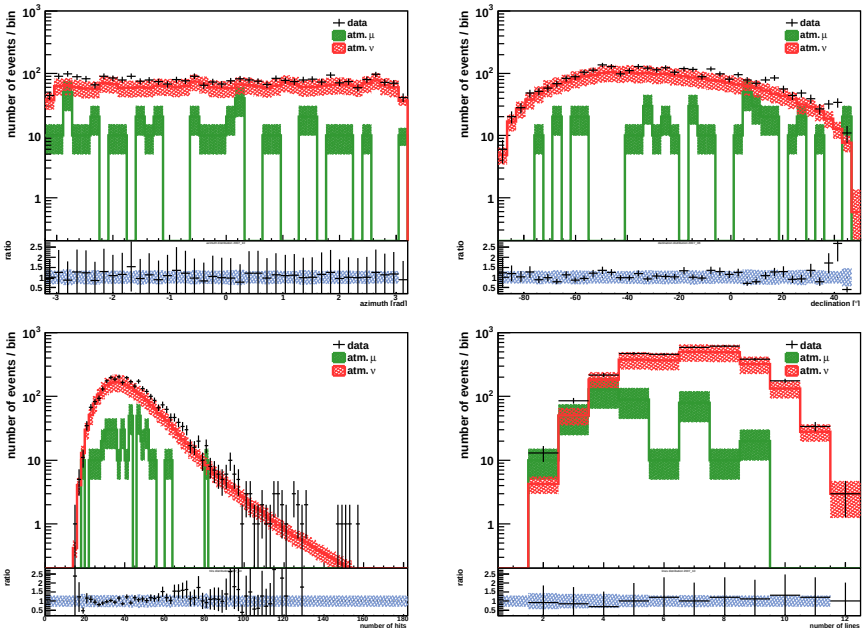

Figure 6.10: Distributions of the azimuth angle, declination angle, number of hits and number of lines used in the track fit (top left - bottom right) for both data and MC events at the final selection level ($\theta < 90^\circ \quad \& \quad \sigma < 1^\circ \quad \& \quad \Lambda > -5.2$).

the cumulative distribution of the angular difference for different neutrino energy regions and spectra. The median value of angular resolution is shown as well (right) for both detector configuration periods as a function of the true neutrino energy.

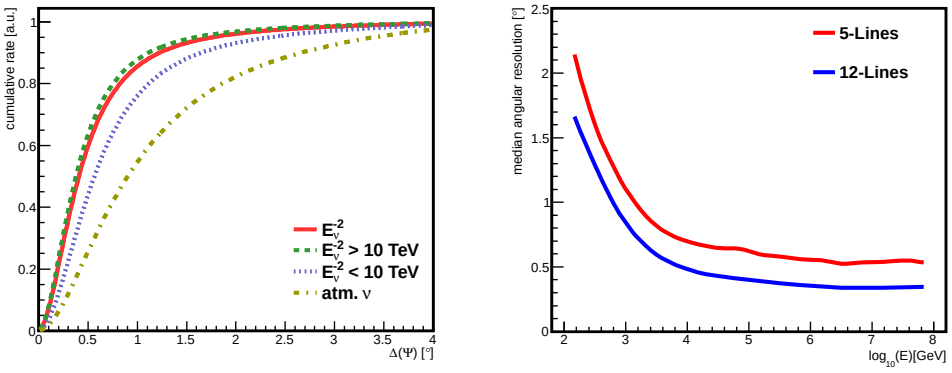

Figure 6.11: Cumulative distribution of the angular error between the reconstructed muon track and the generated neutrino direction for different neutrino energy ranges and spectra (left). Median angular resolution as a function of the true neutrino energy (right).

The effective area represents the equivalent surface of a 100% efficient detector. This parameter, which allows us to calculate signal event rates, depends on the neutrino interaction cross section, the neutrino absorption through the Earth (see Chapter 3) and the muon detection and selection efficiency:

$$A_{\nu}^{eff} = \sum_{i=1}^{N_{\Delta E}} \frac{W_{\mathrm{gen}_i}}{F_{\Delta E}\, t_{\mathrm{gen}} I_{\theta}\, I_E\, E_i^{-2}} \tag{6.1}$$

where

$$F_{\Delta E} = \frac{\int_{\Delta E} E^{-2} dE}{\int_{E_{min}}^{E_{max}} E^{-2} dE} \tag{6.2}$$

and where $N_{\Delta E}$ is the number of reconstructed and selected events in ΔE and $F_{\Delta E}$ is the fraction of simulated events in the ΔE interval. In Figure 6.12 the effective area is shown as a function of the true neutrino energy for a flux of $\nu + \bar{\nu}$ and in three different declination bands. It increases steadily with the energy because the increasing of the neutrino interaction cross section and of the muon range and light yield. Above PeV energies the trend turns over

since the probability for a neutrino to be absorbed by the Earth becomes dominant for events arriving from higher declinations.

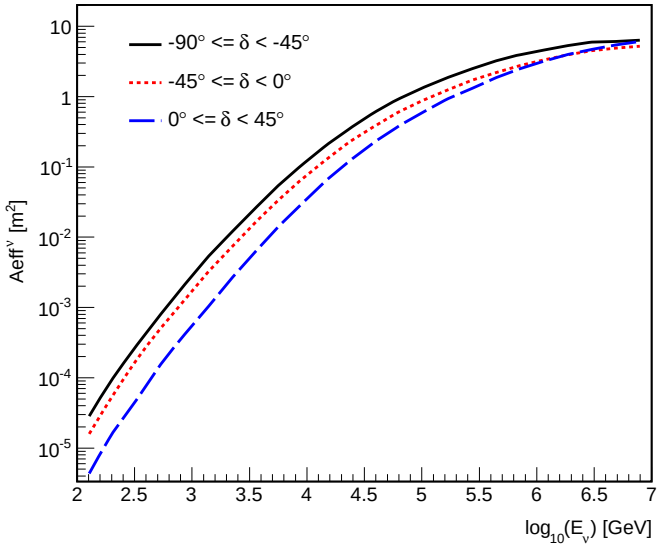

Figure 6.12: Effective area in three declination bands as a function of the neutrino energy for the final selection cuts and for a signal spectrum proportional to E^{-2}.

7

Methods to search for cosmic neutrinos sources

The basis of a search for cosmic neutrinos sources are discussed in this chapter. Unbinned maximum likelihood methods, incorporating spatial and spectral information, are used to estimate the contributions of signal and background in data. A ratio likelihood test determines the significance of the search. Accounting for systematic uncertainties, median upper limits and the flux for discovery are calculated.

7.1 Time-integrated search for point sources

The main motivation for constructing a neutrino telescope is the detection of high energy neutrinos of extraterrestrial origin and the identification of their emission places. The list of candidate sources, as discussed in Chapter 1, includes SNRs, micro-quasars and AGNs. These are also the most plausible scenarios for acceleration of CRs above GeV energies. The discovery of a cosmic neutrino source would, therefore, provide valuable information regarding the origin of CRs and settle the question of the hadronic versus leptonic mechanism as responsible for high energy gamma-ray emissions observed from several sources.

This work focuses on point-like sources of astrophysical neutrinos. It uses four years of data from the ANTARES telescope to perform a time-integrated search over the selected 3058 neutrino candidates, which are described as a set of events appearing spread over the sky with some reconstructed direction and energy. Simulations indicate that this sample consists mainly

on atmospheric neutrinos, with 14% atmospheric muon contamination. These backgrounds should appear uniformly distributed inside a small declination band. Therefore, the presence of a rare accumulation of events within a restricted region (making up a cluster) could indicate the existence of the signal we are searching for. On the other hand, because the atmospheric neutrino flux has a softer energy spectrum than the one expected for cosmic neutrinos, the energy distribution of the events represents an additional piece of information to further separate signal from background. Unbinned clustering techniques, by means of statistical functions, allow us to incorporate all this information in the search. Two unbinned algorithms have been applied in this analysis, which are described below.

7.2 Clustering methods

Clustering analysis provide tools to identify and separate the different groups of elements that may exist in a data set. Among the different clustering techniques, those called "mixture models" assume the data to follow a global density function made up by the sum of different density components. Following this approach, we model our data as the two component mixture of signal and background expressed by the likelihood function

$$\mathcal{L} = \prod_{i=1}^{N} \left[\frac{n_s}{N} \mathcal{S}_i + (1 - \frac{n_s}{N}) \mathcal{B}_i \right], \tag{7.1}$$

where $\mathcal{S}_i$ and $\mathcal{B}_i$ represent, respectively, the signal and background probability density functions (PDFs), N is the total number of events in the data and n_s is the number of signal events. The relative contribution of each component can be estimated by maximizing the likelihood with respect to the unknown parameters of the model.

7.2.1 The Expectation-Maximization algorithm

The Expectation-Maximization (E-M) algorithm [117] is an iterative approach to obtain maximum likelihood estimates of the unknown parameters in mixture problems. In the E-M algorithm the observations given in the data are thought to form a set of incomplete data vectors. The unknown information is whether or not an event belongs to the background or the signal distributions. A class indicator vector or weight is added to each event taking the

value 0 for background and 1 for signal. The observed events with the associated weights form a complete data set with a complete likelihood.

The optimisation procedure in the E-M algorithm consists of two steps. In the *Expectation* step, the likelihood logarithm is evaluated using an initial set of parameter estimates (including the associated weights) to describe the unknown source properties. In the *Maximization* step, a new set of parameters is found that maximizes the complete data log-likelihood. A new likelihood expectation value is calculated using the outcoming parameters from the previous iteration. The entire procedure is repeated until the model parameters converge, leading to the maximization of the likelihood of the incomplete data set.

The E-M method has been adapted to the problem of the search for cosmic neutrino sources as it is described in [118]. We use such implementation here which, unlike other unbinned methods being applied to this problem, does not depend on the exact point spread function of the detector, a feature particularly interesting when dealing with sources whose spatial properties are unknown.

7.2.2 Numerical maximum likelihood method

The accuracy on the reconstructed track direction, as given by the angular error estimate, varies from event to event. This information can be incorporated into the likelihood description in order to improve the signal/noise separation. In contrast with the E-M method, this second algorithm[1] introduces such additional piece of information in the signal PDF description and maximizes the log-likelihood function numerically using the MIGRAD subroutine of the `MINUIT` package [119] from `ROOT`.

In Figure 7.1 the correlation between the angular uncertainty estimate and the angular difference between the reconstructed muon direction and the trajectory of the generated neutrino is shown for a set of σ ranges. Although the uncertainty estimated from the covariance matrix of the reconstruction algorithm does not offer a very precise description of the true error it is very efficient to discriminate misreconstructed muon events (see Chapter 6).

[1] From now on this method will be referred to as the NML method.

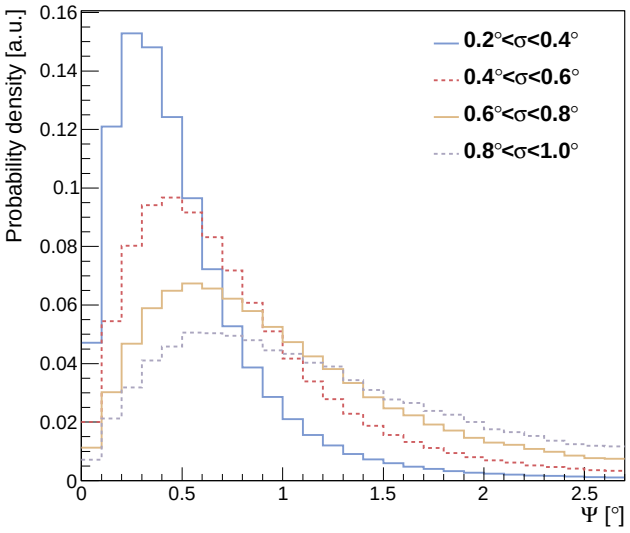

Figure 7.1: Angular difference Ψ between the generated neutrino track and the reconstructed muon direction for different ranges of the angular error estimate σ_i.

7.3 Expressions for the likelihood

The probability density functions for the signal and background distributions include two terms; the first one describes the spatial properties of the events and the second one characterizes their energy distribution.

Background PDF: Because the Earth's rotation and the large exposure time, the detector response is uniform in right ascension and the background distribution is only dependent on declination. Considering that a possible signal is small in comparison, all the events in the data are assumed to be background. A fit to the sine of the declination distribution from real data (Figure 7.2) is used to parameterize the background density function $\Psi_i(\delta_i)$ minimizing the statistic fluctuations.

The energy term $\mathcal{E}(N_i^{hits}|Atm)$ describes the probability for finding an atmospheric neutrino or an atmospheric muon reconstructed using N_i^{hits} number of hits. The global background PDF is given by the product:

$$\mathcal{B}_i = \Psi_i(\delta_i) \cdot \mathcal{E}(N_i^{hits}|Atm). \tag{7.2}$$

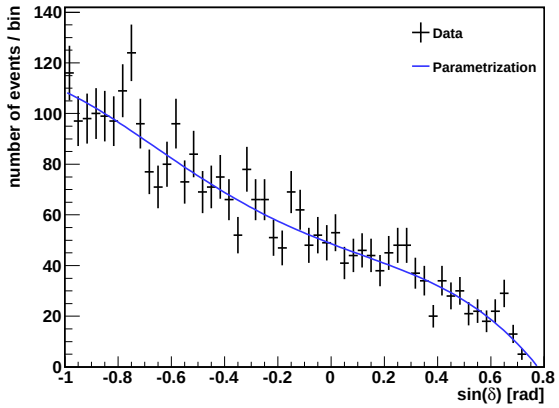

Figure 7.2: Distribution of the sin(δ) for data events at the final selection level (dots). A five degree polynomial function is used for the background PDF characterization (solid line).

Signal PDF: The probability for an event with reconstructed direction $\overrightarrow{x_i} = (\alpha_i, \delta i)$, to be produced by a source located at $\overrightarrow{x_s} = (\alpha_s, \delta s)$ is modeled as a circular two dimensional Gaussian:

$$\Psi(\overrightarrow{x_i}; \sigma_i) = \frac{1}{2\pi\sigma_i^2} \cdot e^{-\frac{|\overrightarrow{x_i} - \overrightarrow{x_s}|^2}{2\sigma_i^2}}, \tag{7.3}$$

where σ_i, i.e. the angular error estimated for each event individually, introduces the dependence on the detector resolution. The approach is different in the E-M likelihood implementation: elliptical Gaussians are used instead whose widths are independent variables ($\sigma_\alpha \neq \sigma_\delta$) with changing values during the maximization process. In this sense, the E-M method has the capability to adapt itself to the (unknown) spatial properties of the source.

The number of hits used in the track reconstruction provides a robust estimator of the muon track energy (see Figure 7.3). Considering this information in the likelihood function was shown to increase about a 25% factor the signal/noise discrimination power of the search. The full signal PDF is, then, given by the product of the probabilities:

$$\mathcal{S}_i = \Psi(\overrightarrow{x}_i) \cdot \mathcal{E}(E_i|\gamma = 2.0), \tag{7.4}$$

where $\mathcal{E}(N_i^{hits}|\gamma = 2.0)$ describes the probability for an event to be reconstructed using N_i^{hits} number of hits if being emitted from a source with an E^{-2} energy spectrum. The

distributions of the number of hits for data and an E^{-2} weighted simulations (Figure 7.4) are used to describe the energy PDFs for background and signal respectively.

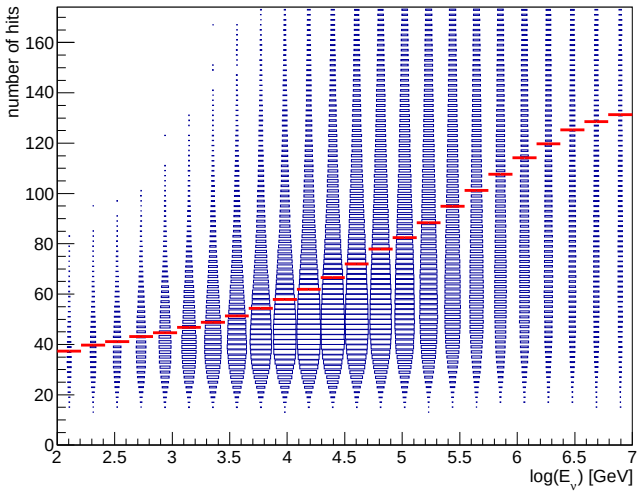

Figure 7.3: Distribution of the number of hits versus the true neutrino energy for a flux $dN/dE \propto E^{-2}$. The red marks indicate the distribution profile.

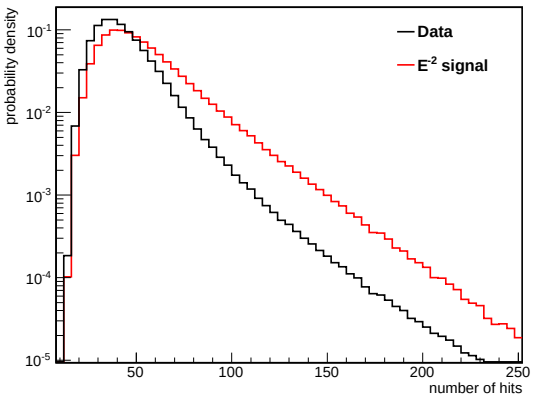

Figure 7.4: Probability density functions used for the background and signal energy densities, which are derived from the normalized distributions of the number of hits used in the track fit.

7.4 Test statistic and hypothesis testing

A criterion is needed to decide whether a point source of neutrinos exists in the data or not, i.e., to determine the compatibility of the data with two hypothesis:

- H_0; Only background events are present in our data sample (the null hypothesis).
- H_1; Additionally to the background noise made up by the atmospheric muon and atmospheric neutrino events, a source of neutrinos, with some strength and energy spectrum, contributes to our data (the alternative hypothesis).

In statistical hypothesis testing, the model discriminator is usually specified in terms of a test statistic, which can be in principle, any function of the data. The ratio of the probabilities for the data ($\overrightarrow{x}$) under the assumption that H_1 and, respectively, H_0 is the true hypothesis (Equation 7.5), was chosen as statistical test.

$$\lambda = \frac{\mathcal{L}(\overrightarrow{x}|H_1)}{\mathcal{L}(\overrightarrow{x}|H_0)}. \tag{7.5}$$

The election is justified on the basis of the Neyman-Pearson lemma [120] which demonstrates that, among all competitors, the ratio likelihood test is the most powerful test when H_0 and H_1 are completely defined (i.e., they have not unknown parameters). The test is calculated for the best fit estimates of the free parameters in the H_1 model (the only background model H_0 is assumed to be completely known) which are obtained by maximizing [2] the likelihood function:

$$\lambda = -\log\left[\frac{\mathcal{L}(H_1)}{\mathcal{L}(H_0)}\right] = \sum_{i=1}^{N} \log\left[\frac{n_s}{N}\mathcal{S}_i + \left(1 - \frac{n_s}{N}\right) B_i\right] - \sum_{i=1}^{N} \log\left[B_i\right]. \tag{7.6}$$

The value of λ indicates whether the data is more compatible with H_0 or with H_1. In Figure 7.5 distributions of the test statistics for the H_0 and H_1 models are shown with illustrative purposes. The rejection region, ω, defines a set of values where is unlikely to find λ when H_0 is true; if λ lies within the rejection region, the hypothesis H_0 is "rejected" in favour of H_1. Higher values of the test statistic indicate thus a larger deviation from the only background expectations.

[2] In reality, the equivalent quantity $-\log(\mathcal{L})$ is minimized.

$$\begin{cases} 1 - CL = P(\lambda \in \omega \mid H_0) \\ power = P(\lambda \in \omega \mid H_1) \end{cases} \tag{7.7}$$

It may happen that λ is contained in the rejection region, even though H_0 is true. In this case H_0 will be wrongly rejected, and a false discovery claimed. The probability for this to happen is called the significance level of the test (1-CL). Alternatively, the probability to reject H_0 when H_1 is indeed the correct model, is called the "power" of the test. Assuming that the null hypothesis is true, a good test statistic will have low significance level (small chance of incorrectly claim a fake discovery) and high discovery power (small chance for missing a discovery).

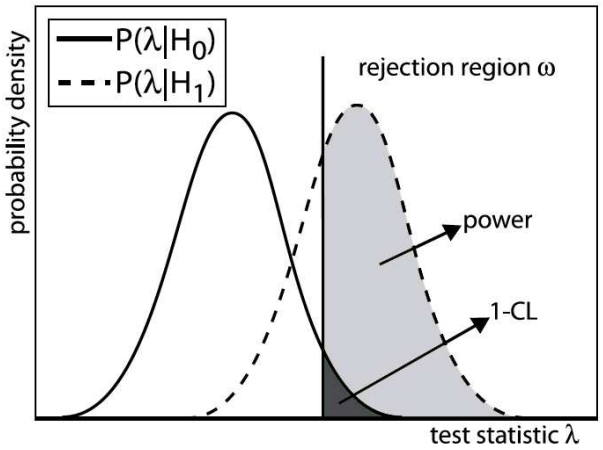

Figure 7.5: Illustrative distributions of the test statistic for the null (H_0) and the signal (H_1) hypothesis. The rejection region (at right from the vertical line) defines a set of λ values which are unlikely to be produced by the background. The shadowed areas are related to the CL and power of the test.

7.5 Significance and upper limits

The significance of the analysis is determined by comparing the value of the test statistic observed from data (λ_{obs}) with the λ distribution of only-background pseudo-experiments using events which have been scrambled in right ascension (see Section 7.6).

The result of an observation would be statistically significant when, according to a pre-defined threshold probability, it is very unlikely to occur by chance as a background fluctuation.

A common choice in high energy physics is to require a false discovery probability of 5.7×10^{-7}, which is equivalent to 5σ expressed in terms of number of deviations from the mean value of a Gaussian distribution. A discovery would be claimed only when, assuming the null hypothesis to be true, the measured *p-value*, i.e., the probability to find a test statistic at least as extreme as the actually observed value, has (at least) a 5σ significance.

Figure 7.6 shows, for the two unbinned methods previously introduced, the distributions of the test statistic obtained from 10^4 only background trials, and from 10^4 pseudo-experiments where signal events are injected from a source located at $\delta = -70^\circ$ with energy spectrum proportional to E^{-2}. Because the limited number of pseudo-experiments simulated, the λ_c critical value that corresponds to the 5σ threshold probability was extrapolated, following the Wilk's theorem [121], from a χ^2 fit to the only background distribution tail. This approximation is necessary because of the high computational resources needed to simulate the 10^7 pseudo-experiments required to reach the 5σ level.

When the result of an observation is a p-value less significant than the 5σ pre-defined threshold, a discovery can not be claimed. In this case we would like to put constraints on the neutrino flux using our observable λ. Following the Neyman [122] frequentist method for the construction of confidence intervals we can calculate an upper limit $P(\lambda > \lambda_1|\mu) = 1-CL$ on the source strength μ it would be required to find, in 90% of the experiments[3], a value of the test statistic equal or higher than the observed one. In this calculation pseudo-experiments where up to 30 signal events are injected into the data set to simulate a fake source are used considering that, for a certain μ value, the probability to observe λ is

$$P(\lambda|\mu) = \sum_{i=0}^{n_s=30} \left(P(\lambda|n_s) \times P(n_s|\mu)\right), \tag{7.8}$$

where $P(\lambda|n_s)$ is the probability to obtain λ having n_s signal events and $P(n_s|\mu)$ is the Poisson probability of finding n_s events for a Poisson mean signal μ.

In this work we also use the Feldman and Cousins approach [123] for limits calculation, which is based on the ordering principle defined by the ratio:

$$R = \frac{P(\lambda|\mu)}{P(\lambda|\mu_{best})}, \tag{7.9}$$

[3]For setting limits on physics parameters a 90% CL is generally used.

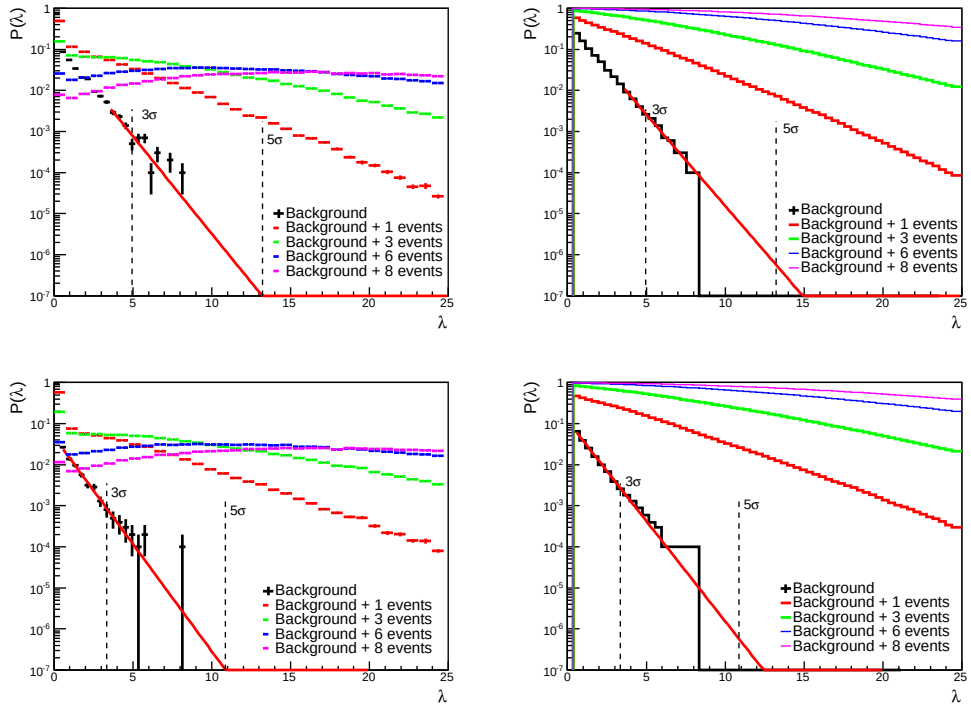

Figure 7.6: Lineal (left) and cumulative (right) distributions of the test statistic from 10^4 only background pseudo-experiments and from 10^4 scrambled sky maps where some signal events are injected from a source simulated at $\delta = -70^\circ$ and with an E^{-2} energy spectrum. The likelihood ratios are shown for the E-M algorithm (top) and the NML method (bottom).

where $P(\lambda|\mu_{best})$ is the maximum value of $P(\lambda|\mu)$ for a given λ. Confidence belts are built by adding values of λ to the acceptance region[4] for a given μ in decreasing order of R, until the sum $P(\lambda|\mu)$ meets or exceeds the desired CL. In order to easily construct our Feldman and Cousins confidence belts we have applied to the test statistic a transformation $\lambda' = \log_{10}(\lambda + C)$. Figure 7.7 shows an example of the resulting 90% CL Feldman and Cousins confidence belt. The edges where a vertical line drawn at a given λ' value intersect the acceptance region form the 90% CL on μ. The highest and lowest values of μ are, respectively, the 90% CL upper and lower limits.

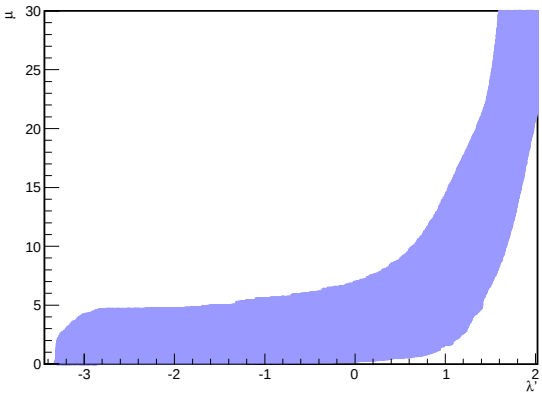

Figure 7.7: Feldman and Cousins 90% CL confidence interval for E^{-2} signals simulated from a source at $\delta = -70°$

The magnitude μ can be translated into a neutrino flux on which to put limits. This is done by means of the acceptance $A(\delta_\nu)$, which is defined as the constant of proportionality between the flux normalization ϕ and the expected number of events in the source direction and can be expressed in terms of the effective area (see Chapter 6) as

$$A(\delta_\nu) = \phi^{-1} \int\int dt dE_\nu A_\nu^{\text{eff}}(E_\nu, \delta_\nu) \frac{dN_\nu}{dE_\nu dt}. \tag{7.10}$$

In this work cosmic sources are assumed to emit a flux of neutrinos of the form:

$$\frac{dN_\nu}{dE_\nu dt dS} = \phi \times \left(\frac{E_\nu}{\text{GeV}}\right)^{-2} \text{GeV}^{-1}\text{cm}^{-2}\text{s}^{-1}, \tag{7.11}$$

[4]The acceptance region defines an interval $[\lambda_1, \lambda_2]$ such that $P(x \in [\lambda_1, \lambda_2]|\mu) = CL$.

therefore the neutrino flux is completely defined by the normalization factor ϕ. The acceptance is shown in Figure 7.8 at the final quality cuts level. Reading this plot we can see that for a point-like source placed at declination $-90°(0°)$ and producing a neutrino flux of $10^{-7}(E_\nu/GeV)^{-2}$ $\mathrm{GeV}^{-1}\mathrm{cm}^{-2}\mathrm{s}^{-1}$ a total of 8.8 (4.8) neutrino candidates would be detected and selected in this analysis.

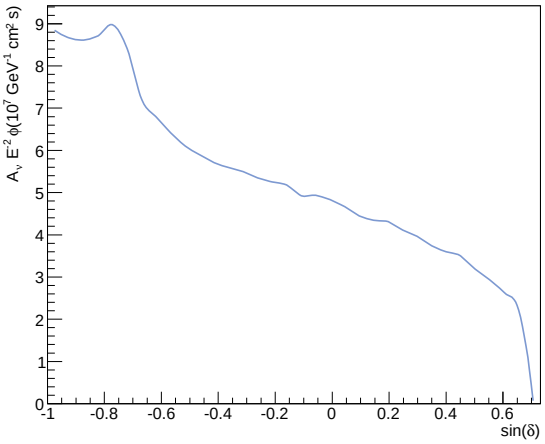

Figure 7.8: Detector acceptance for a neutrino flux of $10^{-7} \times (E_\nu/GeV)^{-2}$ $\mathrm{GeV}^{-1}\mathrm{cm}^{-2}\mathrm{s}^{-1}$ emitted by a point source with a $\propto E^{-2}$ energy spectrum.

The search sensitivity, defined as the 90% CL median upper limit from background only pseudo-experiments, is shown in Figure 7.9 as a function of the source declination expressed as the mean number of signal events and converted to neutrino flux. Figure **??** shows the discovery flux, i.e. the flux required to have 50% chance to find a p-value lower than or equal to 5.7×10^{-7}, as a function of the source declination. It is also shown in terms of the mean number of signal events and at the 3σ CL ($P(\lambda \geq \lambda_c|\mu) = 2.7 \times 10^{-3}$), which is usually interpreted as an evidence of the the signal existence. These results show that when applying the NML method a $\sim 20\%$ lower flux is required to detect a source than when the E-M algorithm is used. This can be understood on the basis of the Neyman-Pearson lemma because the larger number of "nuisance parameters" (the width of the Gaussian pdf) in the E-M likelihood implementation.

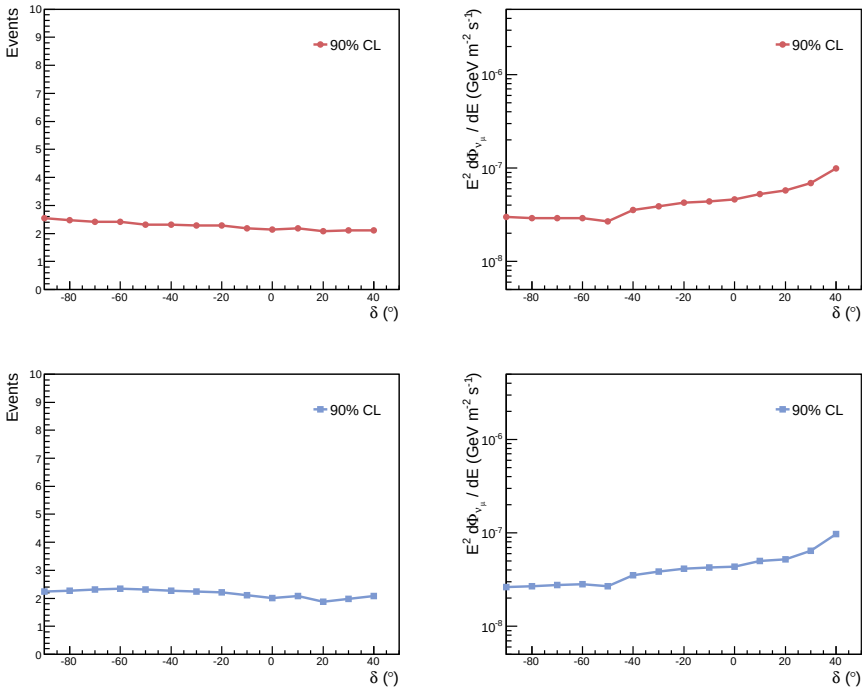

Figure 7.9: Search sensitivity (90% CL) expressed in terms of the number of signal events (left) and the source flux intensity (right) for the E-M algorithm (top) and the NML method (bottom).

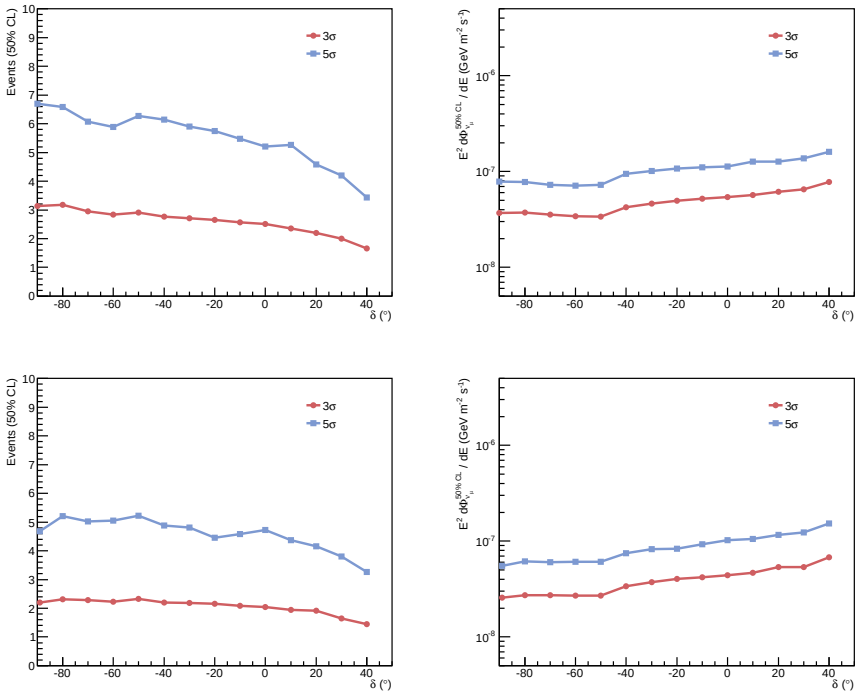

Figure 7.10: Number of signal events (left) and flux (right) for discovery versus the source declination for the two search methods introduced (upper plot is for the E-M algorithm and bottom plot is for the NML method). The sources are simulated with an energy spectrum proportional to E^{-2}.

7.6 Pseudo-experiments simulation

Because the lack of prior knowledge of the λ distributions, the statistical interpretation of the search relies on pseudo-experiments. These are reproductions of the measurements in which fake sky maps (containing events in same number of the data sample) are generated to perform statistical tests.

For placing background events in a fake equatorial sky map, the declination coordinate is sampled from the fit to the data distribution shown in Figure 7.2, while the right ascension is thrown uniformly. For signal events instead, the angular distance β to the source location (α_s, δ_s) is sampled from the distribution of the error on the neutrino direction. Next, a vector $\overrightarrow{v} = [\sin(\beta)\sin(\psi), \sin(\beta)\cos(\psi), cos(\beta)]$ is generated, where the angle ψ is randomly chosen. Then, $\overrightarrow{v}$ is rotated 90$-\delta_s$ degrees over the y-axis and α_s degrees over the z-axis. The celestial coordinates of the event are the spherical coordinates describing the vector: $(\delta, \alpha) = (\sin^{-1}(v_z), \mathrm{atan}(\mathrm{v_y}/\mathrm{v_x}))$.

To fully characterize an event we still need to assign a number of hits and a value for the angular error estimate. Once more, while for background events these values are sampled from data distributions, for signal events it is required the use of MC simulations. In the latter case, the distributions of the angular error on the neutrino direction, the number of hits used in the reconstruction and the angular uncertainty estimate are sampled from 3D-Histograms constructed over declination bands of ten degrees. This procedure ensures that possible correlations between the distributions used are taken into account.

7.6.1 Systematic errors

Systematic uncertainties estimated in previous studies [124] [112] are accounted for in the limits and the sensitivity calculations by modifying the fake signal events injection during the pseudo-experiments generation. This is done assuming the uncertainties to be described by Gaussian distributions.

In order to account for the uncertainty on the angular resolution of the detector a smearing factor is drawn from a Gaussian function of $\mu = 1$ and $\sigma_\alpha = 0.15$. The angular distance at which an event is drawn from the simulated source is then multiplied by this number. When degrading or improving the detector PSF in each pseudo-experiment, the net effect is a deterioration of the search sensitivity.

Type	Systematic error
angular resolution	$\sigma_\alpha = 0.15$
absolute pointing	$\sigma_\theta = 0.06$ and $\sigma_\phi = 0.13$
number of hits	$\sigma_{N_{hits}} = 0.10$
detector efficiency	$\sigma_\mu = 0.15$

Table 7.1: Summary table of the systematic uncertainties we account for in the sensitivity and upper limits computation. These uncertainties were estimated as described in [124] [112].

The effect of the systematic uncertainty on the absolute pointing of the detector is implemented in a similar way. For each pseudo-experiment, the zenith and azimuth angles of the signal events are smeared with scale factors generated from Gaussian distributions of $\sigma_\theta = 0.06$ and $\sigma_\phi = 0.13$ respectively. Because this magnitude is known very precisely, its influence in the results is almost negligible.

To account for the uncertainties in the number of hits with which an event is reconstructed, the value sampled from the number of hits distribution is multiplied by a value randomly generated from a Gaussian of $\mu = 1$ and $\sigma_{N_{hits}} = 0.10$.

For accounting the systematic uncertainty on the detector efficiency ($\sigma_\mu = 0.15$) Equation 7.8 is convoluted with a Gaussian $\mathcal{G}$ as given by:

$$P(\lambda| < \mu >) = \sum_{n_s=1}^{N} P(\lambda|n_s) \int P(n_s|\mu) \cdot \mathcal{G}(\mu| < \mu >, \sigma_\mu) d\mu. \tag{7.12}$$

This is the only systematic not implemented in the pseudo-experiment generation. Table 7.1 summarizes the values of the different systematics uncertainties we have discussed.

7.7 Extended sources and sources with an exponential cutoff spectra

Sources which are spatially extended up to several degrees have been measured with good precision by high energy gamma-ray telescopes. Indeed, in [125] it is discussed how accounting for the correct source extension increases the significance of the observation. Therefore, in order to be more sensitive to an emission from an extended region of width σ_s, we convolute the signal PDF in the NML method with another 2D-Gaussian of equivalent broadness, resulting

on a wider 2D-Gaussian PSF of width $\sqrt{\sigma_i^2 + \sigma_s^2}$. Because the E-M algorithm modifies the width of the Gaussian PDF every iteration, trying to match the correct source extension and yielding $(\hat{\sigma_\alpha}, \hat{\sigma_\delta})$ estimates (see Figure 7.11), it does not requires such modification.

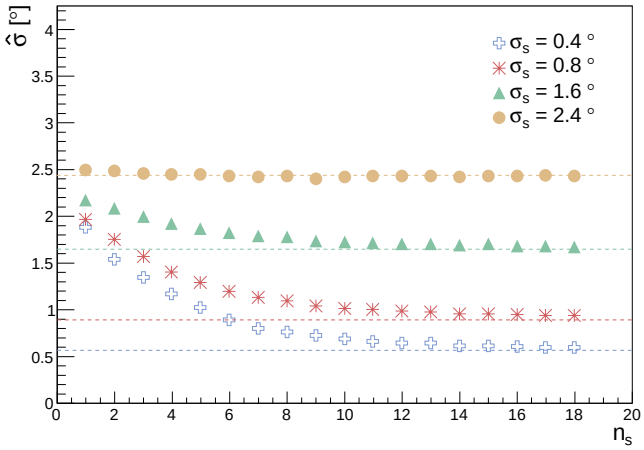

Figure 7.11: Median value of the source extension fitted by the E-M algorithm ($\hat{\sigma}$) versus the number of signal events injected, from pseudo-experiments where Gaussian shape sources of σ extension are simulated.

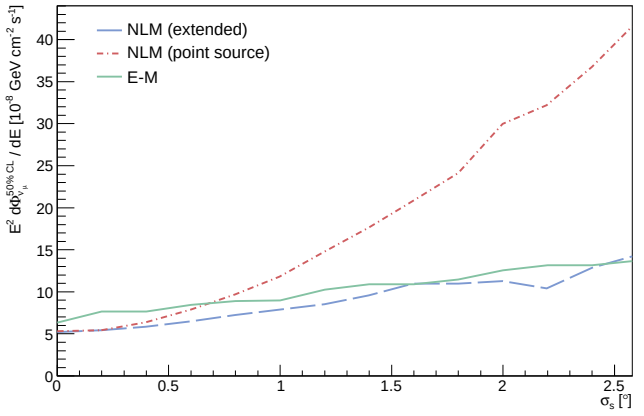

Figure 7.12: Discovery flux as a function of the source extension for a source located at $\delta = -70°$. This is shown for the E-M algorithm and for the NML method accounting for the source extension (dashed line) and assuming the point source hypothesis (dash-dot line).

In Figure 7.12 the discovery flux required to have 50% chance to detect a source with 3σ significance is shown as a function of the source extension. Curves are drawn for the E-M method, and for the NML method accounting for the correct extension of the source and when a point-like source model is instead assumed. For a source with 1° extension the flux needed for discovery when the point source hypothesis is considered is $\sim$1.5 times higher than the flux required when the true extension of the source is taken into account in the NML method likelihood function. The plot also shows how the E-M algorithm becomes competitive as the source extension increases.

In addition, we have studied the response of the NML search method to sources with different exponential cutoffs (Equation 7.13) in the energy spectrum. This analysis was done considering six different cutoff positions: starting at 100 GeV and through steps of one decade in energy. The results obtained are shown in Figure **??**, where neutrino flux and the number of signal events required to detect a source at $\delta = -60^\circ, 0^\circ, 30^\circ$ with 3σ and 5σ significance are presented as a function of the energy cutoff E_{cut}.

$$\frac{dN_\nu}{dE_\nu dt dS} = \phi \times \left(\frac{E_\nu}{\mathrm{GeV}}\right)^{-2} \times e^{-E/E_{cut}} \ \mathrm{GeV}^{-1}\mathrm{cm}^{-2}\mathrm{s}^{-1}, \tag{7.13}$$

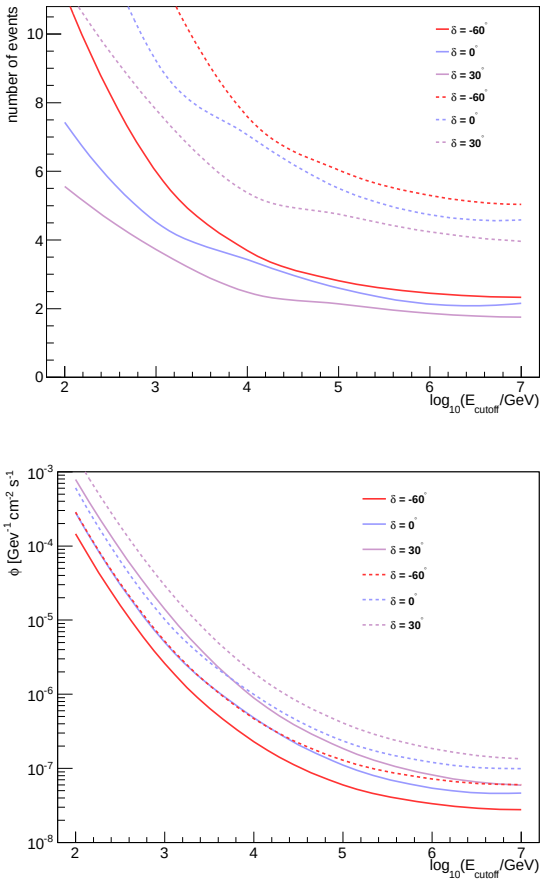

Figure 7.13: Discovery power at 3σ CL (solid lines) and at 5σ CL (dashed lines) as a function of the energy cutoff (E_{cutoff}) for a flux in the form of 7.13 expressed in terms of the number of events (left) and flux (right) needed for having 50% chance of discovery. This is show for three different declinations.

8

Results from cosmic neutrino searches

In this chapter we present the results obtained in the time-integrated searches for cosmic neutrino sources we have performed on the unblinded sample from ANTARES data with 813 days of livetime. Not having found any statistically significant deviation from the background hypothesis we provide p-values and 90% CL upper-limits to the E_ν^{-2} flux for sources in both the Southern and Northern Hemispheres. Assuming flux models of astrophysical neutrino emission we have also calculated upper limits for two high energy gamma-ray sources. The results from a search in correlation with gravitational lensing objects are summarized at the end.

8.1 Description of the searches

Using the final sample of 3058 neutrino candidate events two different searches for point sources of neutrinos have been conducted: The "full-sky" search looks for an excess of events (over the expected background) at any location in the sky within the field of view of ANTARES. In the "candidate list" search the likelihood of the events is evaluated for a reduced number of locations in correspondence with potential neutrino sources.

8.1.1 Full-sky search

The full-sky search is a general search for sources anywhere in the ANTARES visible sky, i.e. in the declination range (-90°, 48°). The source coordinates are not known and must be estimated by the clustering algorithm. In order to reduce the computational time it would require to evaluate the likelihood at every point in the sky, potentially significant clusters containing at least four events within a pre-clustering cone of three degrees diameter built around each event are first selected. Using a larger cone diameter or requiring a smaller number of events increases the computational time but does not result in a significant improvement of the analysis sensitivity. For each selected cluster the fit for the source coordinates starts at the center of gravity. The value of the test statistics is defined as the largest value observed among the selected clusters.

8.1.2 Candidate list search

In the candidate list search the number of locations in the sky where to test the existence of a point-source of neutrinos is restricted in order to increase the search sensitivity by reducing the effective trial factor associated with a full-sky scan. We search here for the most significant point of a list with 51 candidate sources (see Figure 8.1) selected by requiring them:

1. To be visible from ANTARES as up-going neutrino sources.
2. To be enough separated from each other to be resolved as independent sources by the telescope.
3. To produce high energy gamma-ray emission.

In comparison with the candidate list used in the first search for cosmic neutrinos [126] [127] done in ANTARES, we have 27 new objects. Most of these new sources were recently detected by IACTs like H.E.S.S. or MAGIC, but the list also includes a few objects observed during the first FERMI-LAT campaign [22]. These new cataloged sources were selected by convoluting their gamma-ray flux at Earth and exposure time to ANTARES. All the Galactic sources in the list are known to produce γ-rays in the TeV energy range. However, some new γ-ray sources in the GeV energy range were included as well taking into account the effect of the photon absorption by the EBL. The list was completed by adding the most significant

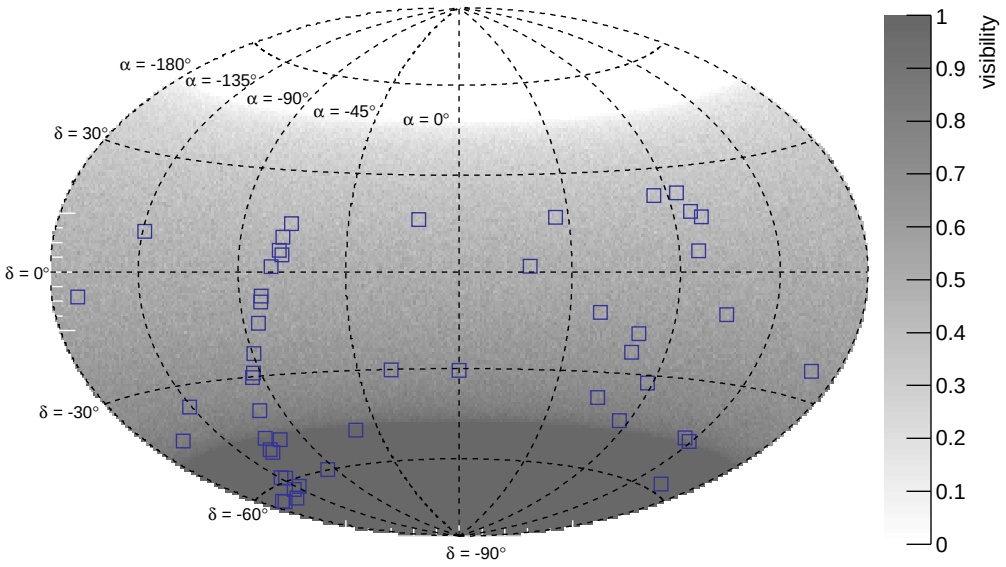

Figure 8.1: Skymap in equatorial coordinates showing the positions of the 51 candidate sources selected (squares) and the visibility fraction at the ANTARES site to upgoing neutrinos.

spot in the point source search performed by the Ice-Cube Collaboration using the 40 string detector [128]. Analogously to the full-sky search, the test statistic is defined as the maximum value observed at the 51 locations explored in the candidate list search.

8.2 Results from the searches

No statistically significant excess of events over the background was found neither in the full-sky search, nor in the search using a list of candidate sources. Therefore, we have calculated p-values and neutrino flux upper limits for point sources of neutrinos assuming a $\propto E^{-2}$ spectrum.

- **Full-sky search:** Using the E-M algorithm the most significant cluster of events was found at the best fit coordinates $(\alpha, \delta) = (313.8°, -64.9°)$. This cluster consist of 5 (9) events within 1 (3) degrees of that position (see Figure 8.2). The number of signal events estimated is $n_s = 5.3$. The value of the likelihood ratio for this cluster is $\lambda = 12.85$, such a value or a larger one is found in 2.6% of 10,000 only background pseudo-experiments. This corresponds to $\sim 2.2\sigma$ significance[1] and thus is compatible with a background fluctuation (Figure 8.3). When we apply the NML method the best cluster is found at $(\alpha, \delta) = (332.3°, -46.4°)$ (Figure 8.2). For this cluster $n_s = 3.8$ is the fitted number of events and $\lambda = 9.46$ the value of the statistical test. A cluster with equal or higher significance is found in about 40% of the only background pseudo-experiments (Figure 8.3).

  The E-M algorithm hot spot is also the top cluster obtained when a modified NML method version, accounting for the width of the zenith angle pull distribution (see Chapter 3), is used. Such a modification consists in the application of a scale factor (equivalent to the pull distribution width) to the angular error estimate parameter as used in the likelihood function. We recommend to follow this approach in future analysis for a more realistic treatment of the angular resolution.

- **Candidate list search:** The results from the search using the candidate list of 51 a priori selected sources are summarized in Table 8.2 and Table 8.3. The most signal-like candidate is 3C 279 with 82% (33%) post-trial corrected p-value obtained when

[1] In order to translate p-values into number of standard deviations the formula $\sigma = \mathrm{erf}^{-1}(1-\mathrm{p-value}) \times \sqrt{2}$ is used.

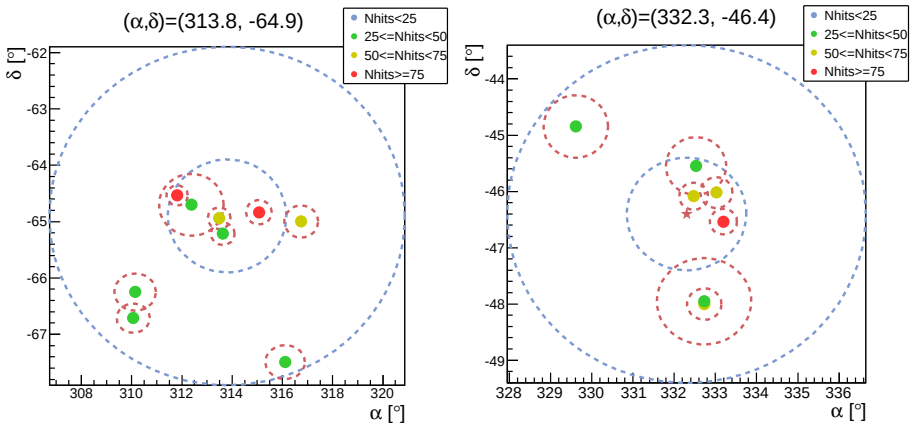

Figure 8.2: Neutrino candidate events (dots) around the position of most significant spot (indicated with a star) found in the full-sky search using the E-M clustering algorithm (left) and when we applied the NML method (right). The blue dashed circles are 1 and 3 degrees diameter cones drawn around the clusters best fit coordinates, the small ellipsoids around each event represent the uncertainty on their reconstructed directions. The color of each event indicates how many hits were used in its reconstruction.

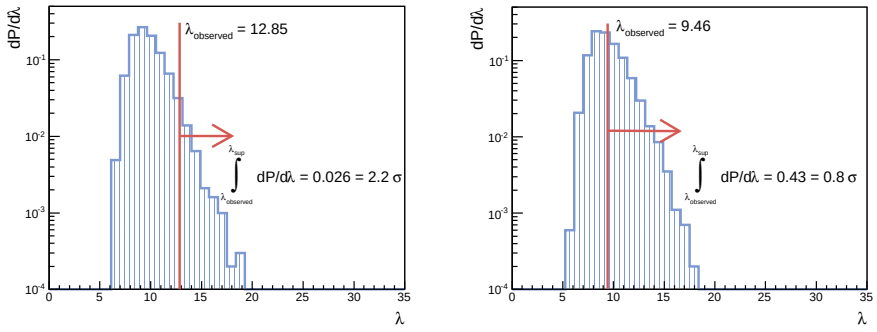

Figure 8.3: The significance of the best clusters found by applying the EM algorithm (left) and the NML method (right) are calculated from 10^4 only-background trials. In both cases the results obtained are compatible with the null hypothesis.

Method	λ	p-value	n_s	(α, δ)
E-M	12.85	0.03	5.3	(313.8°,-64.9°)
NML	9.46	0.43	3.8	(332.3°,-46.4°)

Table 8.1: Results from the full-sky search. The λ value, the p-value, the fitted number of signal events (n_s) and the estimated coordinates (α, δ) are given for the most significant spot found by the E-M and by the NML clustering methods respectively.

applying the E-M (NML) search algorithm. The result is therefore well compatible with the background only hypothesis. In Figure 8.4 Neyman type 90% CL neutrino flux upper limits are shown for the 51 candidate sources as a function of the source declination. Upper limits previously published by other neutrino experiments on sources from both the Southern and the Northern sky [129] [130] [131] [128] [132] are included for comparison. The sensitivity of our analysis is also compared with the IceCube 40+59 strings configuration sensitivity.

8.3 Upper limits for specific astrophysical neutrino emission models

The existing gamma ray data can be used to produce better estimations of the neutrino flux from candidate sources. Using the energy spectrum and source morphology measured by H.E.S.S (approximated to a Gaussian distribution), cosmic neutrino signal rates at the ANTARES site are calculated in [46] for the supernova remnant RX J1713.7-3946 and the pulsar wind nebula Vela X. Assuming these emission models (Equations 8.1, 8.2) we have produced new upper limits using the NML clustering method. For this during the pseudo-experiments generation fake signal events are injected considering the measured emission profile, but in the likelihood function we just convolute our PSF with another 2D-Gaussian which width is determined optimizing the source extension for discovery. The results obtained are shown in Figure 8.5. The Model Rejection Factor (MRF), i.e. the ratio between the 90% CL upper limit and the expected number of signal events is also included; we constrain a flux 7.6 higher than the theoretical prediction for Vela X and a flux 9.8 higher than the expectation for RX J1713.7-3946.

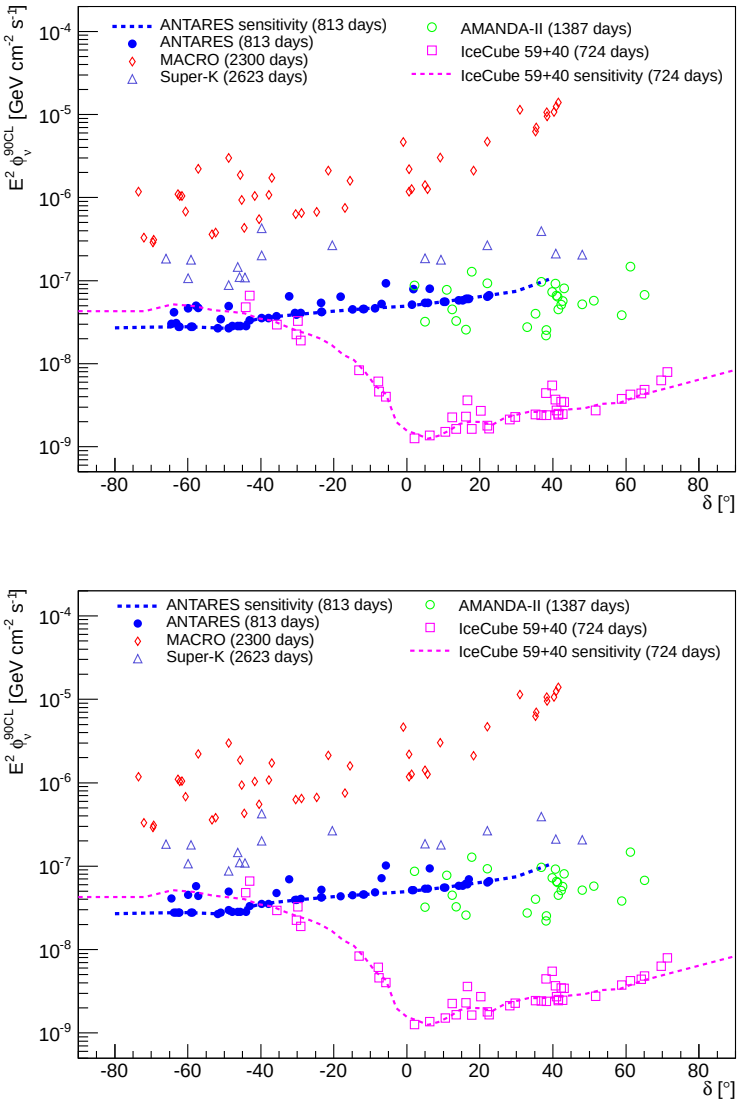

Figure 8.4: Neutrino flux upper limits 90% CL for the 51 candidates (see Tables 8.2 and 8.3) as a function of the source declination. Results reported by other neutrino experiments in both the Southern and Northern Hemisphere are also included. The ANTARES sensitivity of this analysis (solid line $\delta\epsilon[-90°, +40°]$) is compared to the Ice-Cube 40+59 strings analysis sensitivity (dashed line). These results are shown separately for the E-M (top) and the NML (bottom) clustering methods.

$$\frac{d\phi}{dE} = 16.8 \times 10^{-12} \left(\frac{E_\nu}{TeV}\right)^{-1.72} e^{-\sqrt{\frac{E}{2.1TeV}}} \ \mathrm{TeV}^{-1}\mathrm{cm}^{-2}\mathrm{s}^{-1} \tag{8.1}$$

$$\frac{d\phi}{dE} = 11.75 \times 10^{-12} \left(\frac{E_\nu}{TeV}\right)^{-0.98} e^{-\sqrt{\frac{E}{0.84TeV}}} \ \mathrm{TeV}^{-1}\mathrm{cm}^{-2}\mathrm{s}^{-1} \tag{8.2}$$

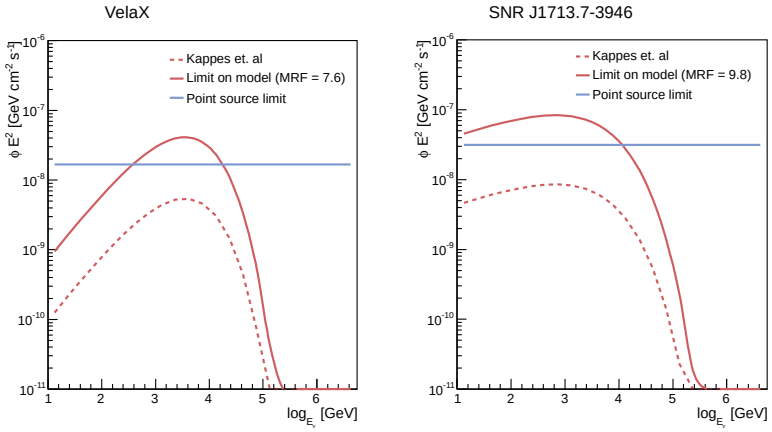

Figure 8.5: Feldman-Cousins 90% CL upper limits (solid lines) and neutrino flux models for Vela X (left) and RX J1713.7-3946. The solid horizontal lines show the limits obtained assuming these sources are point-like objects. The flux models are taken from [46].

8.4 Search for neutrinos from gravitational lensing objects

The gravitational lensing effect is known to enhance the photon flux from sources placed behind them. Neutrino fluxes would also be magnified by a gravitational lensing object [133], which could allow to observe sources otherwise below the detection threshold. As discussed in detail in [134], from catalogues including more than one hundred gravitational lensing objects, 9 systems were selected to look for an excess of neutrino events at their locations on the basis of the following criteria:

1. The system is in the field of view of ANTARES.
2. The lensed object is a known AGN.
3. The system was detected in X-ray and/or gamma-ray observations.

4. In case the object has not been identified as a gamma-ray emitter, a magnification factor larger than 20 for at least one of the multiple images of the source produced is required.

In addition, two galaxy clusters with particularly large magnification factors were included. The 11 sources finally selected are listed in table 8.4.

No significant excess of events was found at any of the 11 directions considered [2]. The less background like source is SDSS 1004+4112 with coordinates $(\alpha, \delta) = (151.15^\circ, 41.21^\circ)$. For this cluster $\lambda = 0.35$ and the fit assigns $n_s = 0.6$ (only 2 neutrino candidates events were detected within a 3 degrees cone drawn around the source position). The post-trial p-value when looking at 11 (51+11) sources is 0.49 (0.99), which is compatible with the only background hypothesis. The results of this search are summarized in table 8.4.

[2] In this search, the NML method was used.

Table 8.2: Candidate list search results for the EM algorithm.

Source name	$\delta[^\circ]$	$\alpha[^\circ]$	p-value	λ	n_s	ϕ_ν^{90CL}
3C 279	-5.79	194.05	0.03	2.19	0.96	9.3
PKS 2005-489	-48.79	255.70	0.07	1.64	1.36	4.9
HESS J1023-575	-57.76	155.83	0.08	1.48	3.04	5.0
Cir X-1	-57.17	230.17	0.10	1.20	1.37	4.7
RGB J0152+017	1.79	28.17	0.10	1.17	1.41	7.9
MGRO J1908+06	6.27	286.99	0.10	1.11	0.86	8.0
PKS 0548-322	-32.27	87.67	0.10	1.09	1.84	6.5
ESO 139-G12	-59.94	264.41	0.11	1.06	2.62	4.6
IceCube hotspot	-18.15	75.45	0.14	0.75	0.79	6.4
PSR B1259-63	-63.83	195.70	0.18	0.62	1.42	4.2
1ES 1101-232	-23.49	165.91	0.23	0.36	1.00	5.4
HESS J1616-508	-50.97	243.97	0.25	0.33	0.95	3.4
HESS J1837-069	-6.95	279.41	0.32	0.12	0.41	5.2
HESS J1303-631	-63.20	195.77	0.39	0.06	0.50	3.1
HESS J1356-645	-64.50	209.00	0.41	0.05	0.29	3.0
H 2356-309	-30.63	359.78	0.39	0.05	0.62	4.1
HESS J1834-087	-8.76	278.69	1.00	0.01	0.20	4.6
1ES 1101-232	-23.43	74.27	1.00	0.00	0.10	5.4
RCW 86	-62.48	220.68	1.00	0.00	0.00	2.8
VER J0648+152	15.27	102.20	1.00	0.00	0.00	5.8
HESS J1614-518	-51.82	243.58	1.00	0.00	0.01	2.7
HESS J1741-302	-30.22	329.72	1.00	0.00	0.00	3.9
PKS 0426-380	-37.93	67.17	1.00	0.00	0.00	3.5
PKS 2005-489	-48.82	302.37	1.00	0.00	0.00	4.9
W51C	14.19	290.75	1.00	0.00	0.00	5.8
1ES 0347-121	-11.99	57.35	1.00	0.00	0.00	4.6
PKS 1454-354	-35.67	224.36	1.00	0.00	0.00	3.7
RXJ 1713.7-3946	-39.75	258.25	1.00	0.00	0.00	3.5
HESS J1503-582	-58.74	226.46	1.00	0.00	0.00	2.8
PKS 0235+164	16.61	39.66	1.00	0.00	0.00	6.0
HESS J1912+101	10.15	288.21	1.00	0.00	0.00	5.6
Centaurus A	-43.02	201.36	1.00	0.00	0.00	3.3
MSH 15-52	-59.16	228.53	1.00	0.00	0.00	2.8

Table 8.2 (continued)

Source name	$\delta[^\circ]$	$\alpha[^\circ]$	p-value	λ	n_s	ϕ_ν^{90CL}
Vela X	-45.60	128.75	1.00	0.00	0.00	2.9
RX J0852.0-4622	-46.37	133.00	1.00	0.00	0.00	2.9
HESS J0632+057	5.81	98.24	1.00	0.00	0.00	5.4
Geminga	17.01	98.31	1.00	0.00	0.00	6.0
HESS J1507-622	-62.34	226.72	1.00	0.00	0.00	2.8
PKS 0727-11	-11.70	112.58	1.00	0.00	0.00	4.6
W28	-23.34	270.43	1.00	0.00	0.00	4.2
LS 5039	-14.83	276.56	1.00	0.00	0.00	4.5
SS 433	4.98	287.96	1.00	0.00	0.00	5.4
3C454.3	16.15	343.50	1.00	0.00	0.00	6.0
Galactic Center	-29.01	266.42	1.00	0.00	0.00	4.1
Crab	22.01	83.63	1.00	0.00	0.00	6.4
PKS 1502+106	10.52	226.10	1.00	0.00	0.00	5.6
W44	1.38	284.04	1.00	0.00	0.00	5.1
HESS J1741-302	-30.20	265.25	1.00	0.00	0.00	3.9
IC443	22.51	94.21	1.00	0.00	0.00	6.6
HESS J1632-478	-47.82	248.04	1.00	0.00	0.02	2.9
PKS 0537-441	-44.08	84.71	1.00	0.00	0.00	2.9

The equatorial coordinates (α, δ), pre-trial p-value, test statistic, number of fitted signal events and upper limit on the E_ν^{-2} flux ($\phi_\nu^{90\%}$) are given sorted by increasing λ value.

Table 8.3: Candidate list search results for the NML method.

Source name	$\delta[^\circ]$	$\alpha[^\circ]$	p-value	λ	n_s	ϕ_ν^{90CL}
3C 279	-5.79	194.05	0.008	2.28	0.99	10.2
HESS J1023-575	-57.76	155.83	0.013	1.71	1.58	5.7
MGRO J1908+06	6.27	286.99	0.02	1.35	0.89	9.4
PKS 2005-489	-48.79	255.70	0.03	1.03	0.85	5.0
PKS 0548-322	-32.27	87.67	0.04	0.75	0.85	7.0
ESO 139-G12	-59.94	264.41	0.07	0.37	0.69	4.6
Cir X-1	-57.17	230.17	0.08	0.32	0.79	4.4
HESS J1837-069	-6.95	279.41	0.07	0.23	0.54	7.2
HESS J1356-645	-64.50	209.00	0.11	0.08	0.37	4.1
PKS 1454-354	-35.67	224.36	1.00	0.00	0.00	4.8
1ES 1101-232	-23.43	74.27	1.00	0.00	0.00	4.2
Geminga	17.01	98.31	1.00	0.00	0.00	6.9
PKS 2005-489	-48.82	302.37	1.00	0.00	0.00	5.0
HESS J1616-508	-50.97	243.97	1.00	0.00	0.00	2.8
HESS J1834-087	-8.76	278.69	1.00	0.00	0.00	4.8
HESS J1503-582	-58.74	226.46	1.00	0.00	0.00	2.8
3C454.3	16.15	343.50	1.00	0.00	0.00	6.2
MSH 15-52	-59.16	228.53	1.00	0.00	0.00	2.8
HESS J1614-518	-51.82	243.58	1.00	0.00	0.00	2.7
PKS 1502+106	10.52	226.10	1.00	0.00	0.00	5.6
LS 5039	-14.83	276.56	1.00	0.00	0.00	4.5
PSR B1259-63	-63.83	195.70	1.00	0.00	0.00	2.8
W28	-23.34	270.43	1.00	0.00	0.00	4.2
RXJ 1713.7-3946	-39.75	258.25	1.00	0.00	0.00	3.5
HESS J0632+057	5.81	98.24	1.00	0.00	0.00	5.4
HESS J1632-478	-47.82	248.04	1.00	0.00	0.00	2.9
HESS J1303-631	-63.20	195.77	1.00	0.00	0.00	2.8
RCW 86	-62.48	220.68	1.00	0.00	0.00	2.8
1ES 1101-232	-23.49	165.91	1.00	0.00	0.00	4.2
H 2356-309	-30.63	359.78	1.00	0.00	0.00	3.9
Vela X	-45.60	128.75	1.00	0.00	0.00	2.9

Table 8.3 (continued)

Source name	$\delta[^\circ]$	$\alpha[^\circ]$	p-value	λ	n_s	ϕ_ν^{90CL}
SS 433	4.98	287.96	1.00	0.00	0.00	5.4
VER J0648+152	15.27	102.20	1.00	0.00	0.00	5.8
PKS 0727-11	-11.70	112.58	1.00	0.00	0.00	4.6
Galactic Center	-29.01	266.42	1.00	0.00	0.00	4.1
Centaurus A	-43.02	201.36	1.00	0.00	0.00	3.3
HESS J1507-622	-62.34	226.72	1.00	0.00	0.00	2.8
RX J0852.0-4622	-46.37	133.00	1.00	0.00	0.00	2.9
HESS J1741-302	-30.22	329.72	1.00	0.00	0.00	3.9
IceCube hotspot	-18.15	75.45	1.00	0.00	0.00	4.4
PKS 0537-441	-44.08	84.71	1.00	0.00	0.00	2.9
1ES 0347-121	-11.99	57.35	1.00	0.00	0.00	4.6
PKS 0426-380	-37.93	67.17	1.00	0.00	0.00	3.5
RGB J0152+017	1.79	28.17	1.00	0.00	0.00	5.1
HESS J1741-302	-30.20	265.25	1.00	0.00	0.00	3.9
IC443	22.51	94.21	1.00	0.00	0.00	6.6
Crab	22.01	83.63	1.00	0.00	0.00	6.4
PKS 0235+164	16.61	39.66	1.00	0.00	0.00	6.0
W44	1.38	284.04	1.00	0.00	0.00	5.1
HESS J1912+101	10.15	288.21	1.00	0.00	0.00	5.6
W51C	14.19	290.75	1.00	0.00	0.00	5.8

The equatorial coordinates (α, δ), pre-trial p-value, test statistic, number of fitted signal events and upper limit on the E_ν^{-2} flux ($\phi_\nu^{90\%}$) are given sorted by increasing λ value.

Lens name	$\delta[^\circ]$	$\alpha[^\circ]$	p-value	λ	n_s	ϕ_ν^{90CL}
J1004+4112	41.21	151.15	0.05	0.35	0.63	12.93
RXJ0911+0551	5.85	137.86	0.09	0.09	0.41	7.24
A370	-1.59	39.96	0.12	0.02	0.18	6.50
RXJ1131-1231	-12.53	172.97	1.00	0.00	0.00	4.58
B1030+074	7.19	158.39	1.00	0.00	0.00	5.52
B1422+231	22.93	216.16	1.00	0.00	0.00	6.64
PKS 1830-211	-21.06	278.42	1.00	0.00	0.00	4.30
J0924+0219	2.32	141.23	1.00	0.00	0.00	5.14
A1689	-1.37	197.89	1.00	0.00	0.00	4.96
J1029+2623	26.39	157.31	1.00	0.00	0.00	6.82
JVAS B0218	35.94	35.27	1.00	0.00	0.00	9.06

Table 8.4: Source names, coordinates, (pre-trial) p-values, likelihood ratio, number of fitted signal events and upper limits (90% CL) for the eleven gravitational lensing objects selected to look for cosmic neutrino emission.

Conclusions

Neutrino astronomy aims at the exploration of the universe using neutrinos as cosmic probes. The main motivation when constructing a neutrino telescope comes from the present lack of knowledge of the origin and the powering mechanism of the high energy cosmic rays. Presumably, the charged particles radiation constituted by the cosmic rays is the result of acceleration processes that happen in violent astrophysical scenarios like Supernova remnants, Micro-quasars or AGNs. However, because the cosmic rays lose the directionality when they interact with the interstellar and the intergalactic magnetic fields, such connection has not been proved yet. Under the likely assumption that part of these cosmic rays interact with the ambient matter at their acceleration site, a significant production of neutrinos and of gamma-rays is expected. The detection of neutrinos in correspondence with a TeV gamma-ray source would bring new light on the problem of the origin of cosmic rays and would also be an unambiguous demonstration for hadronic acceleration mechanisms.

The ANTARES detector is the first fully operative neutrino telescope operating at depth in the Sea water. Since the deployment of the first instrumentation line in 2006, the detector has been taking data almost continuously and with improved efficiency. In its final configuration, achieved in 2008, the detector consists of 885 PMTs arranged on 12 detection lines 450 m long. While the first results obtained have been already published a broad number of physics analysis is ongoing.

The experience gained with ANTARES is the most valuable demonstration of the feasibility for the construction of a multi-km^3 neutrino telescope in the Mediterranean Sea. Such an instrument would explore the Southern Hemisphere sky with unprecedented sensibility and angular resolution. It should also be able to confirm the first evidences reported by the IceCube observatory about the detection of high energy neutrinos with an astrophysical origin

[135].

This thesis has addressed two main topics. The first one was the time calibration of the ANTARES detector and the second one the search for cosmic neutrino sources. The main conclusions obtained from both analysis are summarized below.

Time calibration:

A new method to obtain the time calibration constants has been implemented. This method uses atmospheric muon data and, therefore, it does not require to stop the physics runs acquisition as other systems developed with the same purpose do. The method is an iterative technique which exploits the muon track residuals information and, in this work, it has been extensively used to perform the inter-line time calibration.

After correcting the detector timing taking into account the inter-line time offsets measured with this new technique an enhancement of up to a factor 2 in the number of good quality reconstructed events has been observed. A better agreement between data and MC has also been found when comparing the distributions of the quality of the reconstruction parameter obtained when accounting for these time corrections. Using simulations it was demonstrated that not correcting the inter-line timing would result in a $\sim$40$\%$ degraded angular resolution.

The inter-line offsets have been monitored using data collected between years 2008 and 2012. This study has confirmed the long-term stability of these calibration parameters.

The Optical Beacon system has been used to cross-check, in an independent way, the results provided by the method based on the muon track residuals. This test showed that both methods agree within 1 ns. Only a large difference was found for line 8, which can not be directly illuminated by the laser Beacon currently operative. Such a discrepancy could be soon clarified by using a new laser that has been recently installed at the bottom of an instrumentation line placed outside the ANTARES layout.

The number of of high-quality reconstructed events is slightly larger when correcting for the muon track residuals inter-line offsets than for the Laser Beacon time corrections. The muon

track residuals method method is, therefore, currently used to provide the official inter-line calibration constants needed for the physics analysis.

The intra-line time calibration obtained with the LED Beacon system has been cross-checked using the method based on the muon track residuals. The results obtained have shown a good agreement (within 1 ns) for about 90% of the studied detector channels.

A monitoring study of the TVC calibration parameters has been done using data collected in 4 years. The analysis has confirmed the robustness and stability of the TVC dynamic range at the level demanded to fulfill the requirements on time calibration.

Search for cosmic neutrino sources:

A search for cosmic neutrinos using four years of ANTARES data has been conducted. For this analysis a total of 7419 runs were selected on the basis of data quality principles. This data amounts to 813 days of livetime.

The final sample of events has been obtained applying three selection cuts: $\cos(\theta) > 0$, $\beta < 1^\circ$ and $\Lambda > -5.2$. The cut on the quality of the reconstruction parameter Λ was chosen to optimize the flux required for a 5σ discovery. This was done following a "blind" procedure by using right ascension scrambled events. The final sample contained 3058 neutrino candidates, a number in good agreement with the MC expectations.

Two unbinned clustering algorithms have been used to find maximum likelihood estimates of the unknown parameters of a model which describes the data as the two component mixture of signal and background. The first clustering method was based on the Expectation-Maximization algorithm adapted to perform a search for neutrino sources without depending on the detector point spread function. The NML method instead used the information of the angular error estimate to account for the angular resolution on an event-by-event basis. Both search methods took into account the energy of the events estimated by the number of hits used in the track fit.

A likelihood ratio test was used to determine the significance of the search. The sensitivity

of this analysis was shown to be a factor of $\sim$2.7 better than the sensitivity of the first search for point sources of neutrinos done in ANTARES.

Two different search approaches have been applied. The first one consisted on a survey of all the sky which is visible as upgoing at the ANTARES location, i.e., $\delta \in [-90^\circ, 48^\circ]$. In the second approach the search was reduced at the location of 51 gamma-ray sources candidates for high energy neutrino emission. This list of candidate sources added, with respect the first search for point sources done in ANTARES, 27 new sources selected by convolving their gamma-ray flux and visibility for ANTARES.

No statistically significant excess of events has been found neither in the full-sky search, nor in the search using the list of candidate sources. The most signal-like cluster was found at the coordinates $(\alpha, \delta) = (313.8^\circ, -64.9^\circ)$ in the full-sky search when using the E-M algorithm. This cluster consisted on 5 events within a 1 degree diameter cone around the fitted cluster position. The number of fitted signal events was $n_s = 5.3$ and the value of the test statistic $\lambda = 12.8$. Expressed in number of standard deviations the significance of this cluster was 2.1σ and, therefore, compatible with a background fluctuation. When the NML method was applied the best cluster was found at $(\alpha, \delta) = (332.3^\circ, -46.4^\circ)$. The fitted number of signal events for this cluster was n_s = 3.8 and $\lambda = 9.46$ was the value of the statistical test. This value or a larger one was found in about 40$\%$ of the only background pseudo-experiments.

The E-M hot spot was also found on top position when the NML method was applied to the data modifying the way the angular uncertainty information is used in the likelihood function by multiplying by a scaling factor accounting for the width of the zenith angle pull distribution. We recommend to follow this scheme in future analysis for a more realistic treatment of the angular resolution.

In the candidate list search, the less background-like source was 3C-279, which is a blazar discovered at coordinates $(\alpha, \delta) = (194.1^\circ, -5.8^\circ)$. The E-M algorithm fitted $n_s = 0.96$ and $\lambda = 2.19$, while the NML method assigned $n_s = 0.96$ and $\lambda = 2.28$ for this source. The result in both cases is well compatible with the only background hypothesis.

Not having found any source of neutrinos in the data, upper limits for the 51 sources in the candidate list assuming a E^{-2} flux emission spectrum have been calculated. Some of these limits are the most restrictive ones set on sources in the Southern Hemisphere.

Assuming two specific astrophysical neutrino emission models for the Vela X pulsar and the RX J1713.7-3946 supernova remnant 90$\%$ CL upper limits have been calculated. The Model Rejection Factor was also determined for both sources. A flux 7.8 (9.1) times more intense than the predicted flux could be constrained for Vela X (RX J1713.7-3946).

A search for neutrino emission at the location of 11 gravitational lensing objects has been conducted considering a possible enhancement of the neutrino flux from sources behind Galaxy clusters. The results obtained are compatible with the only background hypothesis, being SDSS 1004+4112 the source with the highest value of the test statistics observed. Upper limits on the neutrino flux from these sources have been produced.

Resumen

Introducción

La astronomía de neutrinos, un campo experimental de la astrofísica de partículas relativamente joven, se propone la observación de los fenómenos más energéticos del universo utilizando neutrinos como mensajeros cósmicos. La motivación principal a la hora de construir un telescopio de neutrinos proviene de las incógnitas existentes sobre el origen y la producción de los rayos cósmicos de más alta energía. Sospechamos que dicha radiación cósmica sea el resultado de procesos de aceleración en escenarios astrofísicos, sin embargo, debido a la pérdida de la direccionalidad de estas partículas por la acción de campos magnéticos inter-estelares durante su propagación, no existe todavía confirmación de dicha conexión. Bajo este esquema, los llamados modelos de aceleración hadrónicos predicen la emisión de neutrinos (y también rayos gamma) a partir de la desintegración de partículas secundarias (piones) producidas en la interacción de los rayos cósmicos con la materia y la radiación en el entorno de la fuente de producción. Las particulares características de los neutrinos les permiten recorrer distancias cosmológicas sin perder la información sobre su origen, lo que les convierte en candidatos ideales para la exploración de las regiones más lejanas del universo. El descubrimiento de una fuente cósmica de neutrinos de alta energía aportaría valiosa información sobre el origen de los rayos cósmicos y la eficacia de los mecanismos de aceleración hadrónica.

Los rayos cósmicos

Descubiertos por Victor Hess en 1912, los rayos cósmicos son una radiación formada por partículas cargadas que alcanza la Tierra desde el espacio exterior. Hoy en día sabemos que los rayos cósmicos están constituidos principalmente por protones y otros núcleos ligeros y que su espectro energético sigue una ley de potencias de la forma $dN/dE \propto E^{-\gamma}$, donde

N es el número de partículas detectadas, E su energía y γ el índice espectral. El espectro de los rayos cósmicos, como han observado multitud de experimentos, se extiende unos 13 órdenes de magnitud en energía y cerca de 31 en flujo, presentando dos cambios importantes conocidos como la rodilla (a energías $\sim 5 \times 10^{15}$ eV) y el tobillo (por encima de los 10^{19} eV).

Se considera que los rayos cósmicos por debajo de la rodilla tienen un origen galáctico y que la variación observada en el índice espectral es una consecuencia de la transición extragaláctica. Por encima del tobillo parece confirmarse la existencia de un corte o "cutoff" cuya causa se debe, con gran probabilidad, a la interacción de las partículas de ultra alta energía con la radiación de fondo cósmica. El mecanismo responsable de este corte sería el denominado efecto GZK por las siglas de los autores que lo formularon en los años 60.

En los mismos escenarios astrofísicos que se han propuesto para la aceleración de los rayos cósmicos, tendría lugar la emisión de un haz de neutrinos si, como parece verosímil, una fracción de aquellos rayos cósmicos interacciona con la materia o los fotones existentes en el entorno cercano a la fuente (ver ecuaciones R.E1 y R.E2). De la misma manera, a partir de la desintegración de los piones neutros resultantes, tendría lugar la emisión de fotones de alta energía. Sin embargo, los neutrinos, al poder escapar de entornos mucho más densos, podrían apuntar a procesos que en cambio permanecerían ocultos a la astronomía tradicional.

$$\begin{aligned} p + N &\rightarrow \pi + X \quad (\pi = \pi^{\pm}, \pi^0) \\ p + \gamma &\rightarrow \Delta^+ \rightarrow \begin{cases} \pi^0 + p \\ \pi^+ + n \end{cases} , \end{aligned} \tag{R.E1}$$

con las desintegraciones subsiguientes:

$$\pi^+(\pi^-) \rightarrow \mu^+(\mu^-)\nu_\mu(\bar{\nu}_\mu), \;\; \mu^+ \rightarrow e^+\bar{\nu}_\mu\nu_e, \;\; \mu^- \rightarrow e^-\nu_\mu\bar{\nu}_e, \tag{R.E2}$$

Astronomía de neutrinos

Los neutrinos son partículas estables, que solo interaccionan débilmente y que apenas tienen masa. Su bajísima sección eficaz de interacción, razón que les permite viajar distancias cosmológicas sin ver alterada su trayectoria, resulta también una importante desventaja experimental al convertirlo en una partícula muy difícil de detectar. Además, aunque este efecto se compensa parcialmente con el hecho de que la probabilidad de interacción del neutrino au-

menta con su energía [1], las predicciones teóricas sobre el flujo de neutrinos cósmicos sugieren valores muy bajos, aunque con grandes incertidumbres. Hasta la fecha, sólo se ha conseguido detectar neutrinos astrofísicos de baja energía ($\leq$ 10 MeV), producidos en el Sol y en la explosión de la supernova SN1987A. Si queremos atrapar unos pocos neutrinos cósmicos de alta energía, y en un tiempo razonable, es imprescindible disponer de volúmenes de detección gigantescos. En este sentido, el diseño actual de un telescopio de neutrinos se basa en la propuesta de Markov de utilizar volúmenes naturales como medio de detección baratos. Hoy en día conocemos la existencia de tres sabores de neutrinos; el neutrino del electrón (ν_e), el neutrino del muón (ν_μ) y el tauónico (ν_τ). Además, sabemos que estas partículas pueden mutar, oscilando entre sabores a través del llamado mecanismo de oscilación de neutrinos. Este hecho se traduce en un flujo de neutrinos detectable en la tierra con un ratio $\nu_e : \nu_\mu : \nu_\tau = 1 : 1 : 1$.

Telescopios de neutrinos

El principio básico de detección de un telescopio de neutrinos se basa en la observación de la luz de Cherenkov inducida por el paso de una partícula cargada y relativista como resultado de la interacción de un neutrino de alta energía en el entorno. Para poder registrar los fotones Cherenkov producidos en este proceso se utilizan tubos fotomultiplicadores (PMTs) ordenados formando una estructura tridimensional en el seno de un medio ópticamente transparente (como el agua del mar o el hielo antártico).

Dependiendo del tipo de neutrino que haya interaccionado podremos distinguir diferentes patrones en el detector. El más interesante en nuestro caso es el que produce un muón capaz de atravesar una gran parte del detector dejando una señal experimental clara que nos permite obtener una buena reconstrucción de su trayectoria. El hecho de que a energías del orden de los 10 TeV la dirección del muón sea prácticamente colineal con la del neutrino incidente, posibilita hacer astronomía con un telescopio de neutrinos.

El principio de detección empleado no está exento de fondo. Tanto los muones como los neutrinos originados en la interacción de rayos cósmicos en las capas altas de la atmósfera terrestre pueden producir una señal en nuestro detector indistinguible de la que dejaría la interacción de un neutrino genuínamente cósmico. Para reducir la contaminación por muones atmosféricos podemos restringir nuestra búsqueda al hemisferio celeste opuesto al que se sitúa

[1] Los telescopios de neutrino actuales están optimizados para detectar neutrinos con energías entre las decenas de GeV y los centenares de TeV.

sobre el horizonte del detector, i.e., seleccionamos sólo aquellos eventos que son reconstruidos como ascendentes, utilizando así la propia tierra como filtro. Los neutrinos atmosféricos, aunque con un flujo varios órdenes de magnitud inferior al de los muones, constituyen sin embargo un fondo irreducible y solo pueden ser discriminados a partir del estudio de su distribución espacial y energética.

Los modelos teóricos más realistas indican que volúmenes del detector inferiores a 1km^3 no son efectivos para llegar a descubrir una fuente astrofísica de neutrinos. El observatorio de neutrinos IceCube, situado en el polo sur geográfico y completado en el año 2011, es el primer telescopio de neutrinos en funcionamiento con un volumen total del este orden. Dicho instrumento consta de 5160 PMTs distribuidos en 79 líneas situadas a una profundidad entre 1450 m y 2450 m. El consorcio KM3NeT representa a su vez el proyecto más realista para la instalación de un telescopio de neutrinos de varios km^3 en el hemisferio norte. Este detector complementaría la sensibilidad de IceCube con una resolución angular sin precedentes.

ANTARES

Situado a unos 43 km de la costa de Tolón (Francia), el telescopio de neutrinos ANTARES está formado por 885 tubos fotomultiplicadores, que se distribuyen de manera uniforme a lo largo de 12 líneas de instrumentación de 450 m de longitud, las cuales permanecen ancladas al fondo marino a una produndidad de 2475 metros mediante pesos muertos y son sostenidas verticalmente gracias a la acción de una gran boya situada en el extremo superior. Las 12 líneas se ordenan siguiendo un esquema octogonal que optimiza la respuesta del detector en ángulos acimutales. La distancia entre las líneas varía entre unos 60 y 75 m. Cada una de ellas dispone de un módulo de control en su base desde el que, mediante cables electro-ópticos, se conecta a la llamada *junction-box*. Los fotomultiplicadores de gran superficie utilizados para registrar la luz de Cherenkov se alojan en el interior de módulos ópticos (OM), que consisten en una esfera de borosilicato de 41.7 cm de diámetro y 15 mm de grosor que lo protege de las altas presiones de las produndidades. Estructuras mecánicas denominadas pisos o *storeys* sostienen un triplete de módulos ópticos, orientados hacia abajo un ángulo de 45° grados respecto a la horizontal para aumentar la eficiencia de detección de trazas que se propagan de manera ascendente. Existen 25 *storey* en cada línea de instrumentación, colocados equiespaciadamente con una separación de 14.5 m y situándose el primero a una altura de 100 m sobre el fondo marino.

Además de los 3 OMs, cada *storeys* aloja un contenedor cilíndrico de titanio con los dispositivos electrónicos necesarios para el control de la alimentación y la transmisión de las señales registradas por los PMTs. El principal componente de la electrónia en ANTARES, el chip ARS, se encarga de digitalizar todas aquellas señales eléctricas que superan los 0.3 fotoelectrones (p.e.) de carga, o condición umbral L0. Todas las señales que cumplen dicha condición son enviadas a la orilla a través de un cable electro-óptico que parte desde la *junction-box*. Una vez en la sala de control, las señales son procesadas con el objetivo de reducir el ruido debido a la contribución de un fondo óptico de diverso origen. Con este propósito se aplican filtros basados en diferentes criterios. En particular, los llamados algoritmos T3 y 3N se encargan de buscar correlaciones causales con señales de física, como la producida por el paso de un muón.

Las propiedades ópticas del entorno marino condicionan la respuesta del detector. En particular, la absorción y la dispersión de la luz a la profundidad en la que se encuentra ANTARES son dos parámetros que influyen notablemente en la reconstrucción y por tanto en la respuesta del telescopio. Por otra parte, la concetración de partículas en el medio marino causa la sedimentación y la acumulación de organimos biológicos microscópicos, que afectan a la transparencia del OM reduciendo su eficiencia en la transmisión de la luz. Por último la emisión de luz por parte de bacterias bioluminiscentes y la desitegración de isótopos ^{40}K capaz de producir un electrón con la suficiente energía como para inducir la producción de fotones Cherenkov son dos procesos naturales que suponen un ruido óptico con una frecuencia en torno a los 60 KHz.

Tras una primera fase de investigación, desarrollo y evalución de las condiciones del medio, que duró varios años, la construcción del telescopio de neutrinos ANTARES comenzó en enero del año 2007 con la instalación de las primeras 5 líneas de instrumentación. En diciembre de ese mismo año se añadieron 5 nuevas líneas y ya en mayo de 2008 se llevó a cabo la operación que condujo a la conexión de la decimosegunda línea de detección, finalizándose la construcción del detector. En el momento de escribir esta tesis ANTARES lleva más de seis años en funcionamiento y detecta una media de 3 neutrinos ascendentes al día.

Fuentes astrofísicas de neutrinos

Como hemos mencionado con anterioridad, es muy probable que se produzca un número importante de neutrinos de alta energía (junto con rayos gamma) en los mismos escenarios astrofísicos propuestos para la aceleración de los rayos cósmicos. A continuación repasamos brevemente algunas de las fuentes candidatas más interesantes.

- **Fuentes galácticas:** Entre las fuentes galácticas más prometedoras podemos encontrar los llamados remanentes de supernova (SNR), los micro-quásares o el centro galáctico. Un SNR es el resultado de la explosión de un estrella muy masiva, proceso en el que se desarrolla una poderosa onda de choque cuando el material estelar sale expelido a velocidades del orden del 10% de la velocidad de la luz y en el que, según el mecasimo de Fermi de primer orden, se puede producir una aceleración de partículas cargadas de forma eficiente. Los SNRs están considerados como los mejores candidatos para la producción de los rayos cósmicos galácticos hasta la energía de la *rodilla*. Los micro-quásares, por su parte, son sistemas binarios cuya principal característica es la emisión de chorros de partículas relativistas que se han podido observar analizando su espectro electromagético en frecuencias de ondas de radio. Se piensa que el proceso que da origen a estos fenómenos es el acrecimiento de la materia de su compañero por parte del componente del sistema más masivo (una estrella de neutrones o un agujero negro por lo general). La observación de líneas de rayos X del hierro en los chorros que emiten estos objetos nos hace sospechar que pueden acelerar bariones hasta energías del orden de los 10 PeV. Finalmente, el centro galáctico tiene un especial interés para la astronomía de neutrinos puesto que en esta región, observatorios de rayos gamma como H.E.S.S. [2], han conseguido localizar un buen número de fuentes capaces de producir fotones con energías del orden del TeV.

- **Fuentes extra-galácticas:** En relación a las fuentes de origen extra-galáctico podemos destacar los llamados núcleos de galaxia activos (AGNs) y las explosiones de rayos gamma (GRBs). Se considera que los primeros son el resultado de la acreción de materia por parte de un agujero negro supermasivo (de entre un millón y mil millones de masas

[2] Estos telescopios son capaces de obtener imágenes astrofísicas a partir del estudio de la radiación Cherenkov inducida en la atmósfera terrestre por la interacción de un fotón de alta energía.

solares) emplazado en el centro de una galaxia húesped. Dependiendo del ángulo de su eje de rotación respecto al observador y de la relación entre la intensidad que alcanzan en ondas de radio respecto a su flujo en el óptico estos sistemas se clasifican en diversos tipos (Blazars, Seyfert I, Seyfert II, Radio galaxias...). Los GRBs son los fenómenos más energéticos del universo, alcanzando energías de $\mathcal{O}(10^{51} - 10^{54})$ erg. Consisten en ráfagas de rayos gamma (de entre 1 milisegundo a varios minutos de duración) producidas en el momento del colapso de una estrella muy masiva en un agujero negro. Por tanto estas últimas son, en contraposición a las anteriormente descritas, fuentes transitorias.

Objetivos y Metodología

Los dos principales objetivos del presente trabajo de investigación son el desarrollo de nuevos métodos para obtener los parámetros de la calibración temporal del detector y el análisis de los datos de física para la búsqueda de fuentes de neutrinos cósmicos.

Los algoritmos de reconstrucción desarrollados dentro de la colaboración ANTARES utilizan el tiempo y la posición de los *hits*[3] para estimar la trayectoria del muón. Por lo tanto, calibrar de manera precisa los tiempos medidos por cada módulo óptico es fundamental si queremos obtener una buena reconstrucción. Con este objetivo, ANTARES está dotado de una serie de balizas ópticas que permiten sincronizar los tiempo marcados por los OMs con cierta periodicidad. El proceso requiere de la toma de "runes"[4] específicos en los que los módulos ópticos del detector son iluminadas mediante el sistema de balizas LED o utilizando el láser situado en la base de la línea 8. Por otra parte, los datos de muones atmosféricos descendentes detectados en ANTARES a un ritmo de 5-10 Hz se pueden utilizar para obtener, de manera independiente, los parámetros de la calibraciones temporal de los sensores del detector. Este segundo método no requiere de la paralización de la toma de datos para llevar a cabo la adquisición de runes de calibración como demanda el sistema de balizas ópticas.

La detección de neutrinos cósmicos y la identificación de sus fuentes de emisión son dos de los principales objetivos de un experimento como ANTARES. En el contexto de esta búsqueda los datos pueden describirse como un conjunto de eventos que, con una dirección y energía

[3] Un hit representa la información combinada del tiempo y la carga de la señal digitalizada por el PMT.

[4] Un run representa la unidad mínima de tiempo durante la cual se realiza una toma de datos de manera contínua.

determinada, se distribuyen sobre el cielo observable [5]. Mientras que los eventos atmosféricos (el fondo) aparecerán distribuidos uniformemente dentro de una cierta banda de declinación, los sucesos originados en una fuente astrofísica (la señal) se agruparán en torno a la posición de dicha fuente, con un cierto grado de dispersión debido a la resolución angular inherente al detector. Por otra parte, la distribución energética que esperamos para los neutrinos de origen cósmico es diferente de la que observamos en el caso de los sucesos originados en la interacción de los rayos cósmicos en la atmósfera. Las técnicas de agrupamiento o *clustering* de tipo *unbinned* permiten incorporar, mediante funciones de densidad de probabilidad, toda aquella información que mejora la capacidad de nuestro análisis para separar las contribuciones de la señal y del fondo en nuestra muestra de datos.

Calibración temporal

Con el fin de garantizar la mejor resolución angular en ANTARES se requiere una precisión en la calibración temporal relativa (la capacidad de sincronizar los tiempos medidos por cada OM) del orden del nanosegundo.

Dentro de la calibración temporal relativa podemos hablar de calibración dentro de la línea (*intra-line*) y calibración entre líneas (*inter-line*). La primera se ocupa de medir los desfases relativos entre los 75 OMs situados en una misma línea y corregirlos respecto al tiempo marcado por un único OM que se toma como referencia (uno de los tres OMs situados en el primer *storey*). La calibración *inter-line* se encargaría entonces de corregir los posibles desfases de todos los OMs instalados respecto a una única referencia común. Antes de su instalación en el emplazamiento marino, cada una de las líneas de ANTARES es calibrada en el laboratorio de integración utilizando un sistema compuesto por un láser y una red de fibra óptica a través de la cual se iluminan los OMs. Para cada OM se mide la diferencia entre el tiempo de emisión de la luz láser y el tiempo de llegada de los fotones al PMT. Después de corregir por el tiempo que tarda la luz en recorrer el camino de fibra óptica, se calculan las diferencias temporales respecto a un único OM que se elije como referencia. Los desfases entre OMs así determinados constituyen las primeras constantes de la calibración temporal.

[5] La posición de cada evento en este mapa del cielo se indica generalmente mediante las coordenadas equatoriales (δ, α) declinación y ascensión recta obtenidas mediante tranformaciones de los ángulos cenital y acimutal de la traza reconstruída.

Puesto que en el laboratorio no se realizó ninguna calibración posterior que nos permitiera determinar los posibles desfases existentes entre los los 12 OMs utilizados como referencia en cada línea, es necesario calibrar *in-situ* los tiempos medidos por cada línea. Para determinar estas correcciones hemos utilizado un método basado en los llamados residuos temporales de las trazas, i.e., las diferencias entre los tiempos de los hits que miden los OMs y los tiempo esperados que se calculan a partir de la trayectoria del muón reconstruida asumiendo un determinado conjunto de parámetros de la traza.

Utilizando un número de runes de física relativamente pequeño los desfases temporales entre las líneas del detector se determinan a partir del siguiente procedimiento iterativo:

1. Selección al azar de una línea sonda.
2. Reconstrucción de la traza utilizando los hits registrados por todas las líneas excepto la línea sonda.
3. Cálculo de los residuos temporales para los hits de la línea sonda respecto de la traza reconstruida.
4. Ajuste, a una función gaussiana, del pico de las distribuciones de los residuos temporales calculados en el paso anterior para cada línea. El valor medio de dicho ajuste se interpreta como el desfase de la línea analizada.
5. Correción de los tiempos de los hits que mide cada línea con los valores calculados en el paso previo.

En cada nueva iteración del método se repiten los cinco pasos anteriores, completándose el proceso cuando las correcciones obtenidas en la última iteracción son lo suficientemente pequeñas (< 0.5 ns). La exclusión de los hits de la línea sonda en la reconstrucción de la traza garantiza que los residuos temporales que obtenemos no estén sesgados, ya que la traza no ha sido ajustada minimizando aquellos.

Además del análisis de las trazas de muones descendentes, durante el periodo de investigación hemos realizado un estudio de la evolución, a lo largo de varios años de operación, de los parámetros TVC de la calibración. El TVC es un sistema de rampa de voltaje, incluído en el chip ARS, que permite realizar medidas temporales con precisiones superiores al nanosegundo.

Búsqueda de fuentes puntuales

La búsqueda de fuentes puntuales es uno de los principales análisis de física en ANTARES. El descubrimiento de una fuente de neutrinos tendría implicaciones directas sobre el origen de los rayos cósmicos y los mecanismos responsables de su aceleración. El primer paso del estudio consistió en seleccionar qué runes de física nos eran útiles de entre todos los que se tomaron los años 2007 a 2010. Con el objetivo de maximizar la cantidad de datos disponibles, se optó por incluir todos aquellos runes que cumplían con una serie de requisitos mínimos definidos por el grupo de análisis de calidad de los datos. De la lista de runes resultante excluimos también aquellos runes en los que las condiciones del detector no habían sido registradas y por tanto no podían ser correctamente simulados. También rechazamos una serie de runes que presentaban características anómalas en la actividad de algunos OMs. En total se seleccionaron 7419 runes de física que representan un tiempo de adquisición de 813 días.

A partir de esta primera muestra hicimos una nueva selección para determinar el conjunto de eventos donde buscar la existencia de una fuente de neutrinos. Para obtener dicha muestra se aplicaron diferentes cortes. En primer lugar, y con el objetivo de reducir la enorme contaminación de muones atmosféricos descendentes, solo se aceptaron aquellos eventos que eran reconstruidos siguiendo una trayectoria ascendente. En segundo lugar, y para disminuir la contribución de los muones descendientes que hubiesen sido erróneamente reconstruídos como ascendentes, se requirió que el valor del estimador del error angular en la dirección de la traza fuese menor que 1°. Por último, solo aquellos eventos con un valor del parámetro de calidad de la reconstrucción $\Lambda > -5.2$ fueron aceptados. Este último corte se decidió mediante la optimización del flujo necesario para descubrir una señal con una significancia de 5σ. Para evitar cualquier sesgo, el análisis de optimización de cortes se llevó a cabo sin conocer el valor real de la ascensión recta de los eventos, que se ocultó sustituyéndolo por un número generado de manera aleatoria a partir de una distribución uniforme. La muestra resultante de la aplicación de estos tres cortes contenía 3058 eventos candidatos a neutrinos de origen cósmico. Las simulaciones de Monte Carlo indican que 2408 ± 722 de estos sucesos consisten en neutrinos atmosféricos y sólo 358 ± 179 en muones atmosféricos.

Dichas simulaciones siguen el denominado esquema *run-by-run* bajo el que, mediante el muestreo del ritmo de cuentas que se registra en cada run, se garantiza que las condiciones

reales de ruido durante la adquisición se tengan en cuenta en las simulaciones de MC. Comparando dichas simulaciones con los datos reales para diferentes distribuciones de parámetros relacionados con las características de las trazas reconstruídas (ángulos cenital y acimutal, número de hits, incertidumbre angular, calidad de la reconstrucción, etc) se observa que, al nivel de los cortes que producen la selección final de eventos, el acuerdo entre los valores esperados y los observados está dentro de las incertidumbres teóricas en el cálculo de los flujos de neutrinos y muones atmosféricos, que fueron estimadas, respectivamente, en un 30% y un 50% a partir de las incertidumbres en parámetros de entrada del MC.

Utilizando estas mismas simulaciones se calculó que, al nivel de calidad de las trazas obtenido aplicando los cortes finales, la resolución angular (valor medio del error angular entre la traza generada y la reconstruída) estaba por debajo del medio grado, siendo de $0.42^\circ \pm 0.10^\circ$ para las configuraciones con más de 5 líneas de detección en funcionamiento. Por otra parte, la denominada aceptancia del detector, magnitud que nos indica el número de eventos que podríamos seleccionar y detectar en nuestro experimento para un cierto flujo de neutrinos, nos dice que observaremos casi 9 (5) eventos para una fuente a una declinación de -90° (0°) que produzca un flujo de $10^{-7}\mathrm{GeV}^{-1}\mathrm{cm}^{-2}\mathrm{s}^{-1}$.

Como hemos mencionado anteriormente, la búsqueda de un exceso de eventos significativo (sobre el fondo esperado) en nuestra muestra de datos se basó en el uso de métodos de clustering de tipo *unbinned*. Estas técnicas estadísticas nos permiten incorporar, por medio de funciones de distribución de probabilidad, toda aquella información que nos sirva para distinguir mejor entre ruido y señal. Asumimos, aquí, que nuestro problema se puede representar por un "modelo de mezcla" donde los datos observados consisten en dos componentes; la señal y el fondo. Para determinar cuál es la verdadera contribución de cada una de estas componentes utilizamos algoritmos basados en la maximización de la siguiente función de verosimilitud:

$$\mathcal{L} = \prod_{i=1}^{N} \left[\frac{n_s}{N} \mathcal{S}_i + (1 - \frac{n_s}{N}) \mathcal{B}_i \right], \qquad \text{(R.E3)}$$

donde $\mathcal{S}_i$ y $\mathcal{B}_i$ representan, respectivamente, las funciones de densidad de probabilidad (PDFs) de la señal y el fondo, *N* es el número total de eventos en nuestra muestra de datos y n_s es el número de eventos producidos por la fuente y cuyo valor desconocemos.

En nuestro análisis hemos estudiado dos algoritmos de maximización diferentes:

- En el algoritmo de Expectación-Maximización (E-M) la maximización de la función de verosimilitud se realiza analíticamente y siguiendo un proceso iterativo. En el esquema E-M, el conjunto de observaciones o eventos que componen nuestra muestra de datos se describe como un conjunto incompleto de vectores de los que desconocemos su peso, i.e., el parámetro que nos indica a qué colectivo (fondo o señal) pertenecen. El proceso de maximización consta de dos pasos; en una primera etapa se evalúa la función de verosimilitud utilizando un conjunto inicial de parámetros (incluyendo un valor inicial para los pesos). En un segundo paso, y mediante la maximización de la función de verosimilitud, se encuentra un nuevo conjunto de parámetros. El proceso se repite hasta que se alcanza la convergencia, obteniéndose un conjunto completo de vectores.

- En el segundo método utilizado (denominado NML) la maximización de la verosimilitud se realiza de manera numérica por medio de la rutina MIGRAD incluida en el paquete de software ROOT. La principal diferencia respecto a la implementación anterior es el uso de la información dada por el estimador de la incertidumbre en el error angular en la PDF que describe la distribución espacial de los eventos de señal. Mientras que en el E-M dicha PDF es una Gaussiana bidimensional cuya anchura es independiente de la resolución angular de nuestro telescopio, en el NML se introduce dicha dependencia asumiendo una anchura igual al valor del estimador en el error angular obtenido evento a evento.

El primer método es particularmente interesante cuando no conocemos la distribución espacial de la fuente, mientras que la segunda implementación permite mejorar la sensibilidad del análisis al reducir el número de parámetros libres de la búsqueda tal y como demuestra el lema de Neyman-Pearsons.

Para determinar si en nuestros datos existe una señal compatible con una fuente de neutrinos necesitamos un criterio que nos permita distinguir entre las dos hipótesis barajadas: A) Que en nuestros datos sólo hay eventos producidos por el fondo (o hipótesis nula). B) Que, además de los sucesos atmosféricos, nuestros datos contienen la contribución de una fuente de neutrinos cósmicos de una cierta intensidad (hipótesis alternativa). En este trabajo el criterio utilizado ha sido el test estadístico λ definido por el cociente de las funciones de verosimilitud que describen la hipótesis nula y su alternativa, donde la contribución de la

señal n_s se haya estimada como resultado de la maximización de la función de verosimilitud introducida anteriormente.

La significancia de la búsqueda se obtiene comparando el valor observado λ_{obs} con la distribución del test estadístico suponiendo que la hipótesis nula es la verdadera. Cuanto mayor es el valor observado de λ mayor es la significancia y los datos menos compatibles con la hipótesis de solo fondo. Puesto que no tenemos información a priori sobre como se distribuye λ, la interpretación estadística de nuestro observación se basa en la generación de pseudo-experimentos en los que reproducimos el resultado de un gran número de medidas mediante la generación de mapas falsos del cielo en los que distribuimos un número de eventos igual al presente en nuestra muestra de datos. A partir de pseudo-experimentos en los que inyectamos un cierto número de eventos de señal (generados a partir de las distribuciones obtenidas usando simulaciones de MC pesadas para un flujo de neutrinos cósmicos) en la muestra de datos, y siguiendo el principio de ordenación de Feldman y Cousins, construimos intervalos de confianza que nos permiten calcular límites al flujo de neutrinos cósmicos si no encontramos un exceso significativo en nuestros datos. La sensibilidad de la búsqueda, definida como el valor medio del límite superior que, con un nivel de confianza del 90$\%$, obtenemos a partir de experimentos de solo fondo es un factor $\sim$2.7 mejor que la sensibilidad alcanzada en el primer análisis de búsqueda de fuentes puntuales realizado en ANTARES.

Se llevaron a cabo dos diferentes tipos de búsquedas de fuentes puntuales. El primero de ellos consiste en buscar un infrecuente agrupamiento de eventos mirando en cualquier parte del cielo situado sobre el horizonte de ANTARES. El segundo enfoque se basa en el uso de una lista de fuentes de interés en cuyas direcciones se busca un exceso. La primera es una búsqueda global en la que no se introducen sesgos sobre la posición de la fuente. En la búsqueda con candidatos, al restringir el número de direcciones donde buscar una fuente, reducimos también la probabilidad de que el fondo genere una fluctuación estadística. La lista de fuentes candidatas utilizada en este análisis incluye 51 objetos, tanto galácticos como extra-galácticos, detectados por telescopios de rayos gamma en los últimos años. En ambas búsquedas, el valor del test estadístico resultante de cada pseudo-experimento se define como el valor más alto de entre todos los obtenidos en las posiciones del cielo examinadas. Se debe tener en cuenta que, con el objetivo de reducir el tiempo de cálculo, en la búsqueda en todo el cielo realizamos una pre-selección de localizaciones antes de evaluar nuestra función de

Tabla R.T1

Line	L1	L2	L3	L4	L5	L6
Offset	-1.26	-3.87	-0.50	-2.13	-3.42	-1.29
Line	L7	L8	L9	L10	L11	L12
Offset	0.63	4.91	0.27	-0.47	3.96	2.15

Desfases temporales entre las líneas del detector medidos con el método basado en los residuos temporal es de las trazas de muones atmosféricos. Los valores aquí recogidos han sido utilizados para las producciones oficiales (reconstrucción) de datos.

verosimilitud; solo son estudiados aquellos clusters que contengan al menos 4 eventos dentro de un cono de 3 grados de diámetro.

Resultados

Calibración con trazas de muones

Utilizando runes de física tomados con las doce líneas de instrumentación en funcionamiento se determinaron los primeros desfases temporales entre las diferentes líneas del detector. Las correcciones obtenidas se recogen en la tabla R.T1. La mayor desviación (de unos 5 nanosegundos) se da en la línea 8 que, como veremos, presenta ciertas particularidades.

Corregir los tiempos de los hits por los desfases temporales entre líneas medidos con trazas de muones revierte en un aumento del número de sucesos mejor reconstruidos de hasta un factor 2 y en una significativa mejora en el acuerdo entre datos y MC al comparar las distribuciones del parámetro de calidad de la reconstrucción.

Para estudiar el efecto de la calibración relativa entre líneas en la respuesta del detector hemos comparado la simulación estándar con eventos de MC en cuya reconstrucción hemos empeorado artificialmente los tiempos de los hits que registra cada línea, desfasándolos con los valores recogidos en la tabla **??**. Comprobamos que el efecto de no corregir los desfases temporales entre líneas implica un empeoramiento de hasta el 40% en la resolución angular del telescopio.

La baliza láser instalada a los pies de la línea 8 del detector nos ofrece la posibilidad de cotejar los resultados obtenidos a partir de los residuos temporales de las trazas de muones atmosféricos con un método completamente independiente. Dicho método se basa en el análisis de los datos obtenidos en la toma (realizada una vez al mes) de runes de calibración

específicos en lo que, durante una media de 10 minutos, el láser ilumina las líneas del detector. Aquí, el residuo temporal se define como la diferencia entre el tiempo de emisión de la luz y el tiempo en el que el flash de fotones es detectado por el OM, corregida por el tiempo que emplea la luz en viajar desde la fuente a dicho OM. Distribuciones de los residuos temporales se obtienen para todos los OMs de cada una de las líneas. Mediante el ajuste de estas distribuciones a una función gaussiana convolucionada con una exponencial se obtiene la posición del máximo. Para cada línea, los valores del pico del ajuste se representan en función de la distancia entre el OM y la baliza láser. La distribución resultante se ajusta a una recta, cuyo coeficiente se interpreta como el offset de la línea analizada. Los valores obtenidos con el método de baliza láser coinciden dentro del nanosegundo con los obtenidos mediante el análisis con trazas de muones excepto para la línea 1 y la línea 8. Para esta última línea la discrepancia es mayor de 2 ns. Hay que tener en cuenta que, al estar situado en su base, la luz emitida por el láser no alcanza de manera directa a los OMs de esta línea. La discrepancia observada deberá ser clarificada mediante el análisis de los datos obtenidos con el láser recientemente instalado a los pies de una línea de instrumentación que se sitúa fuera del esquema octogonal que siguen las líneas de detección.

Aunque solo se esperan cambios en caso de que el PMTs del OM de referencia de una línea particular sea sustituido o su valor de alto voltaje se vea modificado, siempre es necesario monitorizar los parámetros de la calibración. En este sentido, hemos realizado un estudio de la estabilidad de los desfases temporales entre líneas medidos con trazas de muones que abarca los años 2008 a 2012. Los resultados muestran que la distribución de los valores obtenidos en cada periodo investigado es inferior a 1ns, lo que nos proporciona una estimación de la precisión del método.

En cuanto a la calibración temporal *intra-line*, se llevó a cabo un primer test para evaluar las posibilidades del método basado en las trazas de muones de determinar los parámetros T0 de la calibración. En dicho test se empleó un conjunto de runes de física tomados durante el mes de octubre del año 2010. El algoritmo de iteración del método se modificó para reducir el tiempo de procesamiento y el número de runes necesarios para conseguir distribuciones de los residuos temporales con una buena estadística. Puesto que las constantes T0 obtenidas con el sistema de balizas LED se utilizan automáticamente en la reconstrucción[6], los valores de los

[6]El algoritmo de la reconstrucción lee dicha información de las tablas de calibración en la base de datos.

desfases temporales medidos por el método de las trazas han de entenderse como correcciones al sistema LED. Para el 90% de los ARSs las correcciones son inferiores a 1ns, un resultado que valida la calibración intra-line realizada con el sistema de balizas LED.

Búsqueda de fuentes de neutrinos cósmicos

Dos búsquedas con distinto enfoque se han llevado a cabo sobre los 3058 eventos seleccionados en nuestra muestra de datos.

La mayor desviación estadística sobre el fondo se encontró en la búsqueda sobre todo el cielo visible, que abarca el rango de declinaciones $\delta[-90°, 48°]$. El cluster con un mayor valor del test estadístico se localizó en las coordenadas $(\alpha, \delta) = (-46.5°, -65.0°)$. Su significancia estadística equivale a 2.2σ en términos de número de desviaciones estándar (convención *2-sided*). Los dos métodos de agrupación producen este mismo resultado cuando, en la implementación NML, los valores del estimador de la incertidumbre en el error angular se reescalan mediante un factor que tenga en cuenta la anchura de la distribución tipo $pull$ que se obtiene para el ángulo cenital pesado por el estimador del error angular.

En cuanto a la búsqueda utilizando una lista de fuentes candidatas, la mayor desviación estadística se obtiene para la fuente conocida como 3C279 con coordenadas $(\alpha, \delta) = (-5.79°, -165.95°)$. Dicho resultado es compatible con el fondo cuando se aplica cualquiera de los algoritmos de búsqueda. Puesto que no se ha descubierto ninguna fuente de neutrinos en los datos, hemos calculado los límites al flujo (al 90% de nivel de confianza) para las 51 fuentes candidatas. Cabe resaltar que entre los resultados obtenidos se encuentran algunos de los límites más restrictivos obtenidos hasta la fecha para fuentes situadas en el hemisferio sur.

Además, para las fuentes candidatas Vela X y RXJ1713.7-3946 se han recalculado los límites teniendo en cuenta la morfología de dichas fuentes (determinada por las observaciones del telescopio H.E.S.S.) así como un modelo de flujo más preciso que tiene en cuenta dichas observaciones y parametrizaciones actuales de la producción de piones y su desintegración en interacciones hadrónicas. Los valores MRF (factor de rechazo del modelo) para estas dos fuentes nos permiten constreñir flujos un factor $\sim$10 más altos que los predichos.

Por último, utilizando una lista de lentes gravitacionales que pudieran aumentar el flujo de neutrinos procedentes de una posible fuente situada en el foco de dichas lentes, se realizó una nueva búsqueda con 11 candidatos. En este caso, la mejor fuente resultó ser el SDSS

1004+4112, con una valor-p del 49% (99%) tras corregir el resultado por el hecho de haber realizado 11 (62) búsquedas.

Conclusiones

ANTARES es el primer telescopio de neutrinos en utilizar el agua de mar como medio de detección. Desde la instalación de la primera línea de instrumentación a comienzos del año 2006, nuestro detector ha tomado (y sigue tomando) datos de manera continua. En su configuración final, alcanzada tras la instalación de la decimosegunda línea de detección en mayo de 2008, ANTARES registra una media de 3 neutrinos ascendentes al día. La experiencia adquirida con el desarrollo de este instrumento es la mayor garantía de viabilidad para llevar a cabo la construcción de un telecopio de neutrinos con un volumen superior al km^3 en el fondo del Mar Mediterráneo. Un detector de estas características permitirá explorar el hemisferio sur celeste con una sensibilidad muy superior a la actual y desde una posición privilegiada para el estudio del centro galáctico. Un instrumento como el proyectado por el consorcio KM3NeT permitirá, además, confirmar lo que parecen ser las primeras señales de neutrinos cósmicos observadas recientemente por el telecopio de neutrinos IceCube.

El trabajo de investigación que se resume en la presente tesis doctoral abarca dos aspectos fundamentales de los telescopios de neutrinos. El primero consiste en la calibración temporal del detector, imprescindible para garantizar el funcionamiento óptimo del telescopio. El segundo corresponde a la búqueda de fuentes de neutrinos cósmicos, uno de los objetivos principales en el diseño de un experimento como ANTARES. Los principales resultados obtenidos en estos dos temas se resumen a continuación:

Calibración temporal con trazas de muones

- Se llevó a cabo la implementación de un método que, basado en el análisis de los residuos temporales de las trazas de muones atmosféricos, permite obtener los parámetros de la calibración temporal del detector de manera independiente al sistema de balizas diseñado a tal efecto y sin necesidad de detener la adquisición de datos de física.

- Los desfases temporales entre las líneas del detector determinados con este nuevo

método forman parte, en la actualidad, de los parámetros de calibración oficiales utilizados en el procesamiento de los datos reales.

- Sincronizar los tiempos medidos por las 12 líneas que componen el detector se traduce en un incremento de hasta un factor dos en el número de trazas mejor reconstruidas. El acuerdo entre los datos y las simulaciones MC mejora de manera significativa.

- Los parámetros de la calibración *inter-line* obtenidos aplicando el método de las trazas de muones son compatibles (al nivel del nanosegundo) con los valores determinados, de manera independiente, a partir del análisis con la baliza laser. Los resultados proporcionados por el nuevo método consiguen validar la calibración de los parámetros T0 obtenida a través del sistema de balizas LED.

Búsqueda de fuentes de neutrinos cósmicos

- Se analizaron los datos registrados por el detector durante casi 4 años de operación. Los runes de física utilizados representan 813 días de toma de datos. La muestra de datos final contiene 3058 eventos seleccionados en un análisis basado en la optimización del flujo de neutrinos necesario para producir un descubrimiento.

- Para determinar la presencia de una fuente de neutrinos en la muestra de datos se emplearon técnicas *unbinned* y algoritmos de maximización de la función de verosimilitud. Por primera vez, la información de la energía y del error angular estimado evento a evento se utilizaron en una búsqueda de fuentes puntuales con datos de ANTARES. Incluir esta información se tradujo en un incremento de la sensibilidad del análisis cercano al 30$\%$.

- El grupo de eventos más interesantes se encontró en una búsqueda realizada en todo el cielo visible sobre el horizonte del detector. Dicha agrupación, una significancia estadística de 2.2σ, está formada por 5 eventos que se sitúan a menos de un grado de las coordenadas $(\alpha, \delta) = (-46.5^\circ, -65.0^\circ)$. Este resultado es compatible con una fluctuación estadística del fondo.

- La fuente candidata con un valor más alto del test estadístico es 3C 279. Se trata de un blazar con coordenadas $(\alpha, \delta) = (-5.79^\circ, -165.95^\circ)$. El valor-p corregido es, de nuevo,

compatible con el fondo. No habiéndose encontrado ningún exceso estadísticamente significativo, se calcularon límites superiores al flujo para las 51 fuentes en nuestra lista de candidatos. Algunos de los límites calculados son los más restrictivos obtenidos hasta la fecha para fuentes en el hemisferio sur celeste.

- Utilizando los datos obtenidos por el telescopio de rayos gamma H.E.S.S. y asumiendo modelos astrofísicos específicos se recalcularon los límites para dos de las fuentes en la lista de candidatos. Los resultados obtenidos permiten excluir un flujo un factor 7.6 y un factor 9.8 superior a la predicción teórica para las fuentes Vela X y RXJ1713.7-3946 respectivamente.

- La búsqueda de correlación con lentes gravitacionales tampoco reveló ningúna fuente de neutrinos. La candidata con un valor más alto del test estadístico ($\lambda = 0.35$) es SDSS 1004+4112. Este valor, o uno superior, tiene lugar en aproximadamente la mitad de todos los pseudo-experimentos con solo fondo.

References

[1] V. F. Hess. Uber beobachtungen der durchdringenden strahlung bei sieben freiballonfahrten. *Phys. Zeit. 13, p. 1084*, 1912.

[2] P. Auger et al. Extensive cosmic-rays showers. *Reviews of Modern Physics, 288-291*, 1939.

[3] J.R. Horandel. Models of the knee in the energy spectrum of cosmic rays.

[4] T. Antoni et al. (KASKADE Coll.). Kaskade measurements of energy spectra for elemental groups of cosmic rays: Results and open problems. *Astropart. Phys. 24, 1*, 2005.

[5] T. Wibig and A. W. Wolfendale. At what particle energy do extragalactic cosmic rays start to predominate? *J. Phys. G: Nucl. Part. Phys. 31 255*, 2005.

[6] P. Abreu et al. (Pierre Auger Coll.). The pierre auger observatory i: The cosmic ray energy spectrum and related measurements. *Proceedings of the 32nd International Cosmic Ray Conference*, 2011.

[7] R. U. Abassi et al. First observation of the greisen-zatsepin-kuzmin suppression. *Phys. Rev. Lett. 100, 101101*, 2008.

[8] K. Greissen. End to the cosmic-ray spectrum? *Phys. Rev. Lett. 16, 748*, 1966.

[9] G. T. Zatsepin and V. A. Kuzmin. Upper limit of the spectrum of cosmic rays. *JETP Lett. 4, 78*, 1966.

[10] J. Beringer et al. Review of particle physics (particle data group). *Phys. Rev. D86 010001*, 2012.

[11] T. Chiarusi and M. Spurio. High-energy astrophysics with neutrino telescopes. *arXiv:0906.2634v1*, 2009.

[12] P. Abreu et al. The pierre auger observatory i: The cosmic ray energy spectrum and related measurements. *Contributions to the 32nd ICRC, axXiv:1107.4809*, 2011.

[13] D. Semikoz. Constrains on top-down models for the origin of uhecrs from the pierre observatory data. *Proceeding of the 30th International Cormic Ray Conference*, 2007.

[14] E. Fermi. On the origin of the cosmic radiation. *Phys. Rev. 75(8), 1169-1174*, 1949.

[15] T. Haugbolle J.T. Frederiksen, C.B. Hededal and A. Nordlund. Magnetic field generation in collisionless shocks: Pattern growth and transport,. *The Astrophysical Journal Letters 608(1), L13*, 2004.

[16] M. Kachelriess. Lecture notes on high energy cosmic rays. *arXiv:0801.4376v1*, 2008.

[17] A. M. Hillas. The origin of ultra-high energy cosmic rays. *Ann. Rev. Astron. Astrophys. 25, 425-444*, 1995.

[18] P Sommers and S Westerhoff. Cosmic ray astronomy. *New Journal of Physics 11 055004*, 2009.

[19] The pierre auger observatory. *http://www.auger.org*.

[20] PAO Collaboration. Correlation of the highest-energy cosmic rays with nearby extragalactic objects. *Science, Vol. 318 no. 5852 pp. 938-943*, 2007.

[21] P. Abreu et al. Update on the correlation of the highest energy cosmic rays with nearby extragalactic matter. *Astroparticle Physics 34, 314-326*, 2010.

[22] The Fermi-LAT Collaboration. Fermi large area telescope second source catalog. *ApJS 199 31*, 2012.

[23] M. Su et al. Giant gamma-ray bubbles from fermi-lat: Agn activity or bipolar galactic wind? *Astrophys. J. 74, 1044-1082*, 2010.

[24] T.C. Weekes et al. Veritas: the very energetic radiation imaging telescope array system. *Astrop. Phys., 17:221243*, 2002.

[25] J. Albert et al. Physics and astrophysics with a ground-based gamma-ray telescope of low energy threshold. *Astrop. Phys., 23:493509*, 2005.

[26] J.A. Hinton. The status of the hess project. *New Astron. Rev., 48:331337*, 2004.

[27] F. Aharonian et al. The h.e.s.s. survey of the inner galaxy in very high-energy gamma-rays. *Astrophys. Journal 636, 777-797*, 2008.

[28] The cherenkov telescope array. *http://www.cta-observatory.org*.

[29] The tevcat. *http://tevcat.uchicago.edu*.

[30] F.B. Harrison H. W. Kruse C.L. Cowan, F. Reines and A.D. McGuire. Detection of the free neutrino: A confirmation. *Science 124, 103*, 1956.

[31] K. Hirata et al. Observation of a neutrino burst from the supernova sn1987a. *Phys. Rev. Lett., 58:1490*, 1987.

[32] R.M.Bionta et al. Observation of a neutrino burst in coincidence with supernova 1987a in the large magellanic cloud. *Phys. Rev. Lett., 58:1494*, 1987.

[33] V.I. Volchenko E.N. Alekseev, L.N. Alekseeva and I.V. Krivosheina. Detection of the neutrino signal from sn 1987a in the lmc using the inr baksan underground scintillation telescope. *Physics Letters, B 205:209*, 1988.

[34] D.S. Hamer R. Davis and K.C. Hoffman. Search for neutrinos from the sun. *Phys. Rev. Lett. 20, 1205*, 1968.

[35] A. Serenelli J. N. Bahcall and S. Basu. 10,000 standard solar models: a monte carlo simulation. *Ap. J, 621 L85*, 2005.

[36] B. Pontecorvo. Mesonium and antimesonium. *Sov. Phys., JETP, 6, 429.*, 1957.

[37] T. Kobayashi et al. Proceedings of 25th international conference on neutrino physics and astrophysics (neutrino 2012). *Nucl.Phys.Proc.Suppl. 235-236 pp.1-510*, 2012.

[38] J. G. Learned and S. Pakvasa. Detecting ν_{tau} oscillations at pev energies. *Astropart. Phys. 3(3), 267-274*, 1995.

[39] T.C. Weekes. et al. Observation of tev gamma rays from the crab nebula using the atmospheric cerenkov imaging technique. *Astrophys. J. 342, 379-395*, 1989.

[40] V. L. Ginzburg and V. S. Ptuskin. On the origin of cosmic rays: Some problems in high-energy astrophysics. *Rev. Mod. Phys. 48, 161*, 1976.

[41] A. M. Hillas. Can diffusive shock acceleration in supernova remnants account for high-energy galactic cosmic rays? *J. Phys. G: Nucl. Part. Phys. 31 R95*, 2005.

[42] Aharonian et al (H.E.S.S. collaboration). First detection of a vhe gamma-ray spectral maximum from a cosmic source: Hess discovery of the velax nebula. *Astron. Astrophys., 448, L43*, 2006.

[43] H. Muraishi et al. Evidence for tev gamma-ray emission from the shell-type snr rx j1713.7-3946. *Astron. Astrophys. 354, L57*, 2000.

[44] R. Enomoto et al. The acceleration of cosmic-ray protons in the supernova remmant snr rx j1713.7-3946. *Nature 416, 823*, 2002.

[45] F.Aharonian et al. A detailed spectral and morphological study of the gamma-ray supernova remnant rx j1713.7-3946 with h.e.s.s. *Astron.Astrophys. 449 223-242*, 2006.

[46] C. Stegmann F.A. Aharonian. A. Kappes, J. Hinton. Potential neutrino signals from galactic gamma-ray sources. *ApJ 656, 870.*, 2007.

[47] Fermi LAT Collaboration A.A. Abdo et al. Observations of the young supernova remnant rx j1713.7-3946 with the fermi large area telescope. *ApJ, 734, 28*, 2011.

[48] F. Aharonian et al. A detailed spectral and morphological study of the gamma-ray supernova remnant rx j1713.7-3946 with hess. *Astronomy and Astrophysics, Volume 449, Issue 1, pp.223-242*, 2006.

[49] Hoshino et al. Relativistic magnetosonic shock waves in synchrotron sources - shock structure and nonthermal acceleration of positrons. *Astrophys.J. 390 (1992) 454-479*, 1992.

[50] W. Bednarek. Neutrinos from the pulsar wind nebulae. *Astron.Astrophys. 407 1-6*, 2003.

[51] Abramowski et al. Probing the extent of the non-thermal emission from the vela x region at tev energies with h.e.s.s. *arXiv:1210.1359v1*, 2012.

[52] S. Chaty. Microquasars and jets. *proceedings of Rencontres de Moriond, Very High Energy Phenomena in the Universe, astro-ph/0506008*, 2005.

[53] R. Fender S. Migliari and M. M. Méndez. Iron emission lines from extended x-ray jets in ss 433: Reheating of atomic nuclei. *Science, Vol. 297, no. 5587 pp. 1673-1676*, 2002.

[54] F. Aharonian et al. Discovery of very high energy gamma rays associated with an x-ray binary. *Science, 309, 746.*, 2005.

[55] J. Albert et al. Variable very high energy gamma-ray emission from the microquasar ls i+61 303. *Science, 312, 1771. astro-ph/0605549*, 2006.

[56] Fermi coll. Modulated high-energy gamma-ray emission from the microquasar cygnus x-3. *Science, Vol. 326 no. 5959 pp. 1512-1516*, 2009.

[57] M. Punch et al. Detection of tev photons from the active galaxy markarian 421. *Nature vol. 358, no. 6386 p. 477, 478*, 1992.

[58] L. Ferrarese and D. Merritt. A fundamental relation between supermassive black holes and their host galaxies. *Astrophys.J. 539 L9*, 2000.

[59] K. Gebhardt et al. A relationship between nuclear black hole mass and galaxy velocity dispersion.

[60] A. Mückea1 and R.J. Protheroe. Neutrino emission from hbls and lbls. *Proc. 27th Int. Cosmic Ray Conf.*, 2001.

[61] T. Piran. Gamma-ray bursts and the fireball model. *Phys. Rep. 314, pp. 575-667*, 1999.

[62] E. Waxman and J. Bahcall. High energy neutrinos from cosmological gamma-ray burst fireballs. *Physical Review Letters 78, pp. 2292-2295*, 1997.

[63] J. Alvarez-Muñiz D. Guetta, D. Hooper and E. Reuveni. Neutrinos from individual gamma-ray bursts in the batse catalog. *Astroparticle Physics, 20, 429-455*, 2004.

[64] *http://www.batse.msfc.nasa.gov/batse/grb/skymap*.

[65] F. Acero et al. (H.E.S.S. Coll.). Detection of gamma rays from a starburst galaxy. *Science, 326, 1080*, 2009.

[66] N. Karlsson for the VERITAS Coll. Discovery of vhe gamma-ray emission from the starburst galaxy m82. *presented at FERMI symposium, Washington D.C., USA. arXiv:0912.3807[astro-ph.HE].*, 2009.

[67] E. Andrs et al. The amanda neutrino telescope: Principle of operation and first results. *Astropart. Phys. 13, 1*, 2000.

[68] F. Halzen. Lectures on high-energy neutrino astronomy. *arXiv:astro-ph/0506248v1*, 2005.

[69] The IceCube Collaboration. Preliminary design document. *http://icecube.wisc.edu/reports*, 2001.

[70] F. Halzen and S.R. Klein. Icecube: An instrument for neutrino astronomy. *Rev. Sci. Instrum. 81 081101621*, 2010.

[71] The KM3Net Consortium. *http://www.km3net.org*.

[72] The KM3Net Consortium. *http://www.km3net.org/CDR/CDR-KM3NeT.pdf*.

[73] The KM3Net Consortium. *http://www.km3net.org/TDR/TDRKM3NeT.pdf*.

[74] V. Aynutdinov et al. The prototype string for the km3-scale baikal neutrino telescope. *Nucl. Inst. Meth. A602 227*.

[75] R. Gandhi et al. Ultrahigh-energy neutrino interactions. *Astrop. Phys., 5:81-110*, 1996.

[76] S. Adrián-Martínez et al. Measurement of the group velocity of light in sea water at the antares site. *Astropart. Phys., 35, pp.552-557*, 2012.

[77] Zheleznykh I. M. Markov, M. A. Proceedings of the 10th int. conf. on high-energy physics. *Rochester Conference, 579*, 1960.

[78] G. Carminati et al. Atmospheric muons from parametric formulas: A fast generator for neutrino telescopes. *Comp. Phys. Comm. 179:915-923*, 2008.

[79] P. Lipari S. Robbins G.D. Barr, T.K. Gaisser and T. Stanev. Three-dimensional calculation of atmospheric neutrinos. *Physical Review D 79, 023006*, 2004.

[80] M. Ageron et al. Antares: the first undersea neutrino telescope. *Nuclear Inst. and Methods in Physics Research, A 656 (2011) pp. 11-38*, 2011.

[81] P.Amram et al. The antares optical module. *Nucl. Instrum. Meth. A484 369-383*, 2002.

[82] J. A. Aguilar et al. Study of large hemispherical photomultiplier tubes for the antares neutrino telescope. *Nucl. Inst. and Meth. A, 555, 132-141*, 2005.

[83] S. Adrián-Martínez et al. The positioning system of the antares neutrino telescope. *JINST 7, T08002*, 2012.

[84] J. A. Aguilar et al. The antares optical beacon system. *Nucl. Inst. and Meth. Phys. Res. A, 570, 107-116*, 2007.

[85] J.A. Aguilar et al. The data acquisition system for the antares neutrino telescope. *Nucl. Instr. and Meth. A 570 107-116*, 2007.

[86] J.A. Aguilar et al. Performance of the front-end electronics of the antares neutrino telescope. *Nucl. Instr. and Meth. A 622, 59-73*, 2010.

[87] R. Brun and F. Rademakers. Root: An object oriented data analysis framework. *Nucl. Instr. and Meth. Phys. Res. A, 389, http://root.cern.ch*, 1997.

[88] J. A. Aguilar et al. Time calibration of the antares neutrino telescope. *Astr. Part. Phys. 34, 539-549*, 2011.

[89] J. A. Aguilar et al. Charge calibration of the antares high energy neutrino. *Proceedings of the 31st International Cosmic Ray Conference*, 2009.

[90] H. Yepes-Ramirez. Water absorption length measurement with the antares optical beacon system. *Nucl. Instr. and Meth. Phys. Res. A, 626-627, S118*, 2011.

[91] J.A. Aguilar et al. Transmission of light in deep sea water at the site of the antares neutrino telescope. *Astrop. Phys., 23:131155*, 2005.

[92] P. Amram et al. Sedimentation and fouling of optical surfaces at the antares site. *Astropart. Phys., 19:253-267*, 2003.

[93] M. Ageron et al. Studies of a full scale mechanical prototype line for the antares neutrino telescope and tests of a prototype instrument for deep-sea acoustic measurements. *Nucl. Instr. and Meth. Phys. Res. A, 581:695708,*, 2007.

[94] J. A. Aguilar et al. First results of the instrumentation line for the deep-sea antares neutrino telescope. *Astropart. Phys., 26:314324*, 2006.

[95] P. Coyle. Results from the antares deep sea neutrino telescope. *International Conference on Neutrino Physics and Astrophysics (Neutrino 2012)*, 2012.

[96] D. Heck et al. Forschungszentrum karlsruhe report. *FZKA-6019*, 1998.

[97] C. Forti et al. Simulation of atmospheric cascades and deep-underground muons. *Phys. Rev. D42, 3668-3689*, 1990.

[98] P. Antonioli et al. A three-dimensional code for muon propagation through the rock: Music. *Astropart. Phys. 7, 357-368*, 1997.

[99] D. Bailey. Monte carlo tools. *PhD thesis, University of Oxford.*, 2002.

[100] V. Agrawal et al. Atmospheric neutrino flux above 1 gev. *Phys. Rev D 53, 1314-1323*, 1996.

[101] A. Ferrari T. Montaruli G. Battistoni and P. Sala. The fluka atmospheric neutrino flux calculation. *hep-ph/0207035*, 2002.

[102] J.A. Aguilar et al. Zenith distribution and flux of atmospheric muons measured with the 5-line antares detector. *Astropart. Phys. 34, 179-184*, 2010.

[103] J. Brunner. Geasim: User manual. *ANTARES Internal Note*.

[104] S. Navas and L. Thompson. Km-a7 user guide and reference manual. *ANTARES Internal Note (SOFT/011)*, 1999.

[105] GEANT program manual. Cern program library long writeup. *W5013*, 1993.

[106] M. de Jong. The triggerefficiency program. *Antares Internal Note.*, 2009.

[107] J.A. Aguilar et al. A fast algorithm for muon track reconstruction and its application to the antares neutrino telescope. *Astropart. Phys., 34, 652-662*, 2011.

[108] A. Heijboer. Track reconstruction and point source searches with antares. *phD thesis, Universiteit van Amsterdam.*, 2004.

[109] S. Karkar. Detection de microquasars et calibration en temps du telescope a neutrinos antares. *PhD thesis, Universiti de la Miditirranie Aix-Marseille II*, 2004.

[110] F. Salesa. Time calibration and point source analysis with the antares neutrino telescope. *phD thesis, Universitat de Valéncia*, 2010.

[111] J. S. Kaputinsky et al. A fast timing light pulser for scintillation detectors. *Nucl. Instr. and Meth. Phys. Res., A, 241:612-613.*, 1985.

[112] J. Hartman C. Bogazzi and A. Heijboer. Point source search with 2007 and 2008 data. *ANTARES Internal Note (PHYS/008)*, 2010.

[113] T. Eberl and C. Kopper. The seatray software framework. *ANTARES Internal Note (SOFT/013)*, 2009.

[114] The IceCube Neutrino Observatory homepage: http://icecube.wisc.edu.

[115] S. Robbins G.D. Barr, T.K. Gaisser and T. Stanev. Uncertainties in the atmospheric neutrino fluxes. *Phys. Rev. D74 094009*, 2006.

[116] T.K. Gaisser G.D. Barr, S. Robins and T. Stanev. Uncertainties in atmospheric neutrino fluxes. 1975.

[117] N. M. Laird A. P. Dempster and D. B. Rubin. Maximum likelihood from incomplete data via the em algorithm. *J. Royal Statistical Soc. Series. B39 1-38.*, 1977.

[118] J. A. Aguilar and J. J. Hernández-Rey. The expectation-maximization algorithm applied to the search of point sources of astroparticles. *Astropart. Phys. 29, 117.*, 2008.

[119] F. James. Minuit - a system for function minimization and analysis of the parameter errors and correlations. *Computer Physics Communications 10, 343-367*, 1975.

[120] J. Neyman and E. S. Pearson. On the problem of the most efficient test of statistical hypotheses. *Royal Society of London Philosophical Transactions, Series A 231, 289-337.*, 1933.

[121] M. Kendall and A. Stuart. The advanced theory of statistics volume 2. *Charles Griffin Co. Ltd.*, 1978.

[122] J. Neyman. Outline of a theory of statistical estimation based on the clasical theory of probability. *Phil. Trans. Royal. Soc. London, Series A 236, 333-380*, 1937.

[123] G.J. Feldman and R.D. Cousins. A unified approach to the classical statistical analysis of small signals. *Phys. Rev. D 57, 3873-3889*, 1998.

[124] Garabed Halladjian. Update on the absolute pointing with the acoustic positioning system. *ANTARES Internal documentation*.

[125] A. A. Abdo et al. Milagro observations of tev emissions from galactic sources in the fermi bright source list. *Astrophys. J. 700, 127-131*, 2009.

[126] S. Toscano. Golden-list for a point source search in antares. *ANTARES Internal Note (PHYS/002)*, 2009.

[127] S. Adrián-Martínez et al. First search for point sources of high energy cosmic neutrinos with the antares neutrino telescope. *ApJ, Volume 743, L14*, 2011.

[128] R. Abassi et al. Time-integrated searches for point-like sources of neutrinos with the 40-string icecube detector. *ApJ, Volume 732, 18.*, 2011.

[129] Ambrosio et al. Neutrino astronomy with the macro detector. *ApJ, Volume 546, 1038.*, 2001.

[130] E. Thrane et al. Search for astrophysical neutrino point sources at super-kamiokande. *ApJ, Volume 704, 503.*, 2009.

[131] R. Abbasi et al. Search for point sources of high energy neutrinos with final data from amanda-ii. *Phys. Rev. D, 79, 062001.*, 2009.

[132] A. Kappes for the IceCube Collaboration. Neutrino astronomy with the icecube observatory. *J. Phys.: Conf. Ser. 409 012014*, 2013.

[133] C. Quigg O. Mena, I. Mocioiu. Gravitational lensing of supernova neutrinos. *arXiv:astro-ph/0610918v1*.

[134] S. Mangano. Gravitational lensing and neutrinos. *ANTARES Internal Note (PHYS/008)*, 2012.

[135] IceCube Collaboration M. Aartsen et al. First observation of pev-energy neutrinos with icecube. *Phys. Rev. Lett. 111, 021103*, 2013.